9 Cosmic Microwave Background Anisotropy

9.1 Introduction

The cosmic microwave background (CMB) is isotropic to a high degree. This tells us that the early universe was rather homogeneous at the time ($t = t_{\mathrm{dec}} \approx 370\,000$ years) the CMB was formed. However, with precise measurements we can detect a low-level anisotropy in the CMB (Fig. 1) which reflects the small perturbations in the early universe.

This anisotropy was first detected by the COBE (Cosmic Background Explorer) satellite in 1992, which mapped the whole sky in three microwave frequencies. The angular resolution of COBE was rather poor, 7°, meaning that only features larger than this were detected. Measurements with better resolution, but covering only small parts of the sky were then performed using instruments carried by balloons to the upper atmosphere, and ground-based detectors located at high altitudes. A significant improvement came with the WMAP (Wilkinson Microwave Anisotropy Probe) satellite, which made observations for nine years, from 2001 to 2010.

The best CMB anisotropy data to date, covering the whole sky, has been provided by the Planck satellite (Fig. 2). Planck was launched by the European Space Agency (ESA), on May 14th, 2009, to an orbit around the L2 point of the Sun-Earth system, 1.5 million kilometers from the Earth in the anti-Sun direction. Planck made observations for over four years, from August 12th, 2009 until October 23rd, 2013. The first major release of Planck results was in 2013 [1] and the second release in 2015 [2]. Final Planck results were released in 2018 and 2019.

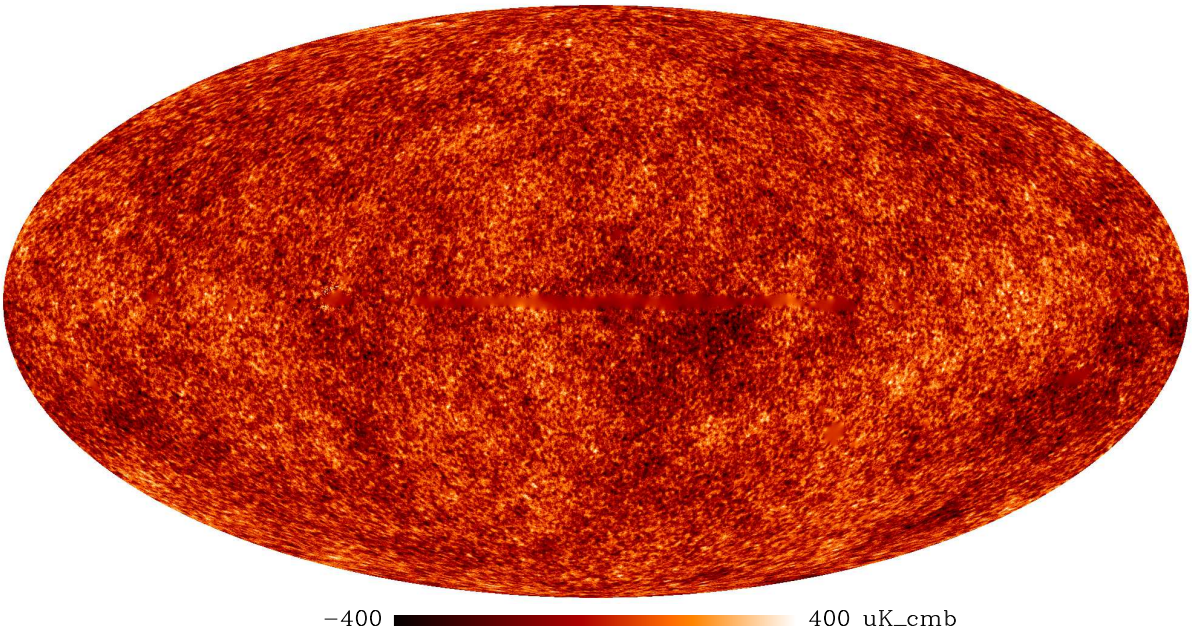

Figure 1: Cosmic microwave background. The figure shows temperature variations from $-400\,\mu$K to $+400\,\mu$K around the mean temperature (2.7255 K) over the whole sky, in galactic coordinates. The color is chosen to mimic the true color of CMB at the time it was formed, when it was visible orange-red light, but the brightness variation (the anisotropy) is hugely exaggerated by the choice of color scale. The fuzzy regions, notable especially in the galactic plane, are regions of the sky where microwave radiation from our own galaxy or nearby galaxies makes it difficult to separate out the CMB. (ESA/Planck data).

Planck observed the entire sky twice in a year. The satellite repeated these observations year after year, and the results become gradually more accurate, since the effects of instrument noise averaged out and various instrument-related systematic effects could be determined and corrected better with repeated observations.

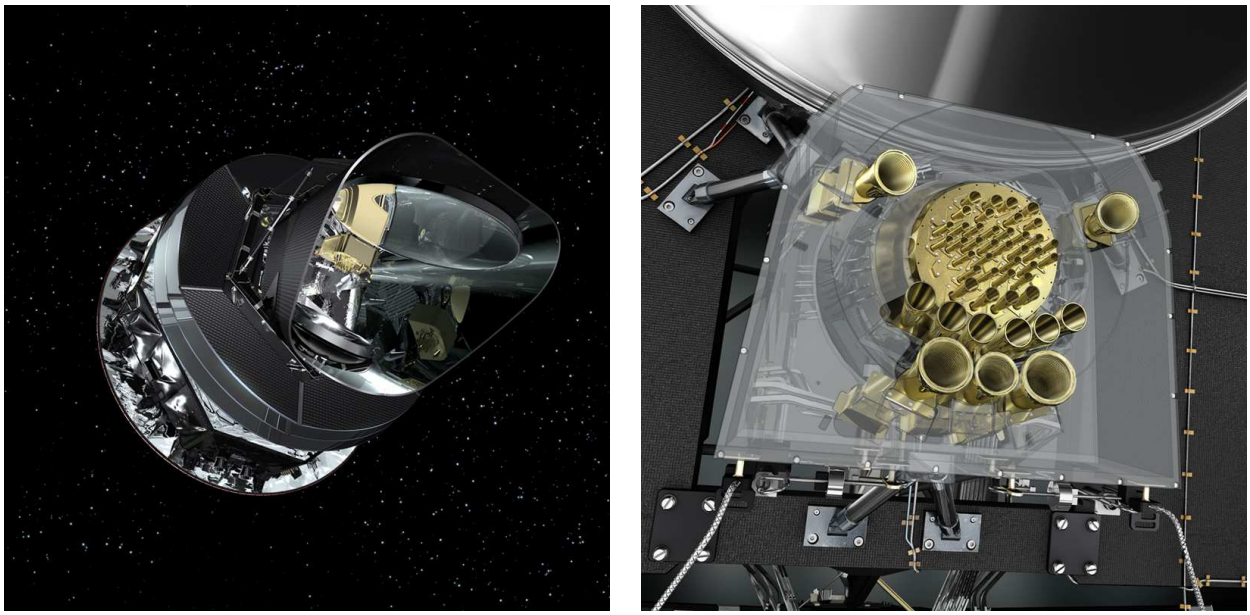

Figure 2: The Planck satellite and its microwave receivers. The larger horns are for receiving lower frequencies and the smaller horns for higher frequencies.

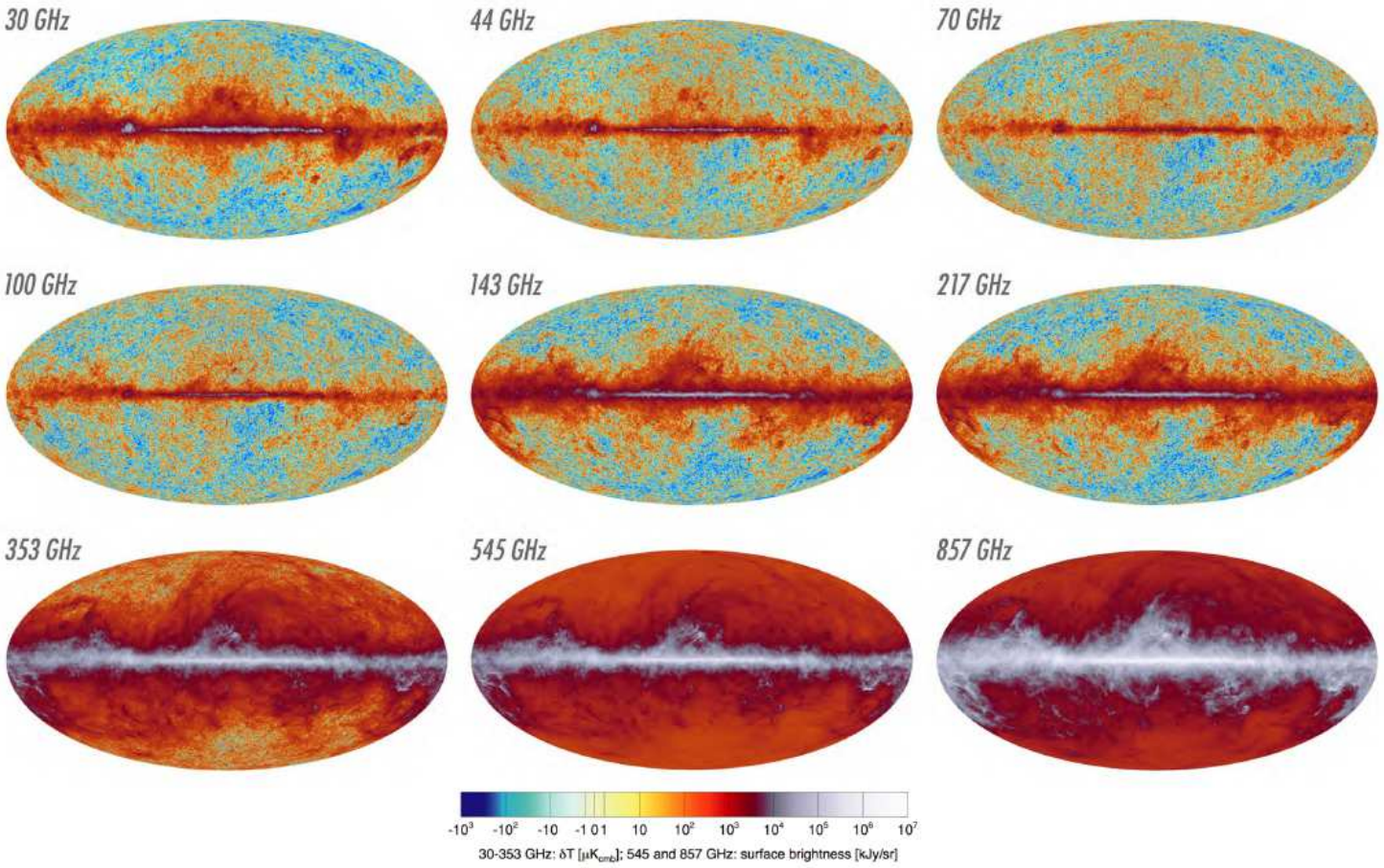

Figure 3: Brightness of the sky in the nine Planck frequency bands. These sky maps are in galactic coordinates so the Milky Way lies horizontally. From [2].

In addition to the CMB, there is microwave radiation from our own galaxy and other galaxies, called *foreground* by those who study CMB. This radiation can be separated from the CMB based on its different electromagnetic spectrum. To enable this *component separation*, Planck observed at 9 different frequency bands; the lowest one centered at 30 GHz and the highest at 857 GHz (Fig. 3). There were two different instruments on Planck, using different technologies to detect the variations in the microwave radiation. The Low Frequency Instrument (LFI) used radiometers for the 30, 44, and 70 GHz bands. The High Frequency Instrument (HFI) used bolometers for the bands from 100 GHz to 857 GHz. HFI is the barrel-shaped instrument at the center in Fig. 2 right panel and LFI was wrapped around it. With the additional help of WMAP and ground-based data 8 different foreground components could be distinguished (Fig. 4).

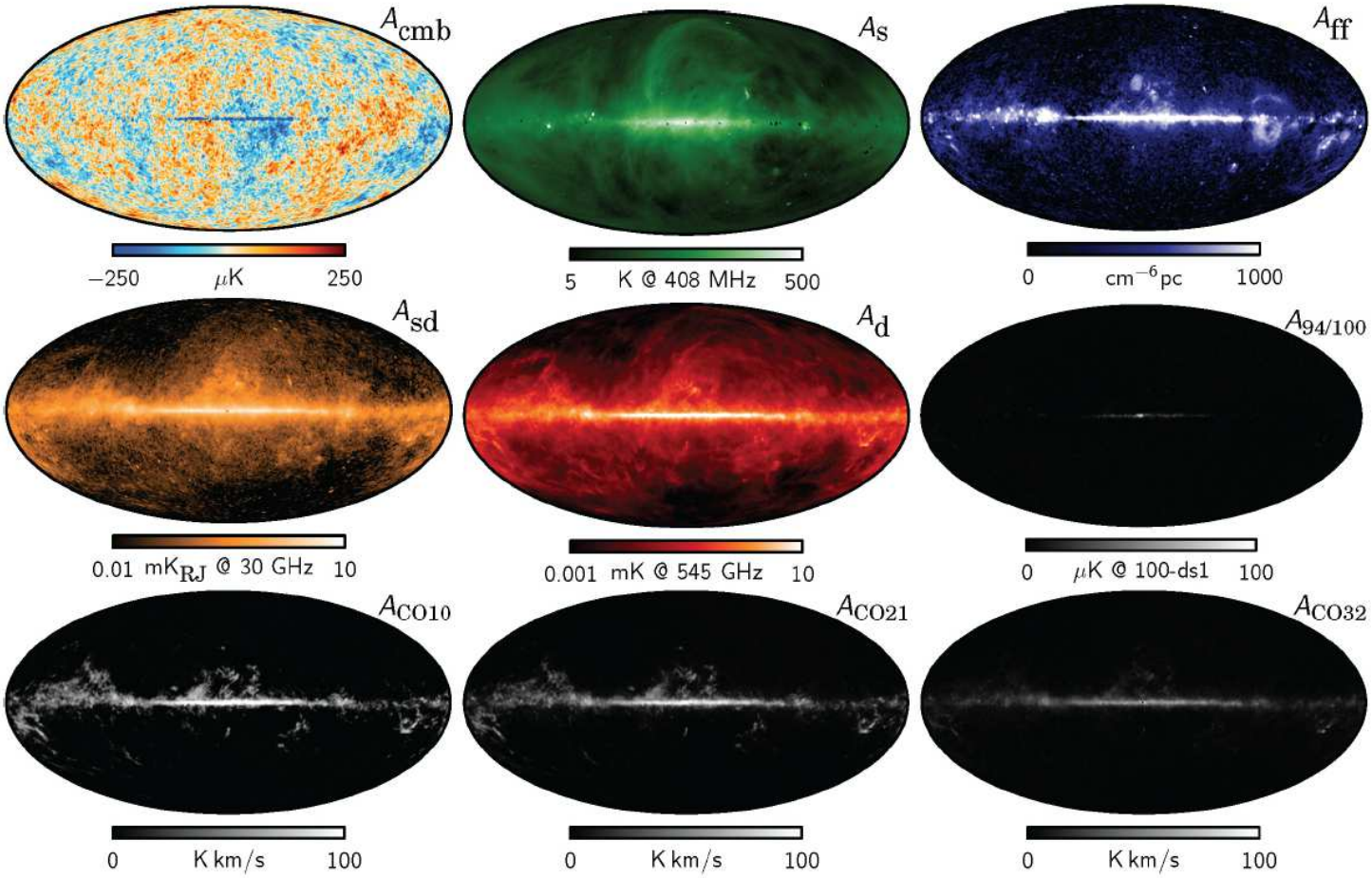

Figure 4: Result from Planck component separation. Also WMAP data and ground-based 408 MHz data was used. The extracted nine different components of the microwave radiation from top left to bottom right are: 1) CMB; 2) synchrotron radiation generated by relativistic cosmic-ray electrons accelerated by the galactic magnetic field; 3) "free-free emission" (bremsstrahlung) from electron-ion collisions; 4) emission from spinning galactic dust grains due to their electric dipole moment; 5) thermal emission from galactic dust (the typical dust temperatures are of order 20 K, so the dust thermal spectrum is peaked at much higher frequencies than CMB); 6) spectral line emission from HCN, CN, HCO, CS, and other molecules; 7) spectral line emission from the CO (carbon monoxide) $J = 1 \to 0$ transition; 8) CO $J = 2 \to 1$ line; 9) CO $J = 3 \to 2$ line (these emission lines from transitions between the four lowest rotation states of the CO molecule map the distribution of carbon monoxide in the Milky Way). From [2].

Figures 5–7 show the observed variation δT in the temperature of the CMB on the sky (red means hotter than average, blue means colder than average).

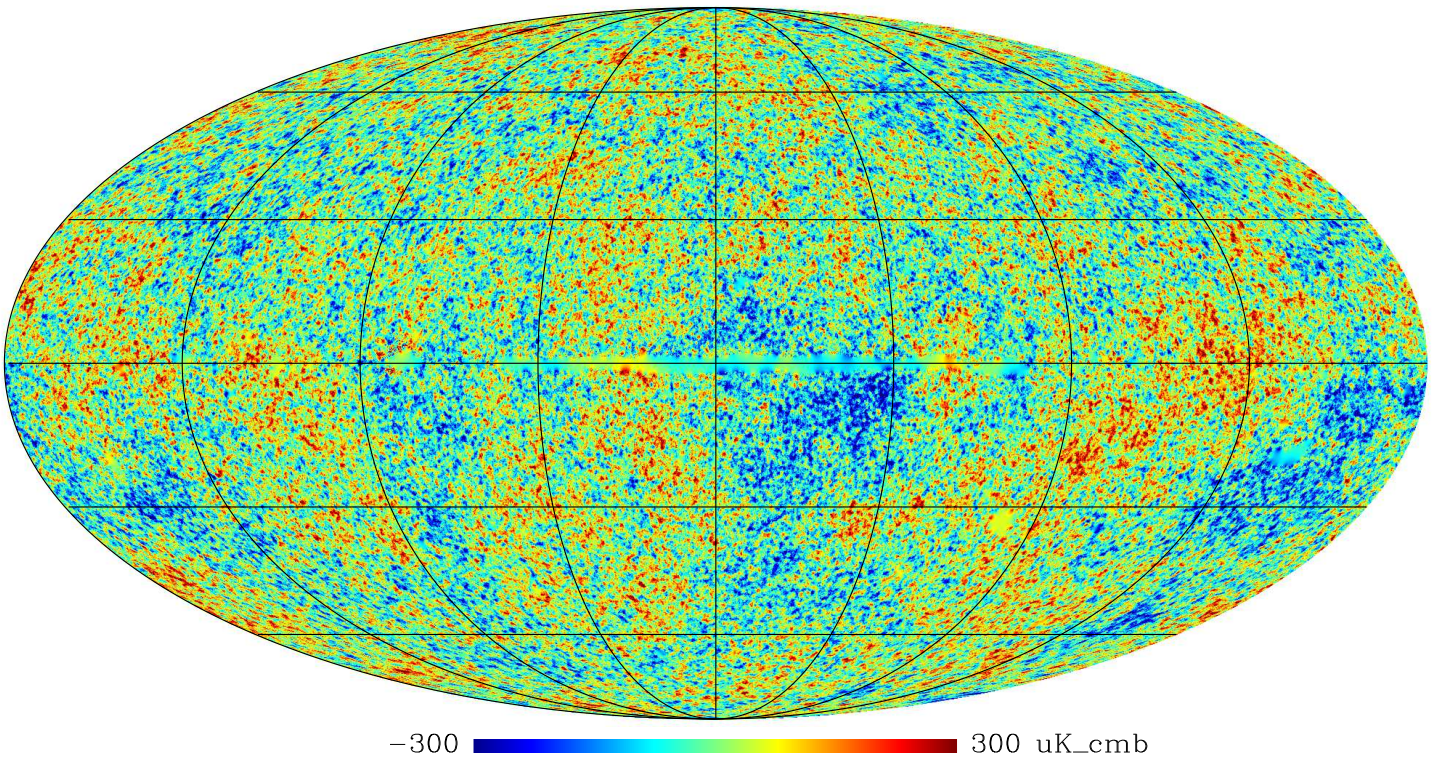

Figure 5: Cosmic microwave background: Fig. 1 reproduced in false color to bring out the patterns more clearly. The color range corresponds to CMB temperature variations from $-300\,\mu$K (blue) to $+300\,\mu$K (red) around the mean temperature. (ESA/Planck data).

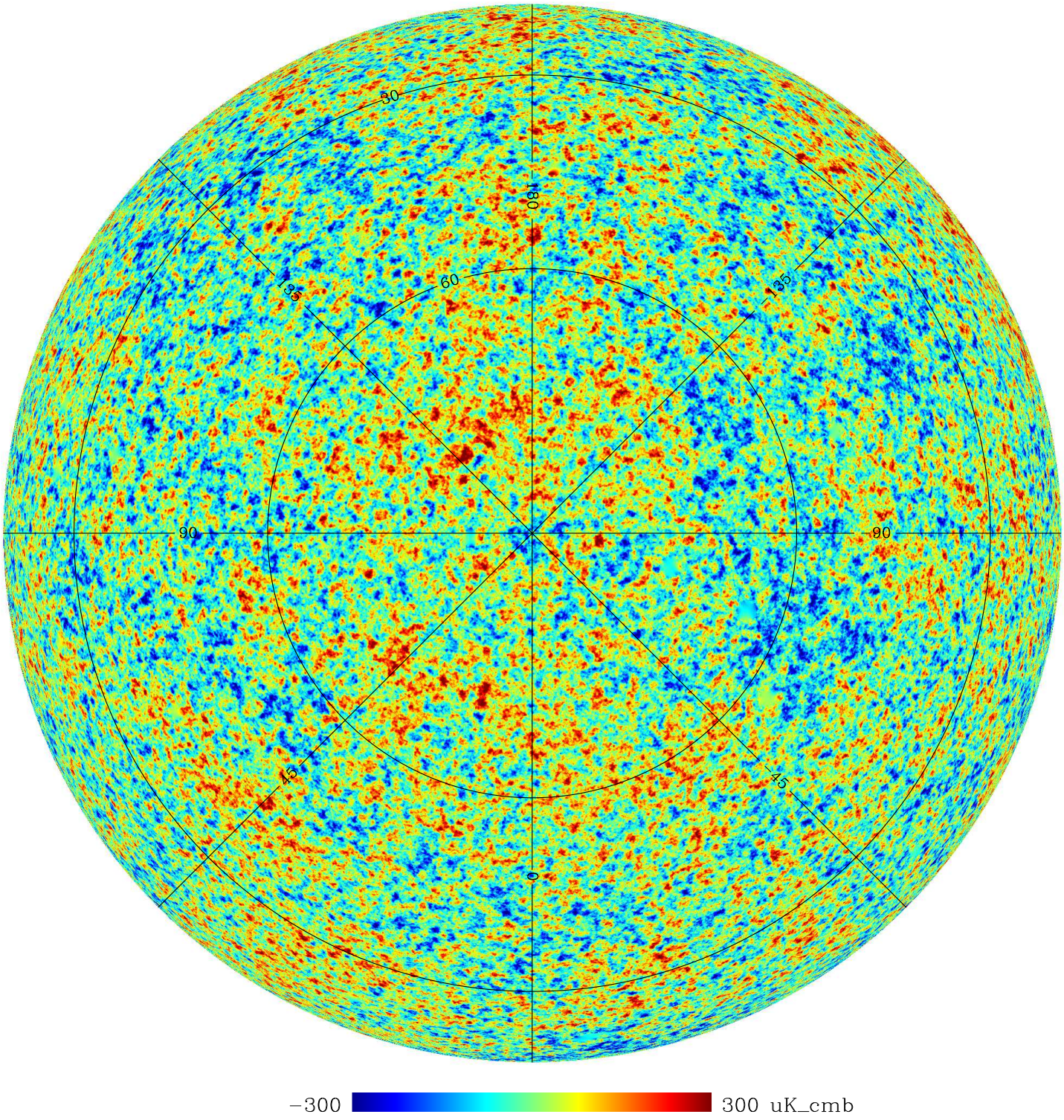

Figure 6: The northern galactic hemisphere of the CMB sky (ESA/Planck data).

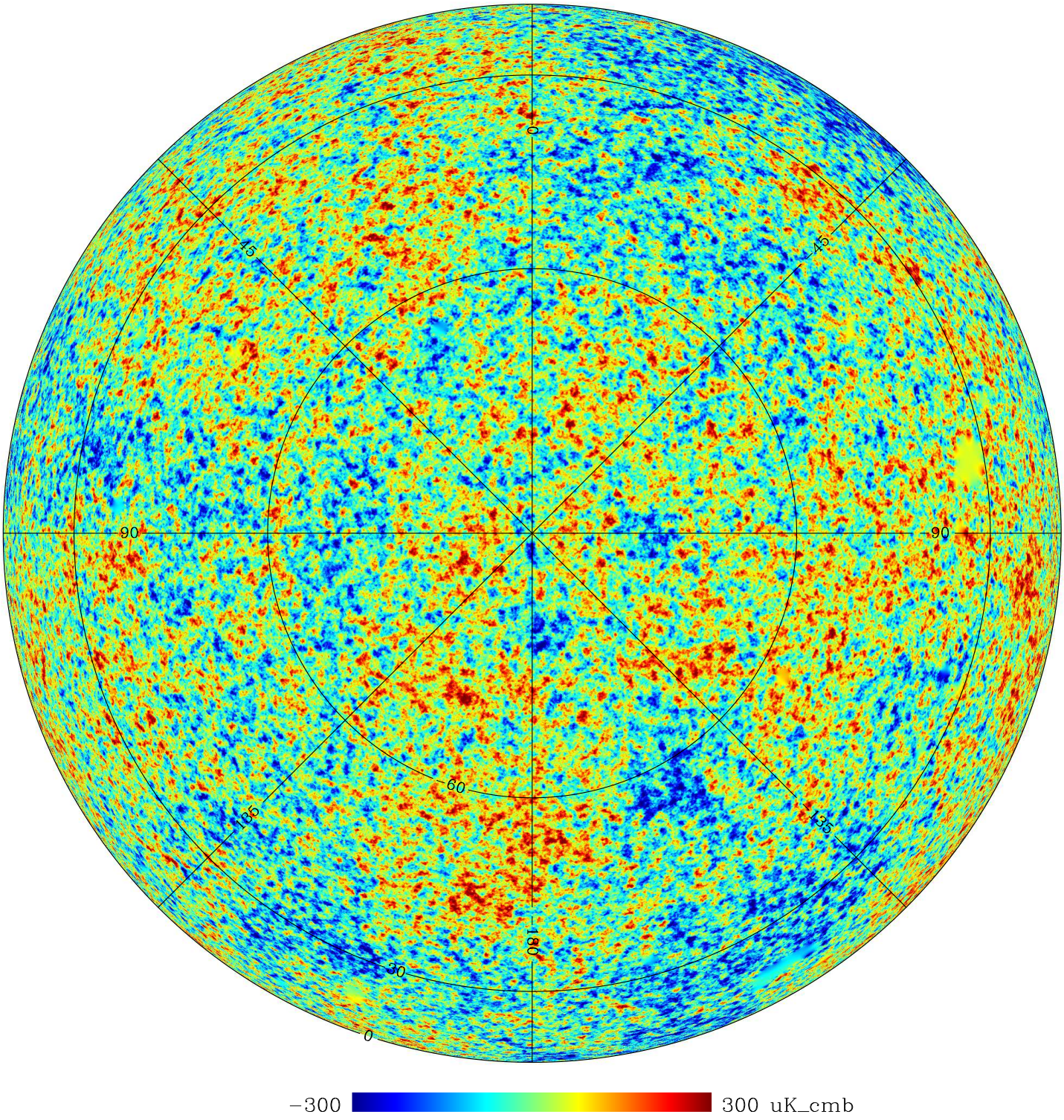

Figure 7: The southern galactic hemisphere of the CMB sky. The conspicuous cold region around $(-150°, -55°)$ is called the Cold Spot. The yellow smooth spot at $(-80°, -35°)$ in galactic coordinates is a region where the CMB is obscured by the Large Magellanic Cloud, and the light blue spot at $(-150°, -20°)$ is due to the Orion Nebula. (ESA/Planck data).

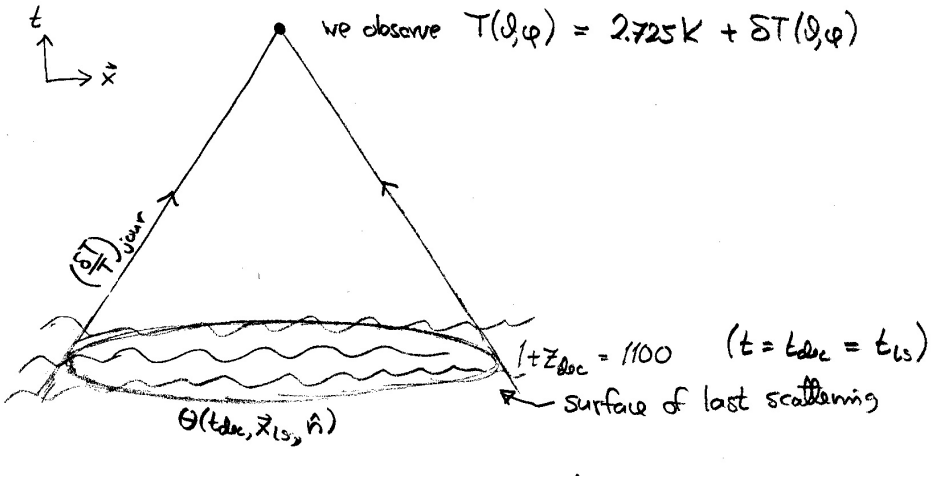

Figure 8: The observed CMB temperature anisotropy gets a contribution from the last scattering surface, $(\delta T/T)_{\rm intr} = \Theta(t_{\rm dec}, \mathbf{x}_{\rm ls}, \hat{\mathbf{n}})$ and from along the photon's journey to us, $(\delta T/T)_{\rm jour}$.

The photons we see as the CMB, have traveled to us from where our past light cone intersects the hypersurface corresponding to the time $t = t_{\rm dec}$ of photon decoupling. This intersection forms a sphere which we shall call the *last scattering surface*.[1] We are at the center of this sphere, except that timewise the sphere is located in the past.

The observed temperature anisotropy is due to two contributions, an *intrinsic* temperature variation at the surface of last scattering and a variation in the redshift the photons have suffered during their "journey" to us,

$$\left(\frac{\delta T}{T}\right)_{\rm obs} = \left(\frac{\delta T}{T}\right)_{\rm intr} + \left(\frac{\delta T}{T}\right)_{\rm jour} . \tag{1}$$

See Fig. 8.

The first term, $\left(\frac{\delta T}{T}\right)_{\rm intr}$ represents the temperature variation of the photon gas at $t = t_{\rm dec}$. We also include in it the Doppler effect from the motion of this photon gas. At that time the larger scales we see in the CMB sky were still outside the horizon, so we have to pay attention to the gauge choice. In fact, the separation of $\delta T/T$ into the two components in Eq. (1) is gauge-dependent. If the time slice $t = t_{\rm dec}$ dips further into the past in some location, it finds a higher temperature, but the photons from there also have a longer way to go and suffer a larger redshift, so that the two effects balance each other. We can calculate in any gauge we want, getting different results for $(\delta T/T)_{\rm intr}$ and $(\delta T/T)_{\rm jour}$ depending on the gauge, but their sum $(\delta T/T)_{\rm obs}$ is gauge independent. It has to be, being an observed quantity.

One might think that $(\delta T/T)_{\rm intr}$ should be equal to zero, since in our earlier discussion of recombination and decoupling we identified decoupling with a particular temperature $T_{\rm dec} \sim 3000\,{\rm K}$. This kind of thinking corresponds to a particular gauge choice where the $t = t_{\rm dec}$ time slice coincides with the $T = T_{\rm dec}$ hypersurface. In this gauge $(\delta T/T)_{\rm intr} = 0$, except for the Doppler effect (we are not going to use this gauge). Anyway, it is not true that all photons have their last scattering exactly when $T = T_{\rm dec}$. Rather they occur during a rather large temperature interval and time period. The zeroth-order (background) time evolution of the temperature of the photon distribution is the same before and after last scattering, $T \propto a^{-1}$, so it does not matter how we draw the artificial separation line, the time slice $t = t_{\rm dec}$ separating the fluid and free particle treatments of the photons. See Fig. 9.

[1] Or the *last scattering sphere*. "Last scattering surface" often refers to the entire $t = t_{\rm dec}$ time slice.

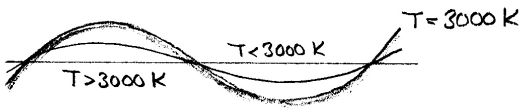

Figure 9: Depending on the gauge, the $T = T_{\rm dec}$ surface may, or (usually) may not coincide with the $t = t_{\rm dec}$ time slice.

9.2 Multipole analysis

The CMB temperature anisotropy is a function over a sphere (the celestial sphere, or the unit sphere of directions $\hat{\mathbf{n}}$). In analogy with the Fourier expansion in 3D space, we separate out the contributions of different angular scales by doing a multipole expansion,

$$\frac{\delta T}{T_0}(\theta,\phi) = \sum a_{\ell m} Y_{\ell m}(\theta,\phi) \tag{2}$$

where the sum runs over $\ell = 1, 2, \ldots \infty$ and $m = -\ell, \ldots, \ell$, giving $2\ell + 1$ values of m for each ℓ. The functions $Y_{\ell m}(\theta,\phi)$ are the *spherical harmonics* (see Fig. 10), which form an orthonormal set of functions over the sphere, so that we can calculate the multipole coefficients $a_{\ell m}$ from

$$a_{\ell m} = \int Y^*_{\ell m}(\theta,\phi)\frac{\delta T}{T_0}(\theta,\phi) d\Omega\,. \tag{3}$$

Definition (2) gives dimensionless $a_{\ell m}$. Often they are defined without the $T_0 = 2.7255\,\mathrm{K}$ in Eq. (2), and then they have the dimension of temperature and are usually given in units of μK. Here θ and ϕ are spherical coordinates, $d\Omega \equiv d\cos\theta d\phi$, θ ranges from 0 to π and ϕ ranges from 0 to 2π.[2]

The sum begins at $\ell = 1$, since $Y_{00} =$ const. and therefore we must have $a_{00} = 0$ for a quantity which represents a deviation from average. The dipole part, $\ell = 1$, is dominated by the Doppler effect due to the motion of the solar system with respect to the last scattering surface, and we cannot separate out from it the *cosmological dipole* caused by large scale perturbations. Therefore we are here interested only in the $\ell \geq 2$ part of the expansion.

Another notation for $Y_{\ell m}(\theta,\phi)$ is $Y_{\ell m}(\hat{\mathbf{n}})$, where $\hat{\mathbf{n}}$ is a unit vector whose direction is specified by the angles θ and ϕ.

9.2.1 Spherical harmonics

We list here some useful properties of the spherical harmonics.

They are orthonormal functions on the sphere, so that

$$\int d\Omega\; Y_{\ell m}(\theta,\phi) Y^*_{\ell' m'}(\theta,\phi) = \delta_{\ell\ell'}\delta_{mm'}\,. \tag{4}$$

They are elementary complex functions and are related to the *associated Legendre functions* $P^m_\ell(x)$ by

$$Y_{\ell m}(\theta,\phi) = (-1)^m \sqrt{\frac{2\ell+1}{4\pi}\frac{(\ell-m)!}{(\ell+m)!}} P^m_\ell(\cos\theta) e^{im\phi}\,. \tag{5}$$

[2]They can also be given in degrees, the *colatitude* θ ranging from 0° (North) to 180° (South) and the *longitude* ϕ from 0° to 360°. There are a number of different astronomical coordinate systems (equatorial, ecliptic, galactic) in use, with their own historical conventions for the coordinate names, symbols, and units. Typically they involve the *latitude* $90° - \theta$ instead of the colatitude, so that North is at +90° and South at −90°, and the longitude is usually given between −180° and +180°, e.g., in Fig. 7.

Legendre polynomials
$P_0(x) = 1$
$P_1(x) = x$
$P_2(x) = \frac{1}{2}(3x^2 - 1)$
$P_3(x) = \frac{1}{2}(5x^3 - 3x)$
$P_4(x) = \frac{1}{8}(35x^4 - 30x^2 + 3)$
Associated Legendre functions $P_\ell^m(x) = P_\ell^m(\cos\theta)$
$P_1^1(x) = \sqrt{1-x^2} = \sin\theta$
$P_2^1(x) = 3x\sqrt{1-x^2} = 3\cos\theta\sin\theta$
$P_2^2(x) = 3(1-x^2) = 3\sin^2\theta$
Spherical harmonics
$Y_0^0(\theta,\phi) = \frac{1}{\sqrt{4\pi}}$
$Y_1^1(\theta,\phi) = -\sqrt{\frac{3}{8\pi}}\sin\theta e^{i\phi}$
$Y_1^0(\theta,\phi) = \sqrt{\frac{3}{4\pi}}\cos\theta$
$Y_2^2(\theta,\phi) = \sqrt{\frac{5}{96\pi}}3\sin^2\theta e^{i2\phi}$
$Y_2^1(\theta,\phi) = -\sqrt{\frac{5}{24\pi}}3\sin\theta\cos\theta e^{i\phi}$
$Y_2^0(\theta,\phi) = \sqrt{\frac{5}{4\pi}}\left(\frac{3}{2}\cos^2\theta - \frac{1}{2}\right)$
Spherical Bessel functions
$j_0(x) = \dfrac{\sin x}{x}$
$j_1(x) = \dfrac{\sin x}{x^2} - \dfrac{\cos x}{x}$
$j_2(x) = \left(\dfrac{3}{x^3} - \dfrac{1}{x}\right)\sin x - \dfrac{3}{x^2}\cos x$

Table 1: Legendre functions, spherical harmonics, and spherical Bessel functions.

Thus the θ-dependence is in $P_\ell^m(\cos\theta)$ and the ϕ-dependence is in $e^{im\phi}$. The functions P_ℓ^m are real and

$$Y_{\ell,-m} = (-1)^m Y_{\ell m}^*\,, \tag{6}$$

so that

$$Y_{\ell 0} = \sqrt{\frac{2\ell+1}{4\pi}}P_\ell(\cos\theta) \qquad \text{is real.} \tag{7}$$

The functions $P_\ell \equiv P_\ell^0$ are called *Legendre polynomials*. See Table 9.2.1 for examples of these functions for $\ell \le 2$.

Summing over the m corresponding to the same multipole number ℓ gives the *addition theorem*

$$\sum_m Y_{\ell m}^*(\theta',\phi')Y_{\ell m}(\theta,\phi) = \frac{2\ell+1}{4\pi}P_\ell(\cos\vartheta)\,, \tag{8}$$

where ϑ is the angle between $\hat{\mathbf{n}} = (\theta, \phi)$ and $\hat{\mathbf{n}}' = (\theta', \phi')$, i.e., $\hat{\mathbf{n}} \cdot \hat{\mathbf{n}}' = \cos\vartheta$. For $\hat{\mathbf{n}} = \hat{\mathbf{n}}'$ this becomes

$$\sum_m |Y_{\ell m}(\theta, \phi)|^2 = \frac{2\ell + 1}{4\pi} \tag{9}$$

(since $P_\ell(1) = 1$ always).

We shall also need the expansion of a plane wave in terms of spherical harmonics,

$$e^{i\mathbf{k}\cdot\mathbf{x}} = 4\pi \sum_{\ell m} i^\ell j_\ell(kx) Y_{\ell m}(\hat{\mathbf{x}}) Y^*_{\ell m}(\hat{\mathbf{k}}) \,. \tag{10}$$

Here $\hat{\mathbf{x}}$ and $\hat{\mathbf{k}}$ are the unit vectors in the directions of $\mathbf{x}$ and $\mathbf{k}$, and the j_ℓ are the spherical Bessel functions.

9.2.2 Theoretical angular power spectrum

The CMB anisotropy is due to primordial perturbations, and therefore it reflects their Gaussian nature. Because one gets the values of the $a_{\ell m}$ from the other perturbation quantities through linear equations (in first-order perturbation theory), the $a_{\ell m}$ are also (complex) Gaussian random variables. Since they represent a deviation from the average temperature, their expectation value is zero,

$$\langle a_{\ell m} \rangle = 0 \,. \tag{11}$$

From statistical isotropy follows that the $a_{\ell m}$ are independent random variables so that

$$\langle a_{\ell m} a^*_{\ell' m'} \rangle = 0 \qquad \text{if } \ell \neq \ell' \text{ or } m \neq m'. \tag{12}$$

Since $\delta T/T_0$ is real,

$$a_{\ell,-m} = (-1)^m a^*_{\ell,m} \,. \tag{13}$$

Although thus $a_{\ell,-m}$ and $a_{\ell m}$ are not independent of each other, we still have $\langle a_{\ell m} a^*_{\ell,-m} \rangle = 0$ (**exercise**), so that (12) is satisfied even in this case. For each ℓ, there are $2\ell + 1$ independent real random variables: $a_{\ell 0}$ (which is always real), and $\operatorname{Re} a_{\ell m}$ and $\operatorname{Im} a_{\ell m}$ for $m = 1, \ldots, \ell$.

The quantity we want to calculate from theory is the variance $\langle |a_{\ell m}|^2 \rangle$ to get a prediction for the typical size of the $a_{\ell m}$. From statistical isotropy also follows that these expectation values depend only on ℓ not m. (The ℓ are related to the angular size of the anisotropy pattern, whereas the m are related to "orientation" or "pattern". See Fig. 10.) Since $\langle |a_{\ell m}|^2 \rangle$ is independent of m, we can define

$$C_\ell \equiv \langle |a_{\ell m}|^2 \rangle = \frac{1}{2\ell + 1} \sum_m \langle |a_{\ell m}|^2 \rangle \,, \tag{14}$$

and altogether we have

$$\langle a_{\ell m} a^*_{\ell' m'} \rangle = \delta_{\ell\ell'} \delta_{mm'} C_\ell \,. \tag{15}$$

This function C_ℓ (of integers $\ell \geq 2$) is called the (theoretical) *angular power spectrum*. It is analogous to the power spectrum $\mathcal{P}(k)$ of density perturbations. For Gaussian perturbations, the C_ℓ contains all the statistical information about the CMB temperature anisotropy. And this is all we can predict from theory. Thus the analysis of the CMB anisotropy consists of calculating the angular power spectrum from the observed CMB (a map like Figure 5) and comparing it to the C_ℓ predicted by theory.[3]

[3] In addition to the temperature anisotropy, the CMB also has another property, its polarization. There are two additional power spectra related to the polarization, C_ℓ^{EE} and C_ℓ^{BB}, and one related to the correlation between temperature and polarization, C_ℓ^{TE}.

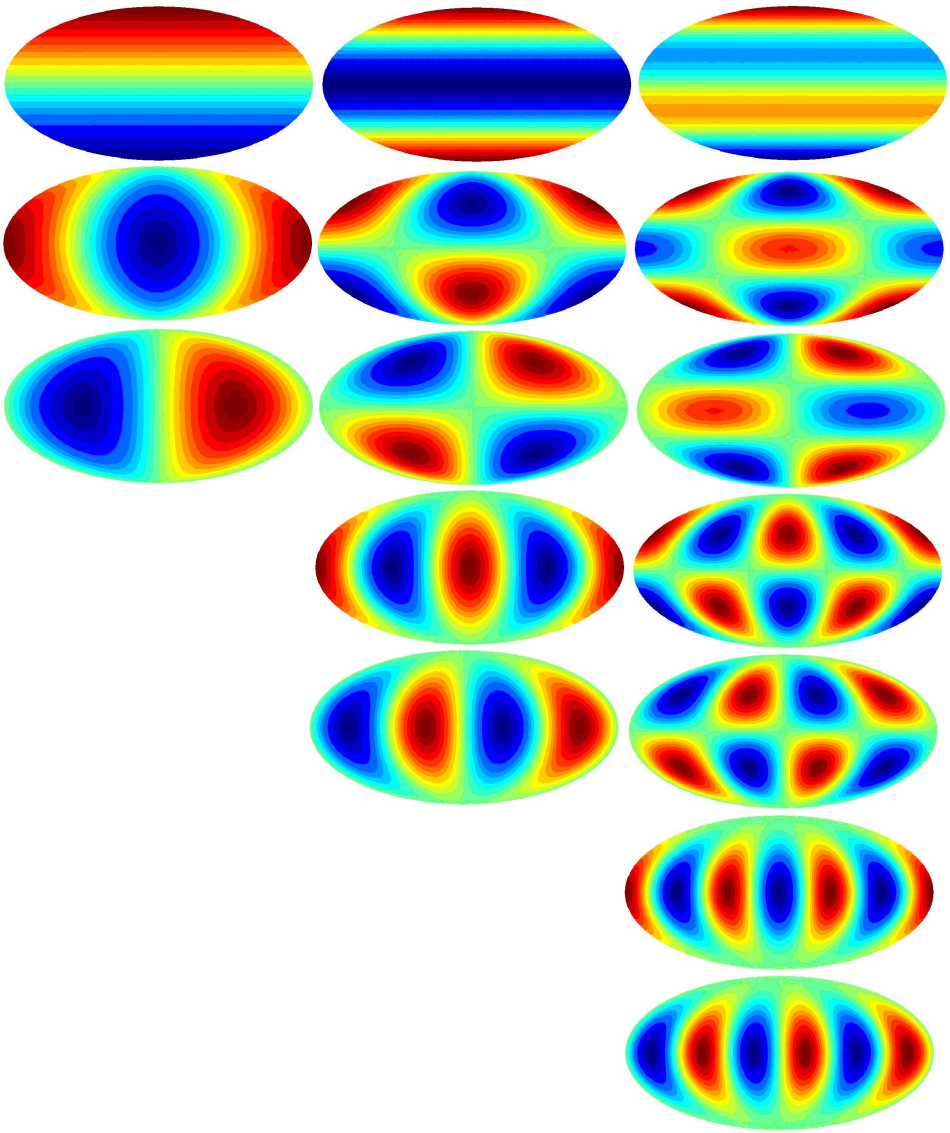

Figure 10: The three lowest multipoles $\ell = 1, 2, 3$ of spherical harmonics. Left column: Y_{10}, $\mathrm{Re}\, Y_{11}$, $\mathrm{Im}\, Y_{11}$. Middle column: Y_{20}, $\mathrm{Re}\, Y_{21}$, $\mathrm{Im}\, Y_{21}$, $\mathrm{Re}\, Y_{22}$, $\mathrm{Im}\, Y_{22}$. Right column: Y_{30}, $\mathrm{Re}\, Y_{31}$, $\mathrm{Im}\, Y_{31}$, $\mathrm{Re}\, Y_{32}$, $\mathrm{Im}\, Y_{32}$, $\mathrm{Re}\, Y_{33}$, $\mathrm{Im}\, Y_{33}$. Figure by Ville Heikkilä.

Just like the 3D density power spectrum $\mathcal{P}(k)$ gives the contribution of scale k to the density variance $\langle\delta(\mathbf{x})^2\rangle$, the angular power spectrum C_ℓ is related to the contribution of multipole ℓ to the temperature variance,

$$\begin{aligned}\left\langle\left(\frac{\delta T(\theta,\phi)}{T}\right)^2\right\rangle &= \left\langle\sum_{\ell m} a_{\ell m}Y_{\ell m}(\theta,\phi)\sum_{\ell' m'} a^*_{\ell' m'}Y^*_{\ell' m'}(\theta,\phi)\right\rangle \\ &= \sum_{\ell\ell'}\sum_{mm'} Y_{\ell m}(\theta,\phi)Y^*_{\ell' m'}(\theta,\phi)\langle a_{\ell m}a^*_{\ell' m'}\rangle \\ &= \sum_\ell C_\ell\sum_m |Y_{\ell m}(\theta,\phi)|^2 \;=\; \sum_\ell \frac{2\ell+1}{4\pi}C_\ell\,, \end{aligned} \tag{16}$$

where we used (15) and (9).

Thus, if we plot $(2\ell+1)C_\ell/4\pi$ on a linear ℓ scale, or $\ell(2\ell+1)C_\ell/4\pi$ on a logarithmic ℓ scale, the area under the curve gives the temperature variance, i.e., the expectation value for the squared deviation from the average temperature. It has become customary to plot the angular power spectrum as $\ell(\ell+1)C_\ell/2\pi$, which is neither of these, but for large ℓ approximates the second case. The reason for this custom is explained later.

Equation (16) represents the expectation value from theory and thus it is the same for all directions θ,ϕ. The actual, "realized", value of course varies from one direction θ,ϕ to another. We can imagine an ensemble of universes, otherwise like our own, but representing a different realization of the same random process of producing the primordial perturbations. Then $\langle\ \rangle$ represents the average over such an ensemble.

Equation(16) can be generalized to the angular correlation function (**exercise**)

$$C(\vartheta) \;\equiv\; \left\langle\frac{\delta T(\hat{\mathbf{n}})}{T}\frac{\delta T(\hat{\mathbf{n}}')}{T}\right\rangle \;=\; \frac{1}{4\pi}\sum_\ell (2\ell+1)C_\ell P_\ell(\cos\vartheta),\,, \tag{17}$$

where ϑ is the angle between $\hat{\mathbf{n}}$ and $\hat{\mathbf{n}}'$.

9.2.3 Observed angular power spectrum

Theory predicts expectation values $\langle|a_{\ell m}|^2\rangle$ from the random process responsible for the CMB anisotropy, but we can observe only one realization of this random process, the set $\{a_{\ell m}\}$ of our CMB sky. We define the *observed* angular power spectrum as the average

$$\widehat{C}_\ell = \frac{1}{2\ell+1}\sum_m |a_{\ell m}|^2 \tag{18}$$

of these observed values.

The variance of the observed temperature anisotropy is the average of $\left(\frac{\delta T(\theta,\phi)}{T}\right)^2$ over the celestial sphere,

$$\begin{aligned}\frac{1}{4\pi}\int\left[\frac{\delta T(\theta,\phi)}{T}\right]^2 d\Omega &= \frac{1}{4\pi}\int d\Omega\sum_{\ell m} a_{\ell m}Y_{\ell m}(\theta,\phi)\sum_{\ell' m'} a^*_{\ell' m'}Y^*_{\ell' m'}(\theta,\phi) \\ &= \frac{1}{4\pi}\sum_{\ell m}\sum_{\ell' m'} a_{\ell m}a^*_{\ell' m'}\underbrace{\int Y_{\ell m}(\theta,\phi)Y^*_{\ell' m'}(\theta,\phi)d\Omega}_{\delta_{\ell\ell'}\delta_{mm'}} \\ &= \frac{1}{4\pi}\sum_\ell\underbrace{\sum_m |a_{\ell m}|^2}_{(2\ell+1)\widehat{C}_\ell} \;=\; \sum_\ell\frac{2\ell+1}{4\pi}\widehat{C}_\ell\,. \end{aligned} \tag{19}$$

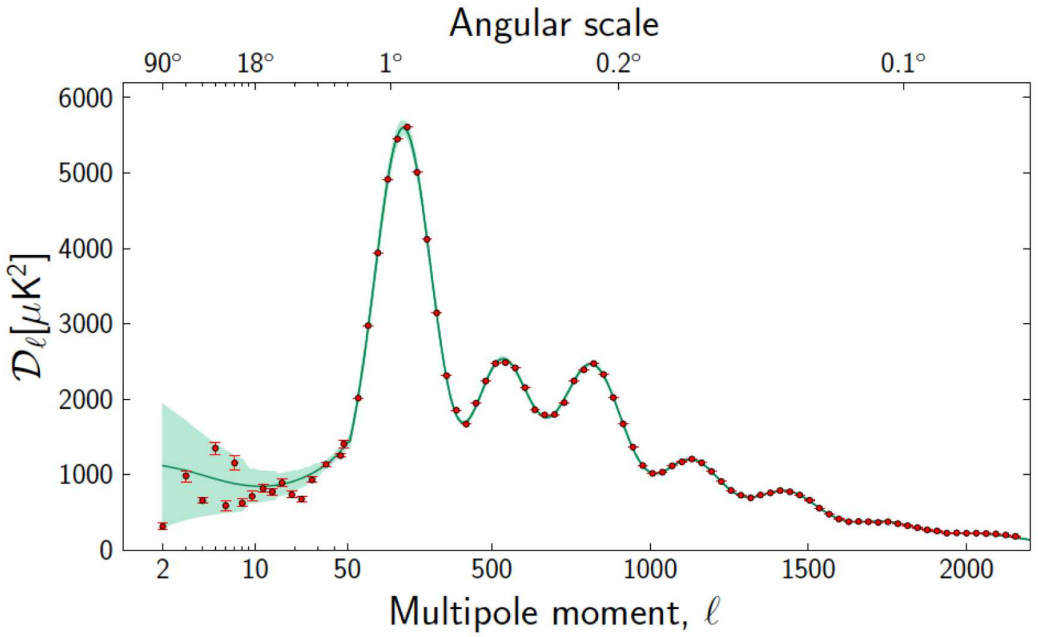

Figure 11: The angular power spectrum $\widehat{C}_\ell$ as observed by Planck. The observational results are the red data points with small error bars. The green curve is the theoretical C_ℓ from a best-fit model, and the light green band around it represents the cosmic variance corresponding to this C_ℓ. The quantity plotted is actually $\mathcal{D}_\ell \equiv T_0^2[\ell(\ell+1)/(2\pi)]C_\ell$. Note that the ℓ-axis is logarithmic until 50 and linear after that. (This is Fig. 21 of [1].)

Contrast this with (16), which gives the variance of $\delta T/T$ at an arbitrary location on the sky over different realizations of the random process which produced the primordial perturbations; whereas (19) gives the variance of $\delta T/T$ of our given sky over the celestial sphere.

9.2.4 Cosmic Variance

The expectation value of the observed spectrum $\widehat{C}_\ell$ is equal to C_ℓ, the *theoretical* spectrum of Eq. (14), i.e.,

$$\langle \widehat{C}_\ell \rangle = C_\ell \quad \Rightarrow \quad \langle \widehat{C}_\ell - C_\ell \rangle = 0\,, \tag{20}$$

but its actual, realized, value is not, although we expect it to be close. The expected squared difference between $\widehat{C}_\ell$ and C_ℓ is called the *cosmic variance* (of C_ℓ). We can calculate it using the properties of (complex) Gaussian random variables (**exercise**). The answer is

$$\langle (\widehat{C}_\ell - C_\ell)^2 \rangle = \frac{2}{2\ell+1} C_\ell^2\,. \tag{21}$$

We see that the expected relative difference between $\widehat{C}_\ell$ and C_ℓ is smaller for higher ℓ. This is because we have a larger (size $2\ell+1$) statistical sample of $a_{\ell m}$ available for calculating the $\widehat{C}_\ell$.

The cosmic variance limits the accuracy of comparison of CMB observations with theory, especially for large scales (low ℓ). See Fig. 11.

9.3 Multipoles and scales

9.3.1 Rough correspondence

The different multipole numbers ℓ correspond to different angular scales, low ℓ to large scales and high ℓ to small scales. Examination of the functions $Y_{\ell m}(\theta, \phi)$ reveals that they have an oscillatory pattern on the sphere, so that there are typically ℓ "wavelengths" of oscillation around a full great circle of the sphere. See Figs. 10 and 12.

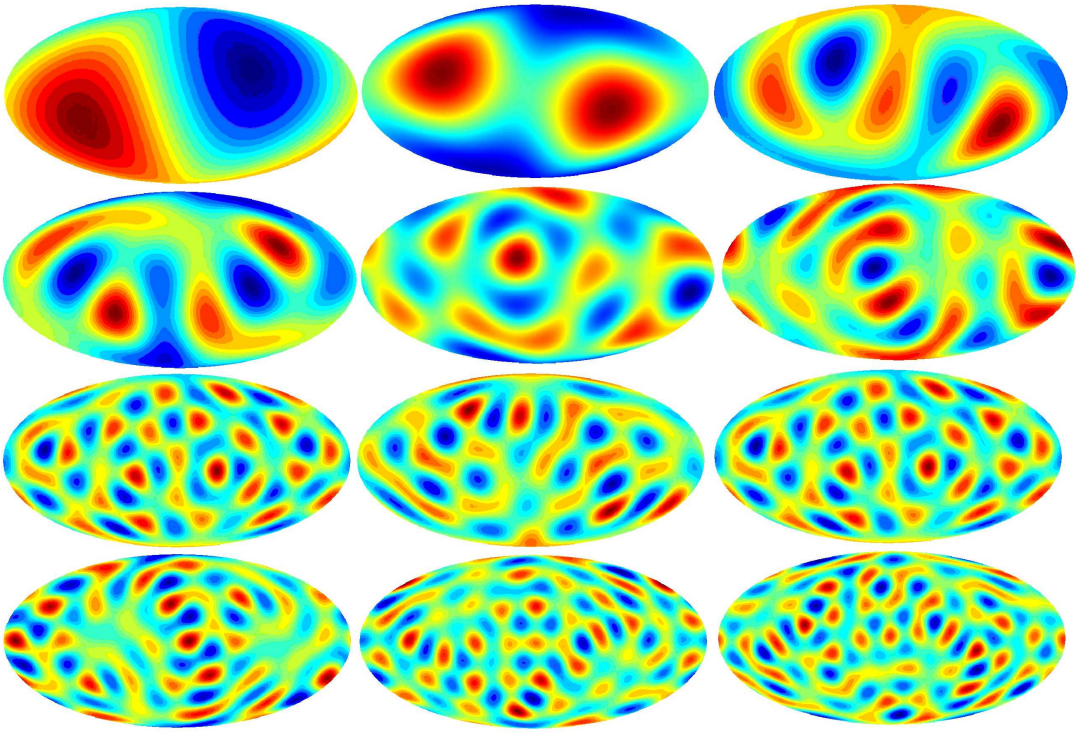

Figure 12: Randomly generated skies containing only a single multipole ℓ. Starting from top left: $\ell = 1$ (dipole only), 2 (quadrupole only), 3 (octupole only), 4, 5, 6, 7, 8, 9, 10, 11, 12. Figure by Ville Heikkilä.

Thus the angle corresponding to this wavelength is

$$\vartheta_\lambda = \frac{2\pi}{\ell} = \frac{360^\circ}{\ell}\,. \tag{22}$$

See Fig. 13. The angle corresponding to a "half-wavelength", i.e., the separation between a neighboring minimum and maximum is then

$$\vartheta_{\rm res} = \frac{\pi}{\ell} = \frac{180^\circ}{\ell}\,. \tag{23}$$

This is the angular resolution required of the microwave detector for it to be able to resolve the angular power spectrum up to this ℓ.

For example, COBE had an angular resolution of 7° allowing a measurement up to $\ell = 180/7 = 26$, WMAP had resolution 0.23° reaching to $\ell = 180/0.23 = 783$, and Planck had resolution 5′, allowing the measurement of C_ℓ up to $\ell = 2160$.[4]

[4] In reality, there is no sharp cut-off at a particular ℓ, the observational error bars just blow up rapidly around this value of ℓ.

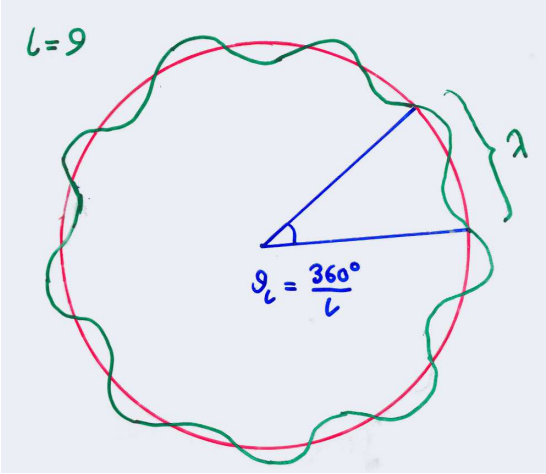

Figure 13: The rough correspondence between multipoles ℓ and angles.

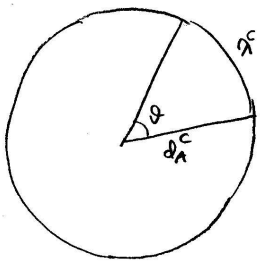

Figure 14: The comoving angular diameter distance relates the comoving size of an object and the angle in which we see it.

The angles on the sky are related to actual physical distances via the *angular diameter distance* d_A, defined as the ratio of the physical length (transverse to the line of sight) and the angle it covers (see Chapter 3),

$$d_A \equiv \frac{\lambda_{\rm phys}}{\vartheta}\,. \tag{24}$$

Likewise, we defined the *comoving angular diameter distance* d_A^c by

$$d_A^c \equiv \frac{\lambda^c}{\vartheta} \tag{25}$$

where $\lambda^c = a^{-1}\lambda_{\rm phys} = (1+z)\lambda_{\rm phys}$ is the corresponding comoving length. Thus $d_A^c = a^{-1}d_A = (1+z)d_A$. See Fig. 14.

Consider now the Fourier modes of our earlier perturbation theory discussion. A mode with comoving wavenumber k has comoving wavelength $\lambda^c = 2\pi/k$. Thus this mode should show up as a pattern on the CMB sky with angular size

$$\vartheta_\lambda = \frac{\lambda^c}{d_A^c} = \frac{2\pi}{k d_A^c} = \frac{2\pi}{\ell}\,. \tag{26}$$

For the last equality we used the relation (22). From it we get that the modes with wavenumber k contribute mostly to multipoles around

$$\ell = k d_A^c\,. \tag{27}$$

9.3.2 Exact treatment

The above matching of wavenumbers with multipoles was of course rather naive, for two reasons:

1. The description of a spherical harmonic $Y_{\ell m}$ having an "angular wavelength" of $2\pi/\ell$ is just a crude characterization. See Fig. 12.

2. The modes $\mathbf{k}$ are not wrapped around the sphere of last scattering, but the wave vector forms a different angle with the sphere at different places.

The following precise discussion applies only for the case of a flat universe ($K = 0$ FRW universe as the background), where one can Fourier expand functions on a time slice. We start from the expansion of the plane wave in terms of spherical harmonics, for which we have the result, Eq. (10),

$$e^{i\mathbf{k}\cdot\mathbf{x}} = 4\pi \sum_{\ell m} i^\ell j_\ell(kx) Y_{\ell m}(\hat{\mathbf{x}}) Y^*_{\ell m}(\hat{\mathbf{k}}) \,, \tag{28}$$

where the j_ℓ are spherical Bessel functions.

Consider now some function

$$f(\mathbf{x}) = \sum_{\mathbf{k}} f_{\mathbf{k}} e^{i\mathbf{k}\cdot\mathbf{x}} \tag{29}$$

on the $t = t_{\rm dec}$ time slice. We want the multipole expansion of the values of this function on the last scattering sphere. See Fig. 15. These are the values $f(x\hat{\mathbf{x}})$, where $x \equiv |\mathbf{x}|$ has a constant value, the (comoving) radius of this sphere. Thus

$$\begin{aligned} a_{\ell m} &= \int d\Omega_x Y^*_{\ell m}(\hat{\mathbf{x}}) f(x\hat{\mathbf{x}}) \\ &= \sum_{\mathbf{k}} \int d\Omega_x Y^*_{\ell m}(\hat{\mathbf{x}}) f_{\mathbf{k}} e^{i\mathbf{k}\cdot\mathbf{x}} \\ &= 4\pi \sum_{\mathbf{k}} \sum_{\ell' m'} \int d\Omega_x f_{\mathbf{k}} Y^*_{\ell m}(\hat{\mathbf{x}}) i^{\ell'} j_{\ell'}(kx) Y_{\ell' m'}(\hat{\mathbf{x}}) Y^*_{\ell' m'}(\hat{\mathbf{k}}) \\ &= 4\pi i^\ell \sum_{\mathbf{k}} f_{\mathbf{k}} j_\ell(kx) Y^*_{\ell m}(\hat{\mathbf{k}}) \,, \end{aligned} \tag{30}$$

where we used the orthonormality of the spherical harmonics. The corresponding result for a Fourier transform $f(\mathbf{k})$ is

$$a_{\ell m} = \frac{4\pi i^\ell}{(2\pi)^3} \int d^3k f(\mathbf{k}) j_\ell(kx) Y^*_{\ell m}(\hat{\mathbf{k}}) \,. \tag{31}$$

The j_ℓ are oscillating functions with decreasing amplitude. For large values of ℓ the position of the first (and largest) maximum is near $kx = \ell$ (see Fig. 16).

Thus the $a_{\ell m}$ pick a large contribution from those Fourier modes $\mathbf{k}$ where

$$kx \sim \ell \,. \tag{32}$$

In a flat universe the comoving distance x (from our location to the sphere of last scattering) and the comoving angular diameter distance d_A^c are equal, so we can write this result as

$$kd_A^c \sim \ell \,. \tag{33}$$

The conclusion is that a given multipole ℓ acquires a contribution from modes with a range of wavenumbers, but most of the contribution comes from near the value given by Eq. (27). This concentration is tighter for larger ℓ.

We shall use Eq. (27) for qualitative purposes in the following discussion.

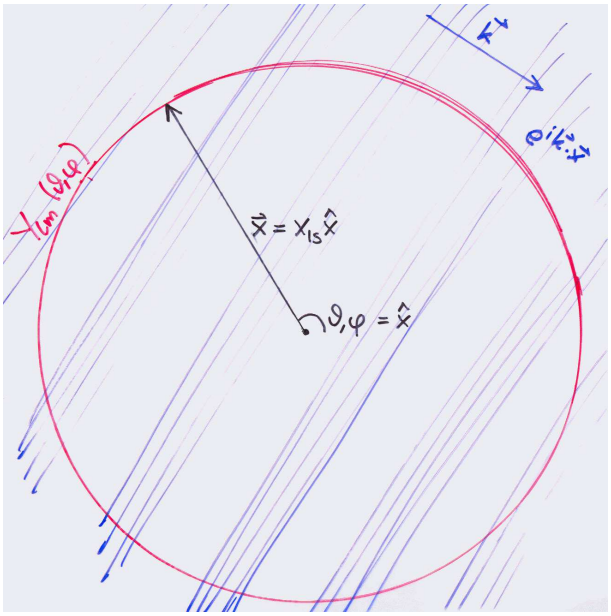

Figure 15: A plane wave intersecting the last scattering sphere.

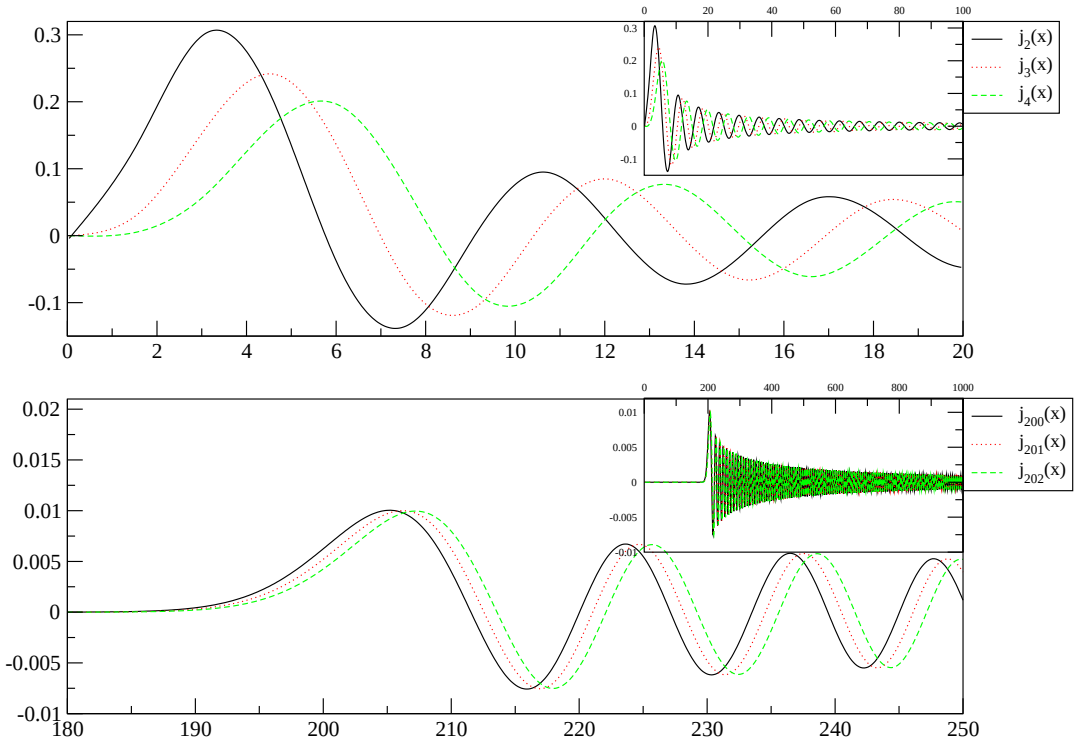

Figure 16: Spherical Bessel functions $j_\ell(x)$ for $\ell = 2$, 3, 4, 200, 201, and 202. Note how the first and largest peak is near $x = \ell$ (but to be precise, at a slightly larger value). Figure by R. Keskitalo.

9.4 Important distance scales on the last scattering surface

9.4.1 Angular diameter distance to last scattering

In Chapter 3 we derived the formula for the comoving distance to redshift z,

$$d^c(z) = H_0^{-1} \int_{\frac{1}{1+z}}^{1} \frac{da}{\sqrt{\Omega_0(a-a^2) - \Omega_\Lambda(a-a^4) + a^2}} \tag{34}$$

(where we have approximated $\Omega_0 \approx \Omega_m + \Omega_\Lambda$) and the corresponding comoving angular diameter distance

$$d_A^c(z) = f_K\left(d^c(z)\right) , \tag{35}$$

where

$$f_K(x) \equiv \begin{cases} K^{-1/2}\sin(K^{1/2}x)\,, & K>0 \\ x\,, & K=0 \\ |K|^{-1/2}\sinh(|K|^{1/2}x)\,, & K<0\,. \end{cases} \tag{36}$$

We also define

$$f_k(x) \equiv \begin{cases} \sin x\,, & k=1 \\ x\,, & k=0 \\ \sinh x\,, & k=-1\,. \end{cases} \tag{37}$$

For the flat universe ($K = k = 0$, $\Omega_0 = 1$), the comoving angular diameter distance is equal to the comoving distance,

$$d_A^c(z) = d^c(z) \qquad (K=0)\,. \tag{38}$$

For the open ($K < 0$, $\Omega_0 < 1$) and closed ($K > 0$, $\Omega_0 > 1$) cases we can write Eq. (35) as

$$\begin{aligned} d_A^c(z) &= \frac{H_0^{-1}}{\sqrt{|\Omega_k|}}\, f_k\left(\frac{\sqrt{|\Omega_k|}}{H_0^{-1}}\, d^c(z)\right) \\ &= H_0^{-1}\frac{1}{\sqrt{|\Omega_k|}}\, f_k\left(\sqrt{|\Omega_k|}\int_{\frac{1}{1+z}}^{1} \frac{da}{\sqrt{\Omega_0(a-a^2) - \Omega_\Lambda(a-a^4) + a^2}}\right) . \end{aligned} \tag{39}$$

Thus $d_A^c(z) \propto H_0^{-1}$, and has some more complicated dependence on Ω_0 and Ω_Λ (or on Ω_m and Ω_Λ).

We are now interested in the distance to the last scattering sphere, i.e., $d_A^c(z_{\rm dec})$, where $z_{\rm dec} \approx 1090$.

For the simplest case, $\Omega_\Lambda = 0$, $\Omega_m = 1$, the integral gives

$$d_A^c(z_{\rm dec}) = H_0^{-1}\int_{\frac{1}{1+z}}^{1} \frac{dx}{\sqrt{x}} = 2H_0^{-1}\left(1 - \frac{1}{\sqrt{1+z_{\rm dec}}}\right) = 1.94 H_0^{-1} \approx 2H_0^{-1}\,, \tag{40}$$

where the last approximation corresponds to ignoring the contribution from the lower limit.

We shall consider two more general cases, of which the above is a special case of both:

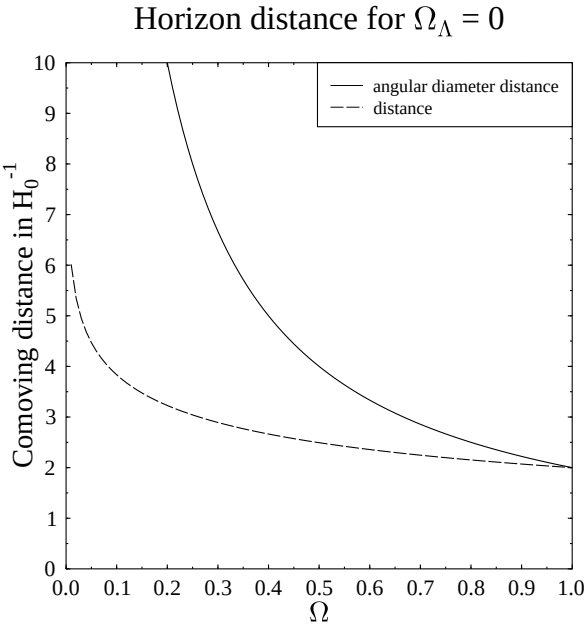

Figure 17: The comoving distance $d^c(z=\infty)$ (dashed) and the comoving angular diameter distance $d_A^c(z=\infty)$ (solid) to the horizon in matter-only open universe. The vertical axis is the distance in units of Hubble distance H_0^{-1} and the horizontal axis is the density parameter $\Omega_0 = \Omega_m$. The distances to last scattering, $d^c(z_{\rm dec})$ and $d_A^c(z_{\rm dec})$ are a few per cent less.

a) Open universe with no dark energy: $\Omega_\Lambda = 0$ and $\Omega_m = \Omega_0 < 1$. Now the integral gives

$$\begin{aligned} d_A^c(z_{\rm dec}) &= \frac{H_0^{-1}}{\sqrt{1-\Omega_m}} \sinh\left(\sqrt{1-\Omega_m}\int_{\frac{1}{1+z}}^1 \frac{dx}{\sqrt{(1-\Omega_m)x^2+\Omega_m x}}\right) \\ &= \frac{H_0^{-1}}{\sqrt{1-\Omega_m}} \sinh\left(\int_{\frac{1}{1+z}}^1 \frac{dx}{\sqrt{x^2+\frac{\Omega_m}{1-\Omega_m}x}}\right) \\ &= \frac{H_0^{-1}}{\sqrt{1-\Omega_m}} \sinh\left(2\,\mathrm{arsinh}\sqrt{\frac{1-\Omega_m}{\Omega_m}} - 2\,\mathrm{arsinh}\sqrt{\frac{1-\Omega_m}{\Omega_m}\frac{1}{1+z_{\rm dec}}}\right) \\ &\approx \frac{H_0^{-1}}{\sqrt{1-\Omega_m}} \sinh\left(2\,\mathrm{arsinh}\sqrt{\frac{1-\Omega_m}{\Omega_m}}\right) \;=\; 2\frac{H_0^{-1}}{\Omega_m}\,, \end{aligned} \tag{41}$$

where again the approximation ignores the contribution from the lower limit (i.e., it actually gives the angular diameter distance to the horizon, $d_A^c(z=\infty)$, in a model where we ignore the effect of other energy density components besides matter). In the last step we used $\sinh 2x = 2\sinh x\cosh x = 2\sinh x\sqrt{1+\sinh^2 x}$. We show this result (together with $d^c(z=\infty)$) in Fig. 17.

b) Flat universe with vacuum energy, $\Omega_\Lambda + \Omega_m = 1$. Here the integral does not give an elementary function, but a reasonable approximation, which we shall use in the following, is

$$d_A^c(z_{\rm dec}) = d^c(z_{\rm dec}) \approx \frac{2}{\Omega_m^{0.4}} H_0^{-1}\,. \tag{42}$$

The comoving distance $d_c(z_{\rm dec})$ depends on the expansion history of the universe. The longer it takes for the universe to cool from $T_{\rm dec}$ to T_0 (i.e., to expand by the factor $1+z_{\rm dec}$), the longer

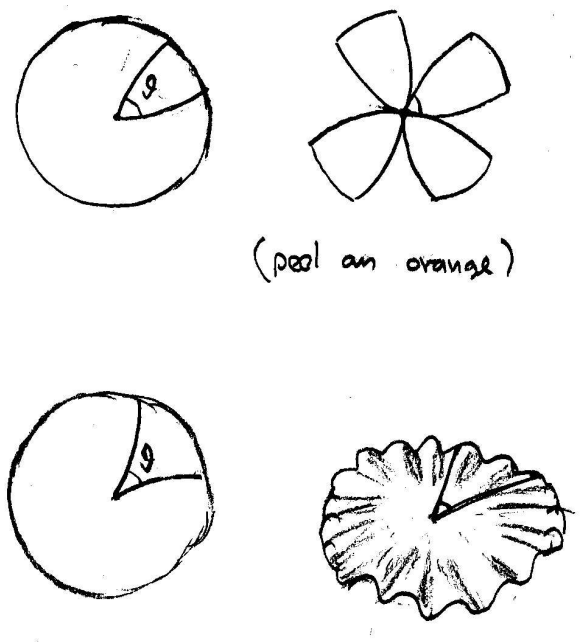

Figure 18: The geometry effect in a closed (top) or an open (bottom) universe affects the angle at which we see a structure of given size at the last scattering surface, and thus its angular diameter distance.

distance the photons have time to travel. When a larger part of this time is spent at small values of the scale factor, this distance gets a bigger boost from converting it to a comoving distance. For open/closed universes the angular diameter distance gets an additional effect from the geometry of the universe (the f_K), which acts like a "lens" to make the distant CMB pattern at the last scattering sphere to look smaller or larger (see Fig. 18).

9.4.2 Hubble scale and the matter-radiation equality scale

Subhorizon ($k \gg \mathcal{H}$) and superhorizon ($k \ll \mathcal{H}$) scales behave differently. Thus we want to know which of the structures we see on the last scattering surface are subhorizon and which are superhorizon. For that we need to know the comoving Hubble scale $\mathcal{H}$ at $t_{\rm dec}$. This was discussed in Sec. 8.3.1. At that time both matter and radiation are contributing to the energy density and the Hubble parameter. The scale which is just entering at $t = t_{\rm dec}$ is

$$\begin{aligned} k_{\rm dec}^{-1} &\equiv \mathcal{H}_{\rm dec}^{-1} = (1+z_{\rm dec})H_{\rm dec}^{-1} = (1+z_{\rm dec})^{-1/2} H_0^{-1}\Omega_m^{-1/2}\left[1+\frac{\Omega_r}{\Omega_m}(1+z_{\rm dec})\right]^{-1/2} \\ &= \Omega_m^{-1/2}(1+0.046\,\omega_m^{-1})^{-1/2}\,91\,h^{-1}{\rm Mpc} \end{aligned} \tag{43}$$

(using $z_{\rm dec} = 1090$; here $0.046\,\omega_m^{-1}$ is ρ_r/ρ_m at $t_{\rm dec}$) and the corresponding multipole number on the last scattering sphere is

$$\begin{aligned} \ell_H &\equiv k_{\rm dec} d_A^c \\ &= (1+z_{\rm dec})^{1/2}\Omega_m^{-1/2}\left[1+\frac{\Omega_r}{\Omega_m}(1+z_{\rm dec})\right]^{1/2} \times \begin{cases} 2/\Omega_m &= 66\,\Omega_m^{-0.5}\sqrt{1+0.046\omega_m^{-1}} \quad (\Omega_\Lambda = 0) \\ 2/\Omega_m^{0.4} &\approx 66\,\Omega_m^{0.1}\sqrt{1+0.046\omega_m^{-1}} \quad (\Omega_0 = 1) \end{cases} \end{aligned} \tag{44}$$

The angle subtended by a half-wavelength π/k of this mode on the last scattering sphere is

$$\vartheta_H \equiv \frac{\pi}{\ell_H} = \frac{180^\circ}{\ell_H} = \sqrt{1+0.046\,\omega_m^{-1}} \times \begin{cases} 2.7^\circ\Omega_m^{0.5} \\ 2.7^\circ\Omega_m^{-0.1} \end{cases} \tag{45}$$

For $\Omega_m \sim 0.3$, $\Omega_\Lambda \sim 0.7$, $h \sim 0.7$, $\ell_H \approx 67$ and $\vartheta_H \approx 3.5^\circ$ (the angle subtended by k^{-1} is 1.12°).

Another important scale is $k_{\rm eq}$, the scale which enters at the time of matter-radiation equality $t_{\rm eq}$, since the transfer function $T(k)$ is bent at that point. Perturbations for scales $k \ll k_{\rm eq}$ maintain essentially their primordial spectrum, whereas scales $k \gg k_{\rm eq}$ have lost relative power between their horizon entry and $t_{\rm eq}$. This scale is

$$k_{\rm eq}^{-1} \;=\; \mathcal{H}_{\rm eq}^{-1} \sim 13.7\,\Omega_m^{-1} h^{-2}\,{\rm Mpc} \;=\; 4.6\times 10^{-3}\,\Omega_m^{-1} h^{-1} H_0^{-1} \tag{46}$$

and the corresponding multipole number of these scales seen on the last scattering sphere is

$$l_{\rm eq} \;=\; k_{\rm eq} d_A^c \;=\; 219\,\Omega_m h \times \left\{ \begin{array}{lll} 2/\Omega_m & = & 440\,h \qquad (\Omega_\Lambda = 0) \\ 2/\Omega_m^{0.4} & \approx & 440\,h\;\Omega_m^{0.6} \qquad (\Omega_0 = 1) \end{array} \right. \tag{47}$$

Later we will introduce the *sound horizon* at photon decoupling, another important scale.

9.5 CMB anisotropy from perturbation theory

We began this chapter with the observation, Eq. (1), that the CMB temperature anisotropy is a sum of two parts,

$$\left(\frac{\delta T}{T}\right)_{\rm obs} = \left(\frac{\delta T}{T}\right)_{\rm intr} + \left(\frac{\delta T}{T}\right)_{\rm jour} , \tag{48}$$

and that this separation is gauge dependent. We shall consider this in the conformal-Newtonian gauge, since the second part, $\left(\frac{\delta T}{T}\right)_{\rm jour}$, the integrated redshift perturbation along the line of sight, is easiest to calculate in this gauge. (However, we won't do the calculation here.[5])

The result of this calculation is

$$\begin{aligned}
\left(\frac{\delta T}{T}\right)_{\rm jour} &= -\int d\Phi + \int (\dot\Phi + \dot\Psi) dt + \mathbf{v}_{\rm obs}\cdot\hat{\mathbf{n}} \\
&= \Phi(t_{\rm dec}, \mathbf{x}_{\rm ls}) - \Phi(t_0, \mathbf{0}) + \int (\dot\Phi + \dot\Psi) dt + \mathbf{v}_{\rm obs}\cdot\hat{\mathbf{n}} \\
&\overset{\Psi\approx\Phi}{\approx} \Phi(t_{\rm dec}, \mathbf{x}_{\rm ls}) - \Phi(t_0, \mathbf{0}) + 2\int \dot\Phi dt + \mathbf{v}_{\rm obs}\cdot\hat{\mathbf{n}}
\end{aligned} \tag{49}$$

where the integral is from $(t_{\rm dec}, \mathbf{x}_{\rm ls})$ to $(t_0, \mathbf{0})$ along the path of the photon (a null geodesic), and $\dot{} \equiv \partial/\partial t$. The origin $\mathbf{0}$ is located where the observer is. The last term, $\mathbf{v}_{\rm obs}\cdot\hat{\mathbf{n}}$, is the Doppler effect from observer motion (assumed nonrelativistic), $\mathbf{v}_{\rm obs}$ being the observer velocity and $\hat{\mathbf{n}}$ the direction we are looking at. The ${}_{\rm ls}$ in $\mathbf{x}_{\rm ls}$ is just to remind us that $\mathbf{x}$ lies somewhere on the last scattering sphere. In the matter-dominated universe the Newtonian potential remains constant in time, $\dot\Phi = 0$, so we get a contribution from the integral only from epochs when radiation or dark energy contributions to the total energy density, or the effect of curvature, cannot be ignored. We can understand the above result as follows. If the potential is constant in time, the blueshift the photon acquires when falling into a potential well is canceled by the redshift from climbing up the well. Thus the net redshift/blueshift caused by gravitational potential perturbations is just the difference between the values of Φ at the beginning and in the end. However, if the potential is changing while the photon is traversing the well, this cancelation is not exact, and we get the integral term to account for this effect.

The value of the potential perturbation at the observing site, $\Phi(t_0, \mathbf{0})$ is the same for photons coming from all directions. Thus it does not contribute to the observed anisotropy. It just produces an overall shift in the observed average temperature. This is included in the observed value $T_0 = 2.7255 \pm 0.0006\,{\rm K}$, and so we just ignore this term, not attempting to separate it from the "correct" unperturbed value.[6] The observer motion $\mathbf{v}_{\rm obs}$ causes a dipole ($\ell = 1$) pattern

[5] It is done in my course on Cosmological Perturbation Theory, Sec. 25.

[6] I don't think the local value of the gravitational potential, $\Phi(t_0, \mathbf{0})$ is known very well. In a quick search I couldn't locate literature discussing it. We live within an overdensity (Solar System + Galaxy + Local Group + Local Supercluster) and thus in a potential well, so $\Phi(t_0, \mathbf{0})$ is negative, contributing a blueshift, and the true unperturbed value of T_0 is slightly lower than 2.7255 K. The exact calculation of ω_γ from T_0 would require the use of this corrected value. While I don't have a good number it appears likely that the correction $\Phi(t_0, \mathbf{0})$ to T_0 is smaller than the uncertainty in the T_0 measurement. The order of magnitude of the Galactic contribution (which is much larger than the Solar contribution) is $\Phi \sim v^2$, where $v = 240\,{\rm km/s} = 8\times10^{-4}$ [4] is the local rotation velocity of the Galaxy. (For a spherically symmetric mass distribution, $\Phi = -v^2$, where v is the circular orbit velocity, is exact outside the mass distribution; if there is mass outside the orbit, it does not contribute to the gravitational field, but it does contribute to the potential. Most of the mass of the Galaxy is further away from the center than the Solar System, and therefore the Galactic contribution to the local potential $\Phi(t_0, \mathbf{0})$ is larger than $-v^2 = -6.4\times10^{-7}$.) The large scale contribution could be estimated by cosmic flow velocities using linear perturbation theory, where velocity is related to the potential gradient; for the matter-dominated growing solution, $\mathbf{v} = -\frac{2}{3}\mathcal{H}^{-1}\nabla\Phi$. The motion of the Local Group in the CMB rest frame has $v = 620\,{\rm km/s} = 2.07\times10^{-3}$ [4], but we would need the relevant scale over which Φ varies to get an estimate of Φ from this. Anyway, this scale is much smaller than the Hubble scale, so the order of magnitude estimate of the linear contribution to $\Phi(t_0, \mathbf{0})$ is much less than this v.

in the CMB anisotropy, and likewise, we do not attempt to separate from it the cosmological dipole on the last scattering sphere. Therefore the dipole is usually removed from the CMB map before analyzing it for cosmological purposes. Accordingly, we shall ignore this term also, and our final result is

$$\left(\frac{\delta T}{T}\right)_{\rm jour} = \Phi(t_{\rm dec}, \mathbf{x}_{\rm ls}) + 2\int \dot{\Phi} dt\,. \tag{50}$$

The other part, $\left(\frac{\delta T}{T}\right)_{\rm intr}$, comes from the local temperature perturbation at $t = t_{\rm dec}$ and the Doppler effect, $-\mathbf{v}\cdot\hat{\mathbf{n}}$, from the local (baryon+photon) fluid motion at that time. Since

$$\rho_\gamma = \frac{\pi^2}{15} T^4\,, \tag{51}$$

the local temperature perturbation is directly related to the relative perturbation in the photon energy density, and

$$\left(\frac{\delta T}{T}\right)_{\rm intr} = \frac{1}{4}\delta_\gamma - \mathbf{v}\cdot\hat{\mathbf{n}}\,. \tag{52}$$

We can now write the observed temperature anisotropy as

$$\boxed{\left(\frac{\delta T}{T}\right)_{\rm obs} = \frac{1}{4}\delta_\gamma^N - \mathbf{v}^N\cdot\hat{\mathbf{n}} + \Phi(t_{\rm dec}, \mathbf{x}_{\rm ls}) + 2\int \dot{\Phi} dt\,.} \tag{53}$$

(note that both the density perturbation δ_γ and the fluid velocity $\mathbf{v}$ are gauge dependent).

To make further progress we now

1. consider adiabatic primordial perturbations only (like we did in Chapter 8), and
2. make the (crude) approximation that the universe is already matter dominated at $t = t_{\rm dec}$.

For adiabatic perturbations

$$\delta_b = \delta_c \equiv \delta_m = \frac{3}{4}\delta_\gamma\,. \tag{54}$$

The perturbations stay adiabatic only at superhorizon scales. Once the perturbation has entered horizon, different physics begins to act on different matter components, so that the adiabatic relation between their density perturbations is broken. In particular, the baryon+photon perturbation is affected by photon pressure, which will damp their growth and cause them to oscillate, whereas the CDM perturbation is unaffected and keeps growing. Since the baryon and photon components see the same pressure they still evolve together and maintain their adiabatic relation until photon decoupling. Thus, after horizon entry, but before decoupling,

$$\delta_c \neq \delta_b = \frac{3}{4}\delta_\gamma\,. \tag{55}$$

At decoupling, the equality holds for scales larger than the photon mean free path at $t_{\rm dec}$.

After decoupling, this connection between the photons and baryons is broken, and the baryon density perturbation begins to approach the CDM density perturbation,

$$\delta_c \leftarrow \delta_b \neq \frac{3}{4}\delta_\gamma\,. \tag{56}$$

We shall return to these issues as we discuss the shorter scales in Sections 9.7 and 9.8. But let us first discuss the scales which are still superhorizon at $t_{\rm dec}$, so that Eq. (54) still applies.

9.6 Large scales: Sachs–Wolfe part of the spectrum

Consider now the scales $k \ll k_{\rm dec}$, or $\ell \ll \ell_H$, which are still superhorizon at decoupling. We can now use the adiabatic condition (54), so that

$$\frac{1}{4}\delta_\gamma = \frac{1}{3}\delta_m \approx \frac{1}{3}\delta\,, \tag{57}$$

where the latter (approximate) equality comes from taking the universe to be matter dominated at $t_{\rm dec}$, so that we can identify $\delta \approx \delta_m$. For these scales the Doppler effect from fluid motion is subdominant, and we can ignore it (the fluid is set into motion by gradients in the pressure and gravitational potential, but the time scale of getting into motion is longer than the Hubble time for superhorizon scale gradients).

Thus Eq. (53) becomes

$$\left(\frac{\delta T}{T}\right)_{\rm obs} = \frac{1}{3}\delta^N + \Phi(t_{\rm dec}, \mathbf{x}_{\rm ls}) + 2\int \dot{\Phi} dt\,. \tag{58}$$

The Newtonian relation

$$\delta = \frac{1}{4\pi G\bar{\rho}a^2}\nabla^2\Phi = \frac{2}{3}\left(\frac{1}{aH}\right)^2\nabla^2\Phi$$

(here ∇ is with respect to the comoving coordinates, hence the a^{-2}) or

$$\delta_{\mathbf{k}} = -\frac{2}{3}\left(\frac{k}{\mathcal{H}}\right)^2\Phi_{\mathbf{k}}$$

does not hold at superhorizon scales (where δ is gauge dependent). A GR calculation using the Newtonian gauge gives the result[7]

$$\boxed{\delta^N_{\mathbf{k}} = -\left[2 + \frac{2}{3}\left(\frac{k}{\mathcal{H}}\right)^2\right]\Phi_{\mathbf{k}}} \tag{59}$$

for perturbations in a matter-dominated universe. Thus for superhorizon scales we can approximate

$$\delta^N \approx -2\Phi \tag{60}$$

and Eq. (58) becomes

$$\begin{aligned}\left(\frac{\delta T}{T}\right)_{\rm obs} &= -\frac{2}{3}\Phi(t_{\rm dec}, \mathbf{x}_{\rm ls}) + \Phi(t_{\rm dec}, \mathbf{x}_{\rm ls}) + 2\int \dot{\Phi} dt \\ &= \frac{1}{3}\Phi(t_{\rm dec}, \mathbf{x}_{\rm ls}) + 2\int \dot{\Phi} dt\,.\end{aligned} \tag{61}$$

This explains the "mysterious" factor 1/3 in this relation between the potential Φ and the temperature perturbation.

This result is called the *Sachs–Wolfe effect*. The first part, $\frac{1}{3}\Phi(t_{\rm dec}, \mathbf{x}_{\rm ls})$, is called the *ordinary* Sachs–Wolfe effect, and the second part, $2\int \dot{\Phi} dt$, the *integrated Sachs-Wolfe effect* (ISW), since it involves integrating along the line of sight. Note that the approximation of matter domination at $t = t_{\rm dec}$, making $\dot{\Phi} = 0$, does not eliminate the ISW, since it only applies to the "early part" of the integral. At times closer to t_0, dark energy becomes important, causing Φ to evolve again.

[7] Cosmological Perturbation Theory, Sec. 13.

This ISW caused by dark energy (or curvature of the background universe, if $k \neq 0$) is called the *late Sachs–Wolfe effect* (LSW) and it shows up as a rise in the smallest ℓ of the angular power spectrum C_ℓ. Correspondingly, the contribution to the ISW from the evolution of Φ near $t_{\rm dec}$ due to the radiation contribution to the expansion law (which we ignored in our approximation) is called the *early Sachs–Wolfe effect* (ESW). The ESW shows up as a rise in C_ℓ for larger ℓ, near ℓ_H.

We shall now forget for a while the ISW, which for $\ell \ll \ell_H$ is expected to be smaller than the ordinary Sachs–Wolfe effect.

9.6.1 Angular power spectrum from the ordinary Sachs–Wolfe effect

We now calculate the contribution from the ordinary Sachs–Wolfe effect,

$$\boxed{\left(\frac{\delta T}{T}\right)_{\rm SW} = \frac{1}{3}\Phi(t_{\rm dec}, \mathbf{x}_{\rm ls})\,,} \tag{62}$$

to the angular power spectrum C_ℓ. This is the dominant effect for $\ell \ll \ell_H$.

Since Φ is evaluated at the last scattering sphere, we have, from Eq. (30),

$$a_{\ell m} = 4\pi i^\ell \sum_{\mathbf{k}} \frac{1}{3}\Phi_{\mathbf{k}} j_\ell(kx) Y^*_{\ell m}(\hat{\mathbf{k}})\,, \tag{63}$$

In the matter-dominated epoch,

$$\Phi = -\frac{3}{5}\mathcal{R}\,, \tag{64}$$

so that

$$a_{\ell m} = -\frac{4\pi}{5} i^\ell \sum_{\mathbf{k}} \mathcal{R}_{\mathbf{k}} j_\ell(kx) Y^*_{\ell m}(\hat{\mathbf{k}})\,. \tag{65}$$

The coefficient $a_{\ell m}$ is thus a linear combination of the independent random variables $\mathcal{R}_{\mathbf{k}}$, i.e., it is of the form

$$\sum_{\mathbf{k}} b_{\mathbf{k}} \mathcal{R}_{\mathbf{k}}\,, \tag{66}$$

For any such linear combination, the expectation value of its absolute value squared is

$$\begin{aligned}\left\langle \left| \sum_{\mathbf{k}} b_{\mathbf{k}} \mathcal{R}_{\mathbf{k}} \right|^2 \right\rangle &= \sum_{\mathbf{k}} \sum_{\mathbf{k}'} b_{\mathbf{k}} b^*_{\mathbf{k}'} \langle \mathcal{R}_{\mathbf{k}} \mathcal{R}^*_{\mathbf{k}'} \rangle \\ &= \left(\frac{2\pi}{L}\right)^3 \sum_{\mathbf{k}} \frac{1}{4\pi k^3} \mathcal{P}_{\mathcal{R}}(k) \left| b_{\mathbf{k}} \right|^2\,, \end{aligned} \tag{67}$$

where we used

$$\langle \mathcal{R}_{\mathbf{k}} \mathcal{R}^*_{\mathbf{k}'} \rangle = \delta_{\mathbf{k}\mathbf{k}'} \left(\frac{2\pi}{L}\right)^3 \frac{1}{4\pi k^3} \mathcal{P}_{\mathcal{R}}(k) \tag{68}$$

(the independence of the random variables $\mathcal{R}_{\mathbf{k}}$ and the definition of the power spectrum $\mathcal{P}(k)$).

Thus

$$\begin{aligned} C_\ell &\equiv \frac{1}{2\ell+1} \sum_m \langle |a_{\ell m}|^2 \rangle \\ &= \frac{16\pi^2}{25} \frac{1}{2\ell+1} \sum_m \left(\frac{2\pi}{L}\right)^3 \sum_{\mathbf{k}} \frac{1}{4\pi k^3} \mathcal{P}_{\mathcal{R}}(k) j_\ell(kx)^2 \left| Y^*_{\ell m}(\hat{\mathbf{k}}) \right|^2 \\ &= \frac{1}{25} \left(\frac{2\pi}{L}\right)^3 \sum_{\mathbf{k}} \frac{1}{k^3} \mathcal{P}_{\mathcal{R}}(k) j_\ell(kx)^2\,. \end{aligned} \tag{69}$$

(Although all $\langle |a_{\ell m}|^2 \rangle$ are equal for the same ℓ, we used the sum over m, so that we could use Eq. (9).) Replacing the sum with an integral, we get

$$\begin{aligned} C_\ell &= \frac{1}{25} \int \frac{d^3k}{k^3} \mathcal{P}_\mathcal{R}(k) j_\ell(kx)^2 \\ &= \frac{4\pi}{25} \int_0^\infty \frac{dk}{k} \mathcal{P}_\mathcal{R}(k) j_\ell(kx)^2 \,, \end{aligned} \tag{70}$$

where $x = d_A^c(z_{\rm dec})$, the final result for an arbitrary primordial power spectrum $\mathcal{P}_\mathcal{R}(k)$.

The integral can be done for a power-law power spectrum, $\mathcal{P}_\mathcal{R}(k) = A_s^2 (k/k_p)^{n-1}$. In particular, for a scale-invariant ($n = 1$) primordial power spectrum,

$$\mathcal{P}_\mathcal{R}(k) = \text{const.} = A_s^2 \,, \tag{71}$$

we have

$$C_\ell = A_s^2 \frac{4\pi}{25} \int_0^\infty \frac{dk}{k} j_\ell(kx)^2 = \frac{A_s^2}{25} \frac{2\pi}{\ell(\ell+1)} \,, \tag{72}$$

since

$$\int_0^\infty \frac{dk}{k} j_\ell(kx)^2 = \frac{1}{2\ell(\ell+1)} \,. \tag{73}$$

We can write this as

$$\frac{\ell(\ell+1)}{2\pi} C_\ell = \frac{A_s^2}{25} = \text{const. (independent of } \ell) \tag{74}$$

This is the reason why the angular power spectrum is customarily plotted as $\ell(\ell+1)C_\ell/2\pi$; it makes the ordinary Sachs–Wolfe part of the C_ℓ flat for a scale-invariant primordial power spectrum $\mathcal{P}_\mathcal{R}(k)$.

Observations are consistent with an almost scale-invariant primordial power spectrum (they favor a small red tilt, $n < 1$). The constant A_s can be determined from the ordinary Sachs–Wolfe part of the observed $\widehat{C}_\ell$. From Fig. 11 we see that at low ℓ

$$\frac{\ell(\ell+1)}{2\pi} \widehat{C}_\ell \sim \frac{800\,\mu\text{K}^2}{(2.725\,K)^2} \sim 10^{-10} \tag{75}$$

on the average. This gives the amplitude of the primordial power spectrum as

$$\mathcal{P}_\mathcal{R}(k) = A_s^2 \sim 25 \times 10^{-10} = \left(5 \times 10^{-5}\right)^2 \,. \tag{76}$$

We already used this result in Chapter 8 as a constraint on the energy scale of inflation.

Exercise: Find the C_ℓ of the ordinary Sachs-Wolfe effect due to a power-law power spectrum $\mathcal{P}_\mathcal{R}(k) = A_s^2 (k/k_p)^{n-1}$. Help:

$$\int_0^\infty dx\, x^{n-2} j_\ell^2(x) = 2^{n-4} \pi \frac{\Gamma(\ell + \frac{n}{2} - \frac{1}{2}) \Gamma(3-n)}{\Gamma(\ell + \frac{5}{2} - \frac{n}{2}) \Gamma(2 - \frac{n}{2})^2} \,. \tag{77}$$

Take $A_s = 4.58 \times 10^{-5}$, for a pivot scale $k_p = 0.05\,\text{Mpc}^{-1}$, and $n = 0.965$ (Planck 2018 central values). Give the numerical values for C_2 and C_{20}. Use $d_A^c(z_{\rm dec}) = 2\Omega_m^{-0.4} H_0^{-1}$, with $\Omega_m = 0.315$ and $H_0 = 67.36\,\text{km/s/Mpc}$ (Planck 2018 central values). Give also $\mathcal{D}_2$ and $\mathcal{D}_{20}$, where $\mathcal{D}_\ell \equiv T_0^2 [\ell(\ell+1)/(2\pi)] C_\ell$, and compare to Fig. 11. What explains the difference?

9.7 Acoustic oscillations

Consider now the scales $k \gg k_{\rm dec}$, or $\ell \gg \ell_H$, which are subhorizon at decoupling. The observed temperature anisotropy is, from Eq. (53)

$$\left(\frac{\delta T}{T}\right)_{\rm obs} = \frac{1}{4}\delta_\gamma(t_{\rm dec}, \mathbf{x}_{\rm ls}) + \Phi(t_{\rm dec}, \mathbf{x}_{\rm ls}) - \mathbf{v}_\gamma \cdot \hat{\mathbf{n}}(t_{\rm dec}, \mathbf{x}_{\rm ls}) + 2\int \dot{\Phi} dt\,. \tag{78}$$

Since we are considering subhorizon scales, we dropped the reference to the Newtonian gauge. We shall concentrate on the three first terms, which correspond to the situation at the point $(t_{\rm dec}, \mathbf{x}_{\rm ls})$ we are looking at on the last scattering sphere.

Before decoupling photons are coupled to baryons. Perturbations in the baryon-photon fluid are oscillating, whereas CDM perturbations grow (slowly during the radiation-dominated epoch, and then faster during the matter-dominated epoch). Therefore CDM perturbations begin to dominate the total density perturbation $\delta\rho$ and thus also Φ already before the universe becomes matter dominated and CDM begins to dominate the background energy density. Thus we make the approximation that Φ is given by the CDM perturbation. The baryon-photon fluid oscillates in these potential wells caused by the CDM. The potential Φ evolves at first but then becomes constant as the universe becomes matter dominated.

We shall not attempt an exact calculation of the $\delta_{b\gamma}$ oscillations in the expanding universe. One reason is that $\rho_{b\gamma}$ is a relativistic fluid, and we have derived the perturbation equations for a nonrelativistic fluid only. From Sec. 8.2.7 we have that the nonrelativistic perturbation equation for a fluid component i is

$$\ddot{\delta}_{\mathbf{k}i} + 2H\dot{\delta}_{\mathbf{k}i} = -\frac{k^2}{a^2}\left(\frac{\delta p_{\mathbf{k}i}}{\bar{\rho}_i} + \Phi_{\mathbf{k}}\right). \tag{79}$$

The generalization of the (subhorizon) perturbation equations to the case of a relativistic fluid is considerably easier if we ignore the expansion of the universe. Then Eq. (79) becomes

$$\ddot{\delta}_{\mathbf{k}i} + k^2\left(\frac{\delta p_{\mathbf{k}i}}{\bar{\rho}_i} + \Phi_{\mathbf{k}}\right) = 0\,. \tag{80}$$

According to GR, the density of "passive gravitational mass" is $\rho + p = (1+w)\rho$, not just ρ as in Newtonian gravity. Therefore the force on a fluid element of the fluid component i is proportional to $(\rho_i + p_i)\nabla\Phi = (1+w_i)\rho_i\nabla\Phi$ instead of just $\rho_i\nabla\Phi$, and Eq. (80) generalizes to the case of a relativistic fluid as[8]

$$\ddot{\delta}_{\mathbf{k}i} + k^2\left[\frac{\delta p_{\mathbf{k}i}}{\bar{\rho}_i} + (1+w_i)\Phi_{\mathbf{k}}\right] = 0\,. \tag{81}$$

In the present application the fluid component ρ_i is the baryon-photon fluid $\rho_{b\gamma}$ and the gravitational potential Φ is caused by the CDM. Before decoupling, the adiabatic relation $\delta_b = \frac{3}{4}\delta_\gamma$ still holds between photons and baryons, and we have the adiabatic relation between pressure and density perturbations,

$$\delta p_{b\gamma} = c_s^2 \delta\rho_{b\gamma}\,. \tag{82}$$

Thus we have

$$\ddot{\delta}_{b\gamma\mathbf{k}} + k^2\left[c_s^2\delta_{b\gamma\mathbf{k}} + (1+w_{b\gamma})\Phi_{\mathbf{k}}\right] = 0\,. \tag{83}$$

Here

$$c_s^2 = \frac{\delta p_{b\gamma}}{\delta\rho_{b\gamma}} \approx \frac{\delta p_\gamma}{\delta\rho_{b\gamma}} = \frac{1}{3}\frac{\delta\rho_\gamma}{\delta\rho_\gamma + \delta\rho_b} = \frac{1}{3}\frac{\bar{\rho}_\gamma\delta_\gamma}{\bar{\rho}_\gamma\delta_\gamma + \bar{\rho}_b\delta_b} = \frac{1}{3}\frac{1}{1+\frac{3}{4}\frac{\bar{\rho}_b}{\bar{\rho}_\gamma}} \equiv \frac{1}{3}\frac{1}{1+R} \tag{84}$$

[8] Actually the derivation is more complicated, since also the density of "inertial mass" is $\rho_i + p_i$ and the energy continuity equation is modified by a work-done-by-pressure term. The more detailed derivation of Eq. (81) was given in Sec. 8.2.8.

gives the speed of sound c_s of the baryon-photon fluid. We defined

$$R \equiv \frac{3}{4}\frac{\bar{\rho}_b}{\bar{\rho}_\gamma}\,. \tag{85}$$

The equation-of-state parameter for the baryon-photon fluid is

$$w_{b\gamma} \equiv \frac{\bar{p}_{b\gamma}}{\bar{\rho}_{b\gamma}} = \frac{\frac{1}{3}\bar{\rho}_\gamma}{\bar{\rho}_\gamma + \bar{\rho}_b} = \frac{1}{3}\frac{1}{1+\frac{4}{3}R}\,, \tag{86}$$

so that

$$1 + w_{b\gamma} = \frac{\frac{4}{3}(1+R)}{1+\frac{4}{3}R} \tag{87}$$

and we can write Eq. (83) as

$$\ddot{\delta}_{b\gamma\mathbf{k}} + k^2\left[\frac{1}{3}\frac{1}{1+R}\delta_{b\gamma\mathbf{k}} + \frac{\frac{4}{3}(1+R)}{1+\frac{4}{3}R}\Phi_\mathbf{k}\right] = 0\,. \tag{88}$$

For the CMB anisotropy we are interested in[9]

$$\Theta_0 \equiv \frac{1}{4}\delta_\gamma\,, \tag{89}$$

which gives the local temperature perturbation, not in $\delta_{b\gamma}$. These two are related by

$$\delta_{b\gamma} = \frac{\delta\rho_{b\gamma}}{\bar{\rho}_{b\gamma}} = \frac{\delta\rho_\gamma + \delta\rho_b}{\bar{\rho}_\gamma + \bar{\rho}_b} = \frac{\bar{\rho}_\gamma\delta_\gamma + \bar{\rho}_b\delta_b}{\bar{\rho}_\gamma + \bar{\rho}_b} = \frac{1+R}{1+\frac{4}{3}R}\delta_\gamma\,. \tag{90}$$

Thus we can write Eq. (83) as

$$\ddot{\delta}_{\gamma\mathbf{k}} + k^2\left[\frac{1}{3}\frac{1}{1+R}\delta_{\gamma\mathbf{k}} + \frac{4}{3}\Phi_\mathbf{k}\right] = 0\,, \tag{91}$$

or

$$\ddot{\Theta}_{0\mathbf{k}} + k^2\left[\frac{1}{3}\frac{1}{1+R}\Theta_{0\mathbf{k}} + \frac{1}{3}\Phi_\mathbf{k}\right] = 0\,, \tag{92}$$

or

$$\ddot{\Theta}_{0\mathbf{k}} + c_s^2k^2\left[\Theta_{0\mathbf{k}} + (1+R)\Phi_\mathbf{k}\right] = 0\,, \tag{93}$$

If we now take R and Φ_k to be constant, this is the harmonic oscillator equation for the quantity $\Theta_{0\mathbf{k}} + (1+R)\Phi_\mathbf{k}$ with the general solution

$$\Theta_{0\mathbf{k}} + (1+R)\Phi_\mathbf{k} = A_\mathbf{k}\cos c_skt + B_\mathbf{k}\sin c_skt\,, \tag{94}$$

or

$$\Theta_{0\mathbf{k}} + \Phi_\mathbf{k} = -R\Phi_\mathbf{k} + A_\mathbf{k}\cos c_skt + B_\mathbf{k}\sin c_skt\,, \tag{95}$$

or

$$\Theta_{0\mathbf{k}} = -(1+R)\Phi_\mathbf{k} + A_\mathbf{k}\cos c_skt + B_\mathbf{k}\sin c_skt\,. \tag{96}$$

We are interested in the quantity $\Theta_0 + \Phi = \frac{1}{4}\delta_\gamma + \Phi$, called the *effective temperature perturbation*, since this combination appears in Eq. (78). It is the local temperature perturbation minus the redshift photons suffer when climbing from the potential well of the perturbation (negative Φ

[9]The subscript 0 refers to the monopole ($\ell = 0$) of the *local* photon distribution. Likewise, the dipole ($\ell = 1$) of the local photon distribution corresponds to the velocity of the photon fluid, $\Theta_1 \equiv v_\gamma/3$.

for a CDM overdensity). We see that this quantity oscillates in time, and the *effect of baryons* (via R) is to *shift the equilibrium point* of the oscillation by $-R\Phi_{\mathbf{k}}$.

In the preceding we ignored the effect of the expansion of the universe. The expansion affects the preceding in a number of ways. For example, c_s, $w_{b\gamma}$ and R change with time. The potential Φ also evolves, especially at the earlier times when radiation dominates the expansion law. However, the qualitative result of an oscillation of $\Theta_0 + \Phi$, and the shift of its equilibrium point by baryons, remains. The time t in the solution (95) gets replaced by conformal time η, and since c_s changes with time, $c_s\eta$ is replaced by

$$r_s(t) \equiv \int_0^\eta c_s d\eta = \int_0^t \frac{c_s(t)}{a(t)} dt\,. \tag{97}$$

We call this quantity $r_s(t)$ the *sound horizon* at time t, since it represents the comoving distance sound has traveled by time t.

The relative weight of the cosine and sine solutions (i.e., the constants $A_{\mathbf{k}}$ and $B_{\mathbf{k}}$ in Eq. (94) depends on the initial conditions. Since the perturbations are initially at superhorizon scales, the initial conditions are determined there, and the present discussion does not really apply. However, using the Newtonian gauge superhorizon initial conditions gives the correct qualitative result for the phase of the oscillation.

We had that for adiabatic primordial perturbations, initially $\Phi = -\frac{3}{5}\mathcal{R}$ and $\frac{1}{4}\delta_\gamma^N = -\frac{2}{3}\Phi = \frac{2}{5}\mathcal{R}$, giving us an initial condition $\Theta_0 + \Phi = \frac{1}{3}\Phi = -\frac{1}{5}\mathcal{R} = \text{const.}$ (At these early times $R \ll 1$, so we don't write the $1 + R$.) Thus adiabatic primordial perturbations correspond essentially to the cosine solution.[10] (There are effects at the horizon scale which affect the amplitude of the oscillations—the main effect being the decay of Φ as it enters the horizon—so we can't use the preceding discussion to determine the amplitude, but we get the right result about the initial phase of the $\Theta_0 + \Phi$ oscillations.)

Thus we have that, qualitatively, the effective temperature behaves at subhorizon scales as

$$\Theta_{0\mathbf{k}} + (1+R)\Phi_{\mathbf{k}} \;\propto\; \cos kr_s(t)\,, \tag{98}$$

Consider a region which corresponds to a positive primordial curvature perturbation $\mathcal{R}$. It begins with an initial overdensity (of all components, photons, baryons, CDM and neutrinos), and a negative gravitational potential Φ. For the scales of interest for CMB anisotropy, the potential stays negative, since the CDM begins to dominate the potential early enough and the CDM perturbations do not oscillate, they just grow. The effective temperature perturbation $\Theta_0 + \Phi$, which is the oscillating quantity, begins with a negative value. After half an oscillation period it is at its positive extreme value. This increase of $\Theta_0 + \Phi$ corresponds to an increase in δ_γ; from its initial positive value it has grown to a larger positive value. Thus the oscillation begins by the, already initially overdense, baryon-photon fluid falling deeper into the potential well, and reaching its maximum compression after half a period. After this maximum compression the photon pressure pushes the baryon-photon fluid out from the potential well, and after a full period, the fluid reaches its maximum decompression in the potential well. Since the potential Φ has meanwhile decayed (horizon entry and the resulting potential decay always happens during the first oscillation period, since the sound horizon and the Hubble length are close to each other, as the sound speed is close to the speed of light), the decompression does not bring the $\delta_{b\gamma}$ back to its initial value (which was overdense), but the photon-baryon fluid actually becomes underdense in the potential well (and overdense in the neighboring potential "hill"). And so the oscillation goes on until photon decoupling.

These are standing waves and they are called *acoustic oscillations*. See Fig. 19. Because of the potential decay at horizon entry, the amplitude of the oscillation is larger than Φ, and thus also Θ_0 changes sign in the oscillation.

[10] The sine solution corresponds to what are called *isocurvature* primordial perturbations.

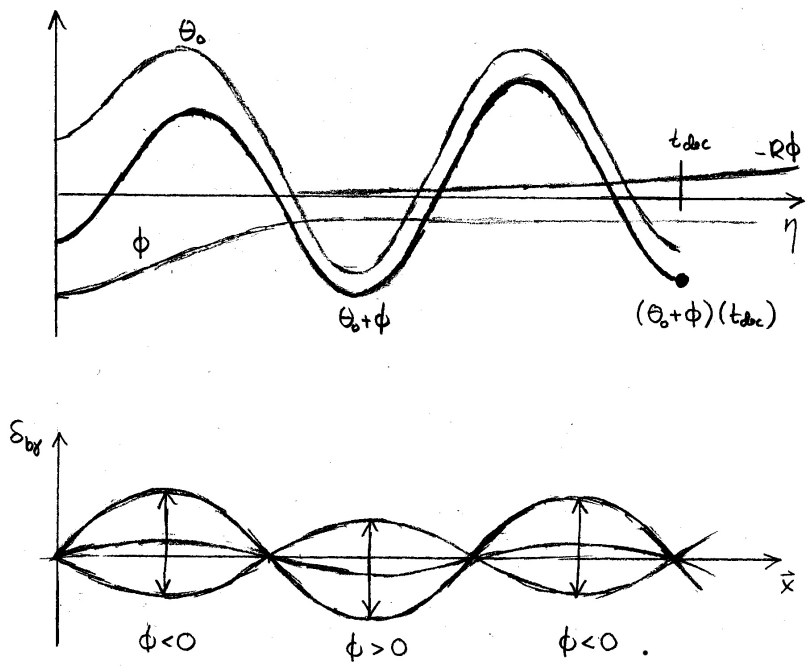

Figure 19: Acoustic oscillations. The top panel shows the time evolution of the Fourier amplitudes $\Theta_{0\mathbf{k}}$, $\Phi_{\mathbf{k}}$, and the effective temperature $\Theta_{0\mathbf{k}} + \Phi_{\mathbf{k}}$. The Fourier mode shown corresponds to the fourth acoustic peak of the C_ℓ spectrum. The bottom panel shows $\delta_{b\gamma}(\mathbf{x})$ for one Fourier mode as a function of position at various times (maximum compression, equilibrium level, and maximum decompression).

These oscillations end at photon decoupling, when the photons are liberated. The CMB shows these standing waves as a snapshot[11] at their final moment $t = t_{\rm dec}$.

At photon decoupling we have

$$\Theta_{0\mathbf{k}} + (1+R)\Phi_{\mathbf{k}} \propto \cos kr_s(t_{\rm dec})\,. \tag{99}$$

At this moment oscillations for scales k which have

$$kr_s(t_{\rm dec}) = m\pi \tag{100}$$

($m = 1, 2, 3, \ldots$) are at their extreme values (maximum compression or maximum decompression). Therefore we see strong structure in the CMB anisotropy at the multipoles

$$\ell = kd_A^c(t_{\rm dec}) = m\pi\frac{d_A^c(t_{\rm dec})}{r_s(t_{\rm dec})} \equiv m\ell_A \tag{101}$$

corresponding to these scales. Here

$$\ell_A \equiv \pi\frac{d_A^c(t_{\rm dec})}{r_s(t_{\rm dec})} \equiv \frac{\pi}{\vartheta_s} \tag{102}$$

is the *acoustic scale* in multipole space and

$$\vartheta_s \equiv \frac{r_s(t_{\rm dec})}{d_A^c(t_{\rm dec})} \tag{103}$$

[11] Actually, photon decoupling takes quite a long time. Therefore this "snapshot" has a rather long "exposure time" causing it to be "blurred". This prevents us from seeing very small scales in the CMB anisotropy.

is the *sound horizon angle*, i.e., the angle at which we see the sound horizon on the last scattering surface.

Because of these acoustic oscillations, the CMB angular power spectrum C_ℓ has a structure of *acoustic peaks* at subhorizon scales. The centers of these peaks are located approximately at $\ell_m \approx m\ell_A$. An exact calculation shows that they will actually lie at somewhat smaller ℓ due to a number of effects. The separation of neighboring peaks is closer to ℓ_A than the positions of the peaks are to $m\ell_A$.

These acoustic oscillations involve motion of the baryon-photon fluid. When the oscillation of one Fourier mode is at its extreme, e.g., at the maximal compression in the potential well, the fluid is momentarily at rest, but then it begins flowing out of the well until the other extreme, the maximal decompression, is reached. Therefore those Fourier modes $\mathbf{k}$ which have the maximum effect on the CMB anisotropy via the $\frac{1}{4}\delta_\gamma(t_{\rm dec}, \mathbf{x}_{\rm ls}) + \Phi(t_{\rm dec}, \mathbf{x}_{\rm ls})$ term (the effective temperature effect) in Eq. (78) have the minimum effect via the $-\mathbf{v}\cdot\hat{\mathbf{n}}(t_{\rm dec}, \mathbf{x}_{\rm ls})$ term (the Doppler effect) and vice versa. Therefore the Doppler effect also contributes a peak structure to the C_ℓ spectrum, but the peaks are in the locations where the effective temperature contribution has troughs.

The Doppler effect is subdominant to the effective temperature effect, and therefore the peak positions in the C_ℓ spectrum are determined by the effective temperature effect, according to Eq. (101). The Doppler effect just partially fills the troughs between the peaks, weakening the peak structure of C_ℓ. See Fig. 22.

Fig. 20 shows the values of the effective temperature perturbation $\Theta_0 + \Phi$ (as well as Θ_0 and Φ separately) and the magnitude of the velocity perturbation ($\Theta_1 \sim v/3$) at $t_{\rm dec}$ as a function of the scale k. This is a result of a numerical calculation which includes the effect of the expansion of the universe, but not diffusion damping (Sec. 9.8).

9.8 Diffusion damping

For small enough scales the effect of photon diffusion and the finite thickness of the last scattering surface ($\sim$ the photon mean free path just before last scattering) smooth out the photon distribution and the CMB anisotropy.

This effect can be characterized by the damping scale $k_D^{-1} \sim$ photon diffusion length $\sim$ geometric mean of the Hubble time and photon mean free path λ_γ. Actually λ_γ is increasing rapidly during recombination, so a calculation of the diffusion scale involves an integral over time which includes this effect.

A calculation, that we shall not do here,[12] gives that photon density and velocity perturbations at scale k are damped at $t_{\rm dec}$ by

$$e^{-k^2/k_D^2}\,, \tag{104}$$

where the diffusion scale is

$$k_D^{-1} \sim \frac{1}{\text{few}}\frac{1}{a}\sqrt{\frac{\lambda_\gamma(t_{\rm dec})}{H_{\rm dec}}}\,. \tag{105}$$

Accordingly, the C_ℓ spectrum is also damped as

$$e^{-\ell^2/\ell_D^2} \tag{106}$$

where

$$\ell_D \sim k_D d_A^c(t_{\rm dec})\,. \tag{107}$$

For typical values of cosmological parameters $\ell_D \sim 1500$. See Fig. 21 for a result of a numerical calculation with and without diffusion damping.

[12] See, e.g., Dodelson [9], Chapter 8.

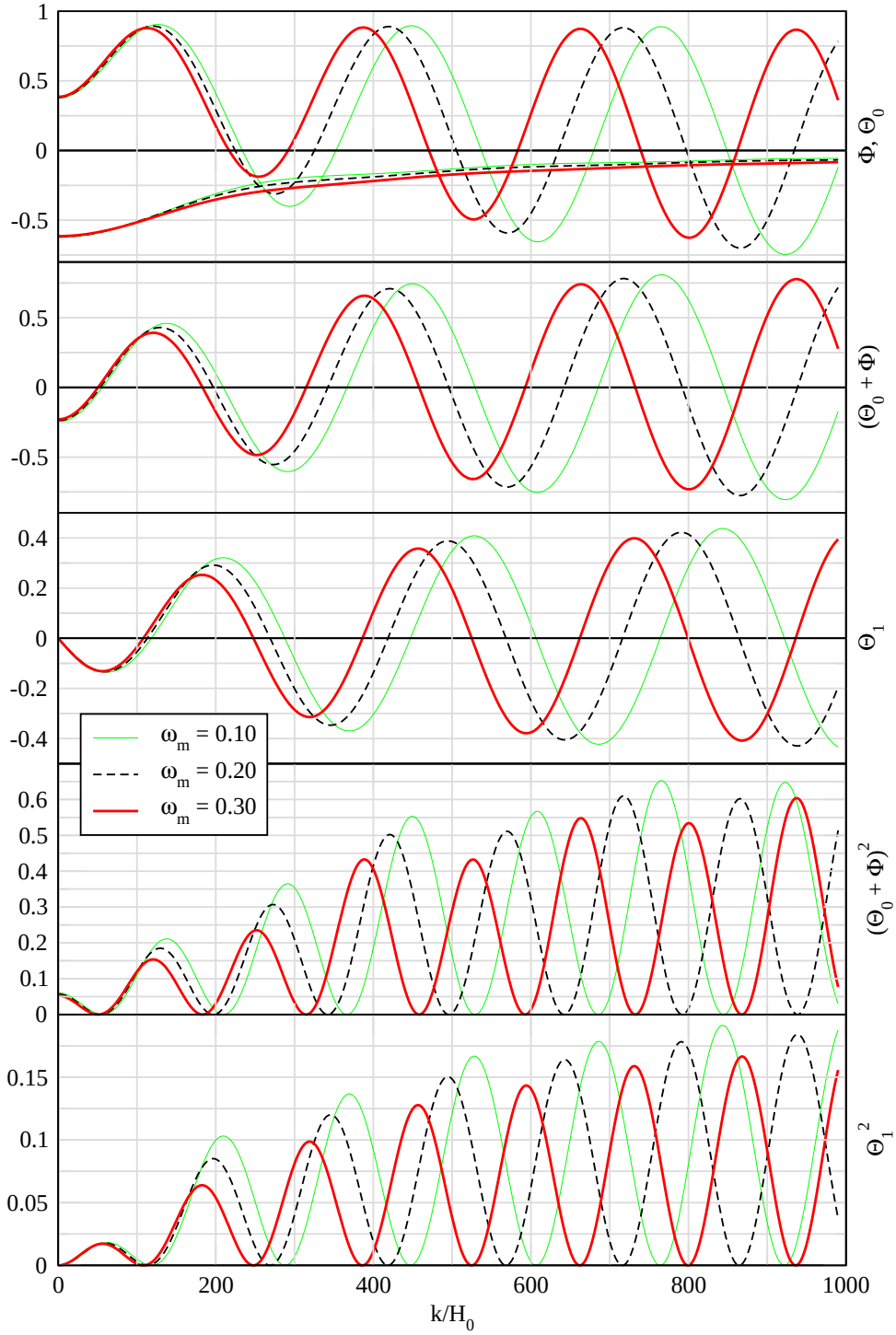

Figure 20: Values of oscillating quantities (normalized to an initial value $\mathcal{R}_{\mathbf{k}} = 1$) at the time of decoupling as a function of the scale k, for three different values of ω_m, and for $\omega_b = 0.01$. Θ_1 represents the velocity perturbation. The effect of diffusion damping is neglected. Figure and calculation by R. Keskitalo.

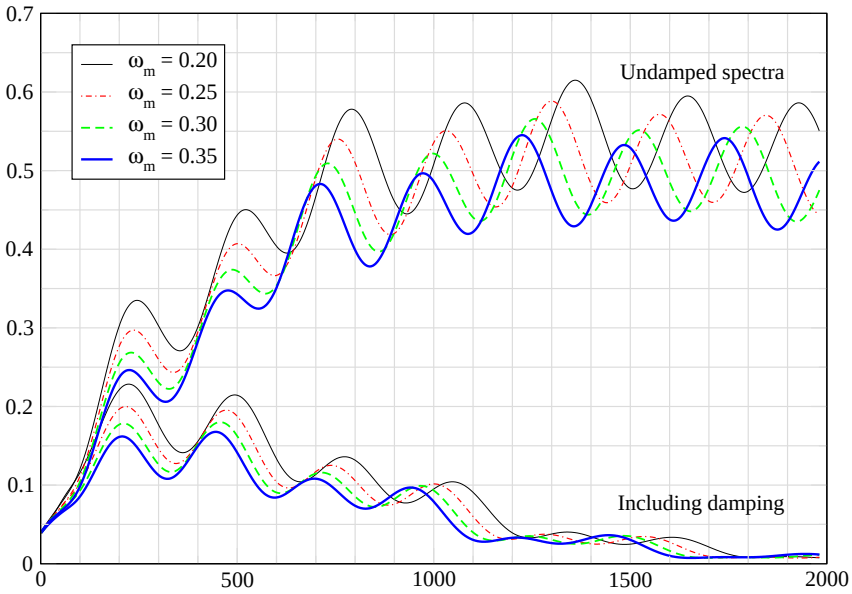

Figure 21: The angular power spectrum C_ℓ, calculated both with and without the effect of diffusion damping. The spectrum is given for four different values of ω_m, with $\omega_b = 0.01$. (This is a rather low value of ω_b, so $\ell_D < 1500$ and damping is quite strong.) Figure and calculation by R. Keskitalo.

Of the cosmological parameters, the damping scale is the most strongly dependent on ω_b, since increasing the baryon density shortens the photon mean free path before decoupling. Thus for larger ω_b the damping moves to shorter scales, i.e., ℓ_D becomes higher (there is less damping).

(Of course, decoupling only happens as the photon mean free path becomes comparable to the Hubble length, so one might think that λ_γ at $t_{\rm dec}$ should be independent of ω_b. However there is a distinction here between whether a photon will not scatter again after a particular scattering and what was the mean free path between the second-to-last and the last scattering. And k_D depends on an integral over the past history of the photon mean free path, not just the last one. The factor 1/few in Eq. (105) comes from that integration, and actually depends on ω_b. For small ω_b the λ_γ has already become quite large through the slow dilution of the baryon density by the expansion of the universe, and relies less on the fast reduction of free electron density due to recombination. Thus the time evolution of λ_γ before decoupling is different for different ω_b and we get a different diffusion scale.)

9.9 The complete C_ℓ spectrum

As we have discussed the CMB anisotropy has three contributions (see Eq. 78), the effective temperature effect,

$$\frac{1}{4}\delta_\gamma(t_{\rm dec}, \mathbf{x}_{\rm ls}) + \Phi(t_{\rm dec}, \mathbf{x}_{\rm ls})\,, \tag{108}$$

the Doppler effect,

$$-\mathbf{v}\cdot\hat{\mathbf{n}}(t_{\rm dec}, \mathbf{x}_{\rm ls})\,, \tag{109}$$

and the integrated Sachs–Wolfe effect,

$$2\int_{t_{\rm dec}}^{t_0} \dot{\Phi}(t, \mathbf{x}(t))dt\,. \tag{110}$$

Since the C_ℓ is a quadratic quantity, it also includes cross terms between these three effects.

The calculation of the full C_ℓ proceeds much as the calculation of just the ordinary Sachs–Wolfe part (which the effective temperature effect becomes at superhorizon scales) in Sec. 9.6.1, but now with the full $\delta T/T$. Since all perturbations are proportional to the primordial perturbations, the C_ℓ spectrum is proportional to the primordial perturbation spectrum $\mathcal{P}_\mathcal{R}(k)$ (with integrals over the spherical Bessel functions $j_\ell(kx)$, like in Eq. (70), to get from k to ℓ).

The difference is that instead of the constant proportionality factor $(\delta T/T)_{SW} = -(1/5)\mathcal{R}$, we have a k-dependent proportionality resulting from the evolution (including, e.g., the acoustic oscillations) of the perturbations.

In Fig. 22 we show the full C_ℓ spectrum and the different contributions to it.

Because the Doppler effect and the effective temperature effect are almost completely off-phase, their cross term gives a negligible contribution.

Since the ISW effect is relatively weak, it contributes more via its cross terms with the Doppler effect and effective temperature than directly. The cosmological model used for Fig. 22 has $\Omega_\Lambda = 0$, so there is no late ISW effect (which would contribute at the very lowest ℓ), and the ISW effect shown is the early ISW effect due to radiation contribution to the expansion law. This effect contributes mainly to the first peak and to the left of it, explaining why the first peak is so much higher than the other peaks. It also shifts the first peak position slightly to the left and changes its shape.

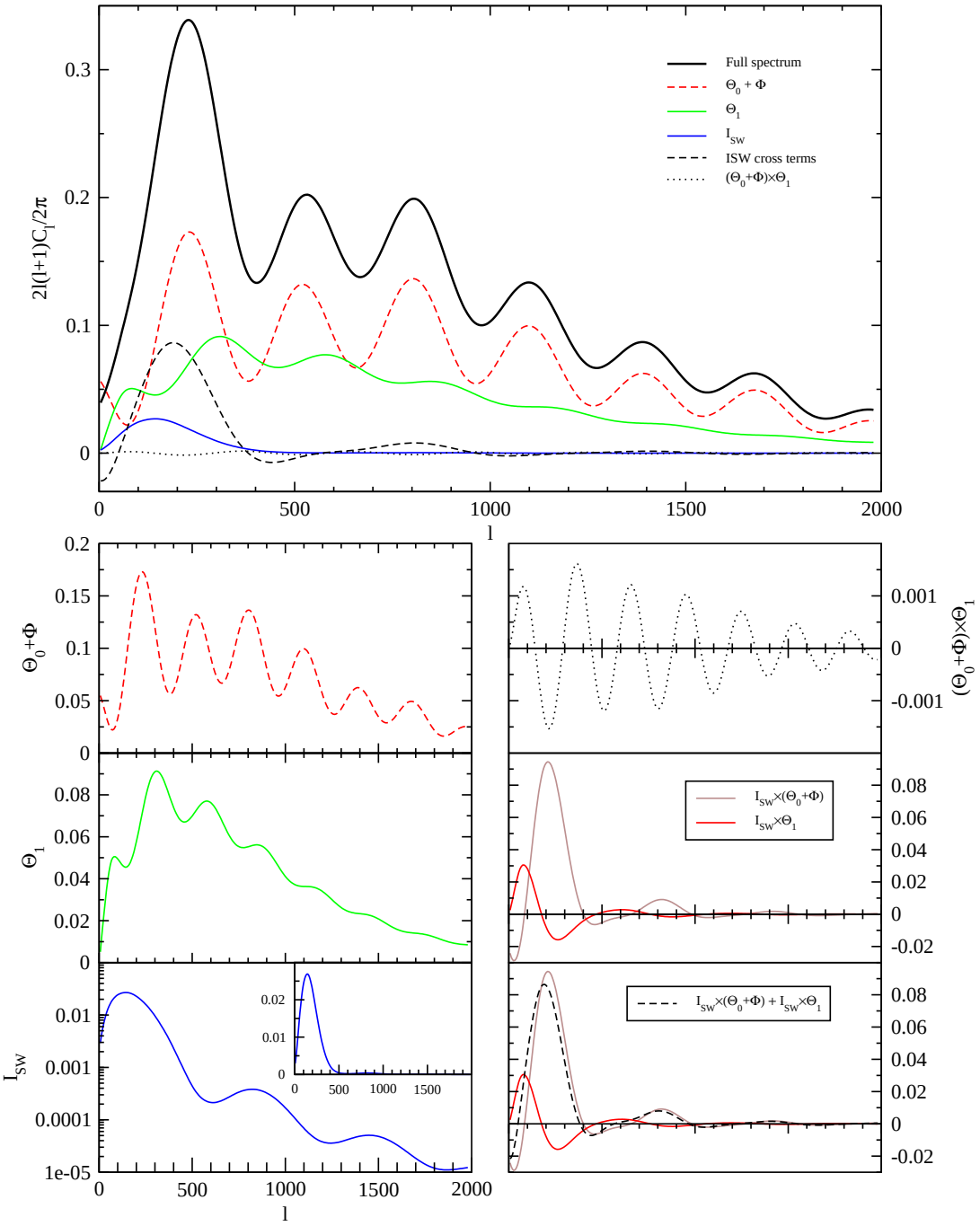

Figure 22: The full C_ℓ spectrum calculated for the cosmological model $\Omega_0 = 1$, $\Omega_\Lambda = 0$, $\omega_m = 0.2$, $\omega_b = 0.03$, $A_s = 1$, $n_s = 1$, and the different contributions to it. (The calculation involves some approximations which allow the description of C_ℓ as just a sum of these contributions and is not as accurate as a CMBFAST or CAMB calculation.) Here Θ_1 denotes the Doppler effect. Figure and calculation by R. Keskitalo.

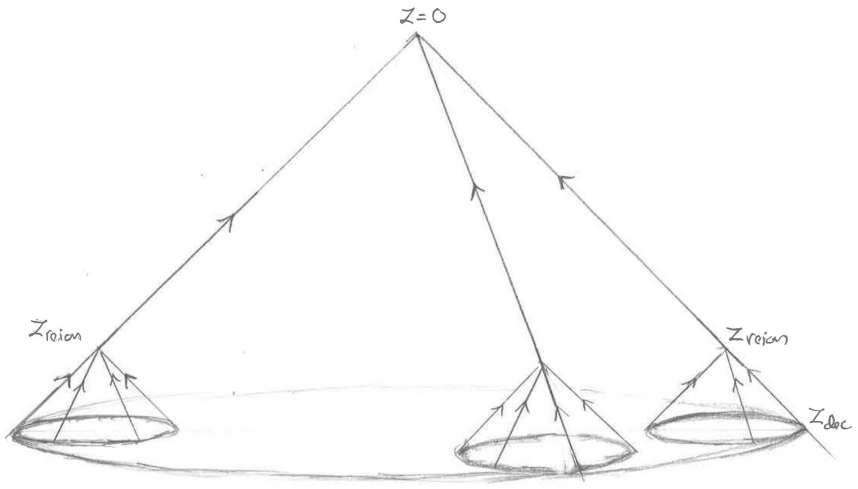

Figure 23: Spacetime diagram of the rescattering of CMB photons due to free electrons released in reionization. The rescattering continues after reionization, but most of it happens relatively soon after it, since the n_e is diluted by expansion.

9.10 Reionization and optical depth

When radiation from the first stars reionizes the intergalactic gas, CMB photons may scatter from the resulting free electrons. The optical depth τ due to reionization is the expectation number of such scatterings per CMB photon. It is expected to be less than 0.1, i.e., most CMB photons do not scatter at all. This rescattering causes additional polarization[13] of the CMB, and CMB polarization measurements are actually the best way to determine τ. Most of this scattering happens relatively soon after the reionization, since the number density of free electrons is diluted by the expansion of the Universe.

The optical depth is thus directly related to the reionization redshift $z_{\rm reion}$. A smaller τ corresponds to later reionization and thus means that the first stars formed later.

Because of this scattering, not all the CMB photons come from the location on the last scattering surface they seem to come from. The effect of the rescattered photons is to mix up signals from different directions and therefore to reduce the CMB anisotropy. The reduction factor on $\delta T/T$ is $e^{-\tau}$ and on the C_ℓ spectrum $e^{-2\tau}$. However, this does not affect the largest scales, scales larger than the area from which the rescattered photons, reaching us from a certain direction, originally came from. Such a large-scale anisotropy has affected all such photons the same way, and thus is not lost in the mixing. See Fig. 23.

[13] Due to time constraints, CMB polarization is not discussed in these lectures.

9.11 Cosmological parameters and CMB anisotropy

Let us finally consider the total effect of the various cosmological parameters on the C_ℓ spectrum. The C_ℓ provides the most important single observational data set for determining (or constraining) cosmological parameters, since it has a rich structure which we can measure with an accuracy that other cosmological observations cannot match, and because it depends on so many different cosmological parameters in many ways. The latter is both a strength and weakness: the number of cosmological parameters we can determine is large, but on the other hand, some feature in C_ℓ may depend on more than one parameter, so that we may only be able to constrain some combination of such parameters, not the parameters individually. We say that such parameters are *degenerate* in the CMB data. Other cosmological observations are then needed to break such degeneracies.

We shall consider 7 "standard parameters":

- Ω_0 total density parameter
- Ω_Λ cosmological constant (or vacuum energy) density parameter
- A_s amplitude of primordial scalar perturbations (at some pivot scale k_p)
- n_s spectral index of primordial scalar perturbations
- τ optical depth due to reionization (discussed in Sec. 9.11.6)
- $\omega_b \equiv \Omega_b h^2$ "physical" baryon density parameter
- $\omega_m \equiv \Omega_m h^2$ "physical" matter density parameter

There are other possible cosmological parameters ("additional parameters") which might affect the C_ℓ spectrum, e.g.,

- m_{ν_i} neutrino masses
- w dark energy equation-of-state parameter
- $\frac{dn_s}{d\ln k}$ scale dependence of the spectral index
- r, n_T relative amplitude and spectral index of tensor perturbations
- B, $n_{\rm iso}$ amplitudes and spectral indices of primordial isocurvature perturbations
- $A_{\rm cor}$, $n_{\rm cor}$ and their correlation with primordial curvature perturbations

We assume here that these additional parameters have no impact, i.e., they have the "standard" values

$$r = \frac{dn}{d\ln k} = B = A_{\rm cor} = 0\,, \quad w = -1\,, \quad \text{and} \quad \sum m_{\nu_i} = 0.06\,\text{meV}\,, \tag{111}$$

to the accuracy which matters for C_ℓ observations. This is both observationally and theoretically reasonable. There is no sign in the present-day CMB data for deviations from these values. On the other hand, significant deviations can be consistent with the current data, and may be discovered by more accurate future observations. The primordial isocurvature perturbations refer to the possibility that the primordial scalar perturbations are not adiabatic, and therefore are not completely determined by the comoving curvature perturbation $\mathcal{R}$.

The assumption that these additional parameters have no impact, leads to a determination of the standard parameters with an accuracy that may be too optimistic, since the standard parameters may have degeneracies with the additional parameters.

9.11.1 Independent vs. dependent parameters

The above is our choice of independent cosmological parameters. Ω_m, Ω_b and H_0 (or h) are then dependent (or "derived") parameters, since they are determined by

$$\Omega_0 = \Omega_m + \Omega_\Lambda \quad \Rightarrow \quad \Omega_m = \Omega_0 - \Omega_\Lambda \tag{112}$$

$$h = \sqrt{\frac{\omega_m}{\Omega_m}} = \sqrt{\frac{\omega_m}{\Omega_0 - \Omega_\Lambda}} \tag{113}$$

$$\Omega_b = \frac{\omega_b}{h^2} = \frac{\omega_b}{\omega_m}(\Omega_0 - \Omega_\Lambda) \tag{114}$$

Note that the Hubble constant $H_0 \equiv h \cdot 100$ km/s/Mpc is now a dependent parameter! We cannot vary it independently, but rather the varying of ω_m, Ω_0, or Ω_Λ also causes H_0 to change.

Different choices of independent parameters are possible within our 7-dimensional parameter space (e.g., we could have chosen H_0 to be an independent parameter and let Ω_Λ to be a dependent parameter instead). They can be thought of as different coordinate systems[14] in this 7D space. *It is not meaningful to discuss the effect of one parameter without specifying what is your set of independent parameters!*

Some choices of independent parameters are better than others. The above choice represents standard practice in cosmology today.[15] The independent parameters have been chosen so that they correspond as directly as possible to physics affecting the C_ℓ spectrum and thus to observable features in it. We want the effects of our independent parameters on the observables to be as different ("orthogonal") as possible in order to avoid parameter degeneracy.

In particular,

- ω_m (not Ω_m) determines $z_{\rm eq}$ and $k_{\rm eq}$, and thus, e.g., the magnitude of the early ISW effect and which scales enter during matter- or radiation-dominated epochs.
- ω_b (not Ω_b) determines the baryon/photon ratio and thus, e.g., the relative heights of the odd and even peaks.
- Ω_Λ (not $\Omega_\Lambda h^2$) determines the late ISW effect.

There are many effects on the C_ℓ spectrum, and parameters act on them in different combinations. Thus there is no perfectly "clean" way of choosing independent parameters. Especially having the Hubble constant as a dependent parameter takes some getting used to.

In the following CAMB[16] plots we see the effect of these parameters on C_ℓ by varying one parameter at a time around a *reference model*, whose parameters have the following values.

Independent parameters:

$$\begin{aligned} \Omega_0 &= 1 & \qquad \Omega_\Lambda &= 0.7 \\ A_s &= 1 & \qquad \omega_m &= 0.147 \\ n_s &= 1 & \qquad \omega_b &= 0.022 \\ \tau &= 0.1 \end{aligned}$$

[14] The situation is analogous to the choice of independent thermodynamic variables in thermodynamics.

[15] There are other choices in use, which are even more geared to minimizing parameter degeneracy. For example, the sound horizon angle ϑ_s may be used instead of Ω_Λ as an independent parameter, since it is directly determined by the acoustic peak separation. However, since the determination of the dependent parameters from it is complicated, such use is more directed towards technical data analysis than pedagogical discussion.

[16] CAMB is a publicly available code for precise calculation of the C_ℓ spectrum. See http://camb.info

which give for the dependent parameters

$$\begin{aligned} \Omega_m &= 0.3 & h &= 0.7 \\ \Omega_c &= 0.2551 & \omega_c &= 0.125 \\ \Omega_b &= 0.0449 \end{aligned}$$

The meaning of setting $A_s = 1$ is just that the resulting C_ℓ still need to be multiplied by the true value of A_s^2. (In this model the true value should be about $A_s = 5 \times 10^{-5}$ to agree with observations.) If we really had $A_s = 1$, perturbation theory of course would not be valid! This is a relatively common practice, since the effect of changing A_s is so trivial that it makes not much sense to plot C_ℓ separately for different values of A_s.

9.11.2 Sound horizon angle

The positions of the acoustic peaks of the C_ℓ spectrum provide us with a measurement of the sound horizon angle

$$\vartheta_s \equiv \frac{r_s(t_{\rm dec})}{d_A^c(t_{\rm dec})}$$

We can use this in the determination of the values of the cosmological parameters, once we have calculated how this angle depends on those parameters. It is the ratio of two quantities, the sound horizon at photon decoupling, $r_s(t_{\rm dec})$, and the angular diameter distance to the last scattering, $d_A^c(t_{\rm dec})$.

Angular diameter distance to last scattering

The angular diameter distance $d_A^c(t_{\rm dec})$ to the last scattering surface we have already calculated and it is given by Eq. (39) as

$$d_A^c(t_{\rm dec}) = H_0^{-1} \frac{1}{\sqrt{|\Omega_0 - 1|}} f_k \left(\sqrt{|\Omega_0 - 1|} \int_{\frac{1}{1+z_{\rm dec}}}^1 \frac{da}{\sqrt{\Omega_0(a - a^2) - \Omega_\Lambda(a - a^4) + a^2}} \right) , \quad (115)$$

from which we see that it depends on the three cosmological parameters H_0, Ω_0 and Ω_Λ. Here $\Omega_0 = \Omega_m + \Omega_\Lambda$, so we could also say that it depends on H_0, Ω_m, and Ω_Λ, but it is easier to discuss the effects of these different parameters if we keep Ω_0 as an independent parameter, instead of Ω_m, since the "geometry effect" of the curvature of space, which determines the relation between the comoving angular diameter distance d_A^c and the comoving distance d^c, is determined by Ω_0.

1. The comoving angular diameter distance is inversely proportional to H_0 (directly proportional to the Hubble distance H_0^{-1}).

2. Increasing Ω_0 decreases $d_A^c(t_{\rm dec})$ in relation to $d^c(t_{\rm dec})$ because of the geometry effect.

3. With a fixed Ω_Λ, increasing Ω_0 decreases $d^c(t_{\rm dec})$, since it means increasing Ω_m, which has a decelerating effect on the expansion. With a fixed present expansion rate H_0, deceleration means that expansion was faster earlier $\Rightarrow$ universe is younger $\Rightarrow$ there is less time for photons to travel as the universe cools from $T_{\rm dec}$ to T_0 $\Rightarrow$ last scattering surface is closer to us.

4. Increasing Ω_Λ (with a fixed Ω_0) increases $d^c(t_{\rm dec})$, since it means a larger part of the energy density is in dark energy, which has an accelerating effect on the expansion. With fixed H_0, this means that expansion was slower in the past $\Rightarrow$ universe is older $\Rightarrow$ more time for photons $\Rightarrow$ last scattering surface is further out. $\therefore$ Ω_Λ increases $d_A^c(t_{\rm dec})$.

Here 2 and 3 work in the same direction: increasing Ω_0 decreases $d_A^c(t_{\rm dec})$, but the geometry effect (2) is stronger. See Fig. 17 for the case $\Omega_\Lambda = 0$, where the dashed line (the comoving distance) shows effect (3) and the solid line (the comoving angular diameter distance) the combined effect (2) and (3).

However, now we have to take into account that, in our chosen parametrization, H_0 is not an independent parameter, but

$$H_0^{-1} \propto \sqrt{\frac{\Omega_0 - \Omega_\Lambda}{\omega_m}}\,,$$

so that via H_0^{-1}, Ω_0 increases and Ω_Λ decreases $d_A^c(t_{\rm dec})$, which are the opposite effects to those discussed above. For Ω_Λ this opposite effect wins. See Fig. 26.

Sound horizon

To calculate the sound horizon,

$$r_s(t_{\rm dec}) \;=\; \int_0^{t_{\rm dec}} \frac{c_s(t)}{a(t)} dt \;=\; \int_0^{a_{\rm dec}} \frac{da}{a\cdot(da/dt)} c_s(a)\,, \tag{116}$$

we need the speed of sound, from Eq. (84),

$$c_s^2(x) = \frac{1}{3}\frac{1}{1+\frac{3}{4}\frac{\bar\rho_b}{\bar\rho_\gamma}} = \frac{1}{3}\frac{1}{1+\frac{3}{4}\frac{\omega_b}{\omega_\gamma}a}\,, \tag{117}$$

where the upper limit of the integral is $a_{\rm dec} = 1/(1+z_{\rm dec})$.

The other element in the integrand of Eq. (116) is the expansion law $a(t)$ before decoupling. From Chapter 3 we have that

$$a\frac{da}{dt} = H_0\sqrt{\Omega_r + \Omega_m a + (1-\Omega_0)a^2 + \Omega_\Lambda a^4}\,. \tag{118}$$

In the integral (115) we dropped the Ω_r, since it is important only at early times, and the integral from $a_{\rm dec}$ to 1 is dominated by late times. Integral (116), on the other hand, includes only early times, and now we can instead drop the Ω_Λ and $1-\Omega_0$ terms (i.e., we can ignore the effect of curvature and dark energy in the early universe, before photon decoupling), so that

$$a\frac{da}{dt} \approx H_0\sqrt{\Omega_m a + \Omega_r} = H_{100}\sqrt{\omega_m a + \omega_r} = \frac{\sqrt{\omega_m a + \omega_r}}{2998\,{\rm Mpc}}\,, \tag{119}$$

where we have written

$$H_0 \equiv h\cdot 100\frac{\rm km/s}{\rm Mpc} \equiv h\cdot H_{100} = \frac{h}{2997.92\,{\rm Mpc}}\,. \tag{120}$$

Thus the sound horizon is given by

$$\begin{aligned} r_s(a) &= 2998\,{\rm Mpc}\int_0^a \frac{c_s(x)dx}{\sqrt{\omega_m x + \omega_r}} \\ &= 2998\,{\rm Mpc}\cdot\frac{1}{\sqrt{3\omega_r}}\int_0^a \frac{dx}{\sqrt{\left(1+\frac{\omega_m}{\omega_r}x\right)\left(1+\frac{3}{4}\frac{\omega_b}{\omega_\gamma}x\right)}}\,. \end{aligned} \tag{121}$$

Here

$$\omega_\gamma = 2.473\times 10^{-5} \qquad \text{and} \tag{122}$$

$$\omega_r = \left[1+\frac{7}{8}N_{\rm eff}\left(\frac{4}{11}\right)^{4/3}\right]\omega_\gamma = 1.692\,\omega_\gamma = 4.184\times 10^{-5} \tag{123}$$

are accurately known from the CMB temperature $T_0 = 2.7255\,\mathrm{K}$ (and therefore we do not consider them as cosmological parameters in the sense of something to be determined from the C_ℓ spectrum).

Thus the sound horizon depends on the two cosmological parameters ω_m and ω_b,

$$r_s(t_{\rm dec}) = r_s(\omega_m, \omega_b)$$

From Eq. (121) we see that increasing either ω_m or ω_b *makes the sound horizon at decoupling,* $r_s(a_{\rm dec})$*, shorter*:

- ω_b slows the sound down
- ω_m speeds up the expansion at a given temperature, so the universe cools to $T_{\rm dec}$ in less time.

The integral (121) can be done and it gives

$$r_s(t_{\rm dec}) = \frac{2998\,\mathrm{Mpc}}{\sqrt{1+z_{\rm dec}}}\frac{2}{\sqrt{3\omega_m R_*}}\ln\frac{\sqrt{1+R_*}+\sqrt{R_*+r_*R_*}}{1+\sqrt{r_*R_*}}\,, \tag{124}$$

where

$$r_* \equiv \frac{\bar\rho_r(t_{\rm dec})}{\bar\rho_m(t_{\rm dec})} = \frac{\omega_r}{\omega_m}(1+z_{\rm dec}) = 0.0456\frac{1}{\omega_m}\left(\frac{1+z_{\rm dec}}{1091}\right) \tag{125}$$

$$R_* \equiv \frac{3\bar\rho_b(t_{\rm dec})}{4\bar\rho_\gamma(t_{\rm dec})} = \frac{3\omega_b}{4\omega_\gamma}\frac{1}{1+z_{\rm dec}} = 27.8\,\omega_b\left(\frac{1091}{1+z_{\rm dec}}\right)\,. \tag{126}$$

For our reference values $\omega_m = 0.147$, $\omega_b = 0.022$, and $1+z_{\rm dec} = 1091$[17] we get $r_* = 0.310$ and $R_* = 0.614$ and $r_s(t_{\rm dec}) = 144\,\mathrm{Mpc}$ for the sound horizon at decoupling.

Summary

The angular diameter distance $d_A^c(t_{\rm dec})$ is the most naturally discussed in terms of H_0, Ω_0, and Ω_Λ, but since these are not the most convenient choice of independent parameters for other purposes, we shall trade H_0 for ω_m according to Eq. (113). Thus we have that the sound horizon angle depends on 4 parameters,

$$\vartheta_s \equiv \frac{r_s(\omega_m,\omega_b)}{d_A^c(\Omega_0,\Omega_\Lambda,\omega_m)} = \vartheta_s(\Omega_0,\Omega_\Lambda,\omega_m,\omega_b) \tag{127}$$

9.11.3 Acoustic peak heights

There are a number of effects affecting the heights of the acoustic peaks:

1. **The early ISW effect.** The early ISW effect raises the first peak. It is caused by the evolution of Φ because of the effect of the radiation contribution on the expansion law after $t_{\rm dec}$. This depends on the radiation-matter ratio at that time; decreasing ω_m makes the early ISW effect stronger.
2. **Shift of oscillation equilibrium by baryons.** (Baryon drag.) This makes the odd peaks (which correspond to compression of the baryon-photon fluid in the potential wells, decompression on potential hills) higher, and the even peaks (decompression at potential wells, compression on top of potential hills) lower.

[17] Photon decoupling temperature, and thus $1+z_{\rm dec}$, depends somewhat on ω_b, but since this dependence is not easy to calculate (recombination and photon decoupling were discussed in Chapter 4), we have mostly ignored this dependence and used the fixed value $1+z_{\rm dec} = 1091$.

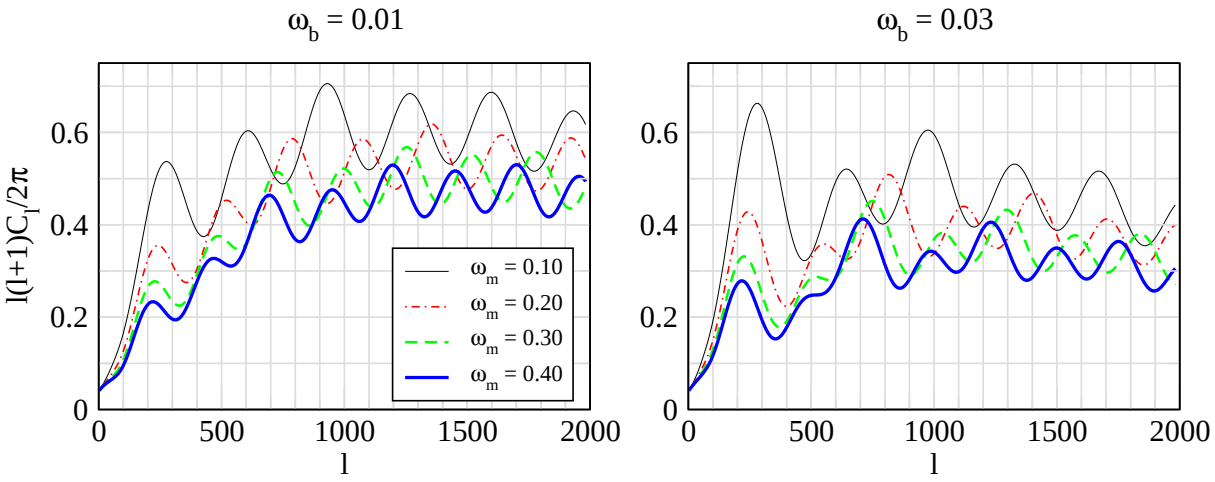

Figure 24: The effect of ω_m. The angular power spectrum C_ℓ is here calculated without the effect of diffusion damping, so that the other effects on peak heights could be seen more clearly. Notice how reducing ω_m raises all peaks, but the effect on the first few peaks is stronger in relative terms, as the radiation driving effect is extended towards larger scales (smaller ℓ). The first peak is raised mainly because the ISW effect becomes stronger. Figure and calculation by R. Keskitalo.

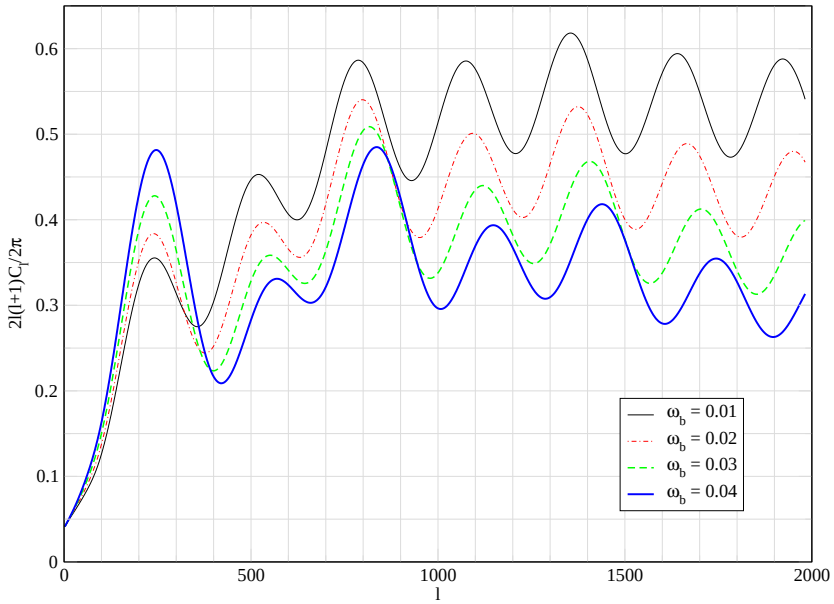

Figure 25: The effect of ω_b. The angular power spectrum C_ℓ is here calculated without the effect of diffusion damping, so that the other effects on peak heights could be seen more clearly. Notice how increasing ω_b raises odd peaks relative to the even peaks. Because of baryon damping there is a general trend downwards with increasing ω_b. This figure is for $\omega_m = 0.20$. Figure and calculation by R. Keskitalo.

3. **Baryon damping.** The time evolution of $R \equiv 3\bar{\rho}_b/4\bar{\rho}_\gamma$ causes the amplitude of the acoustic oscillations to be damped in time roughly as $(1+R)^{-1/4}$. This reduces the amplitudes of all peaks.

4. **Radiation driving.**[18] This is an effect related to horizon scale physics that we have not tried to properly calculate. For scales k which enter during the radiation-dominated epoch, or near matter-radiation equality, the potential Φ decays around the time when the scale enters. The potential keeps changing as long as the radiation contribution is important, but the largest change in Φ is around horizon entry. Because the sound horizon and Hubble length are comparable, horizon entry and the corresponding potential decay always happen during the first oscillation period. This means that the baryon-photon fluid is falling into a deep potential well, and therefore is compressed by gravity by a large factor, before the resulting overpressure is able to push it out. Meanwhile the potential has decayed, so it is less able to resist the decompression phase, and the overpressure is able to kick the fluid further out of the well. This increases the amplitude of the acoustic oscillations. The effect is stronger for the smaller scales which enter when the universe is more radiation-dominated, and therefore raises the peaks with a larger peak number m more. Reducing ω_m makes the universe more radiation dominated, making this effect stronger and extending it towards the peaks with lower peak number m.

5. **Diffusion damping.** Diffusion damping lowers the heights of the peaks. It acts in the opposite direction than the radiation driving effect, lowering the peaks with a larger peak number m more. Because the diffusion damping effect is exponential in ℓ, it wins for large ℓ.

Effects 1 and 4 depend on ω_m, effects 2, 3, and 5 on ω_b. See Figs. 24 and 25 for the effects of ω_m and ω_b on peak heights.

[18] This is also called gravitational driving, which is perhaps more appropriate, since the effect is due to the change in the gravitational potential.

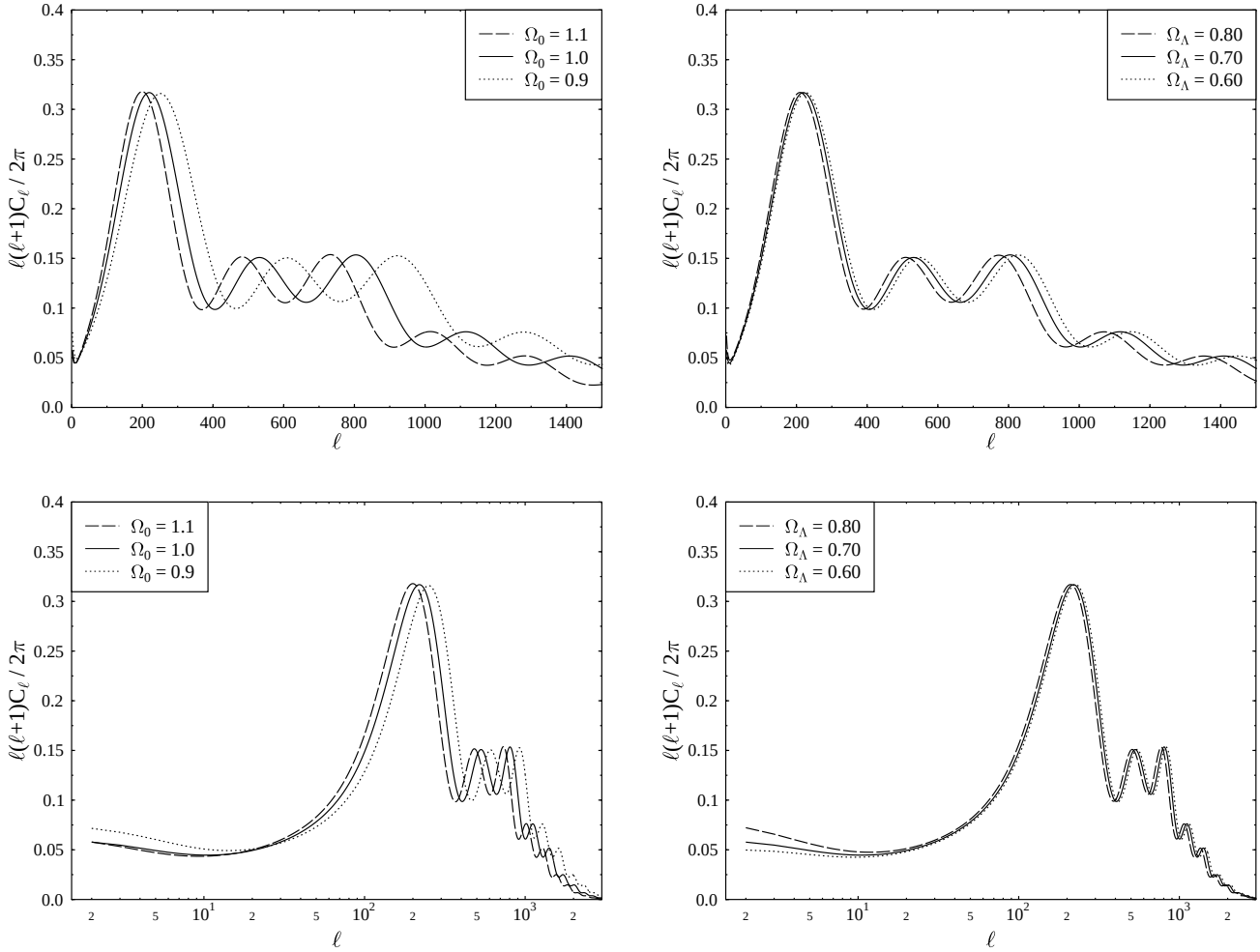

Figure 26: The effect of changing Ω_0 or Ω_Λ from their reference values $\Omega_0 = 1$ and $\Omega_\Lambda = 0.7$. The top panels shows the C_ℓ spectrum with a linear ℓ scale so that details at larger ℓ where cosmic variance effects are smaller can be better seen. The bottom plot has a logarithmic ℓ scale so that the integrated Sachs-Wolfe effect at small ℓ can be better seen. The logarithmic scale also makes clear that the effect of the change in sound horizon angle is to stretch the spectrum by a constant factor in ℓ space.

9.11.4 Effect of Ω_0 and Ω_Λ

These two parameters have only two effects:

1. they affect the sound horizon angle and thus the positions of the acoustic peaks
2. they affect the late ISW effect

See Fig. 26. Since the late ISW effect is in the region of the C_ℓ spectrum where the cosmic variance is large, it is difficult to detect. Thus we can in practice only use ϑ_s to determine Ω_0 and Ω_Λ. Since ω_b and ω_m can be determined quite accurately from C_ℓ acoustic peak heights, peak separation, i.e., ϑ_s, can then indeed be used for the determination of Ω_0 and Ω_Λ. Since one number cannot be used to determine two, the parameters Ω_0 and Ω_Λ are degenerate. CMB observations alone cannot be used to determine them both. Other cosmological observations (like the power spectrum $P_\delta(k)$ from large scale structure, or the SNIa redshift-distance relationship) are needed to break this degeneracy.

A fixed ϑ_s together with fixed ω_b and ω_m determine a line on the (Ω_0, Ω_Λ) -plane. See Fig. 27. Derived parameters, e.g., h, vary along that line. As you can see from Fig. 26, changing Ω_0 (around the reference model) affects ϑ_s much more strongly than changing Ω_Λ. This means

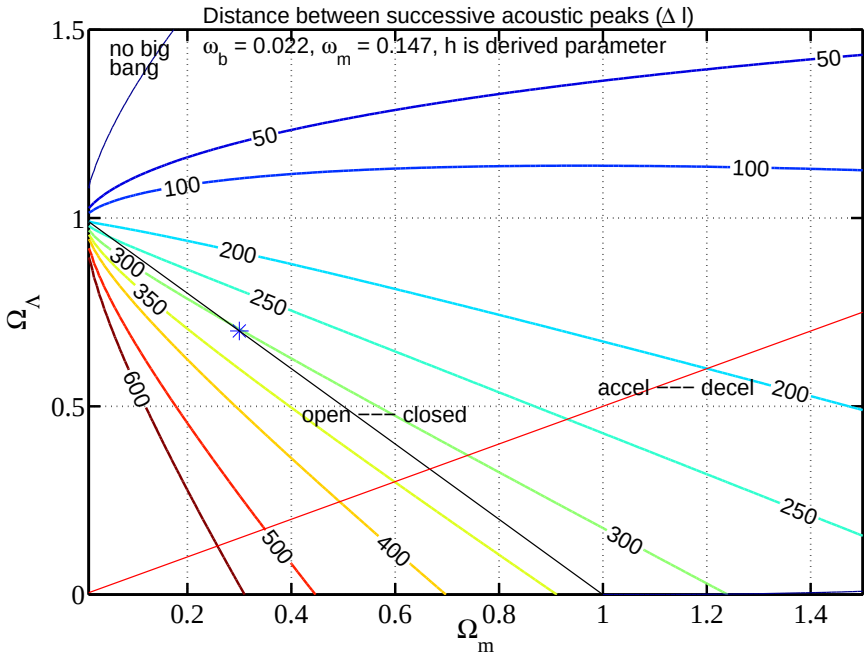

Figure 27: The lines of constant sound horizon angle ϑ_s on the $(\Omega_m,\Omega_\Lambda)$ plane for fixed ω_b and ω_m. The numbers on the lines refer to the corresponding acoustic scale $\ell_A \equiv \pi/\vartheta_s$ ($\sim$ peak separation) in multipole space. Figure by J. Väliviita. See his PhD thesis[10], p.70, for an improved version including the HST constraint on h.

that the orientation of the line is such that Ω_Λ varies more rapidly along that line than Ω_0. Therefore using additional constraints from other cosmological observations, e.g., the Hubble Space Telescope determination of h based on the distance ladder, which select a short section from that line, gives us a fairly good determination of Ω_0, leaving the allowed range for Ω_Λ still quite large.

Therefore it is often said that CMB measurements have determined that $\Omega_0 \sim 1$. But as explained above, this determination necessary requires the use of some auxiliary cosmological data besides the CMB.

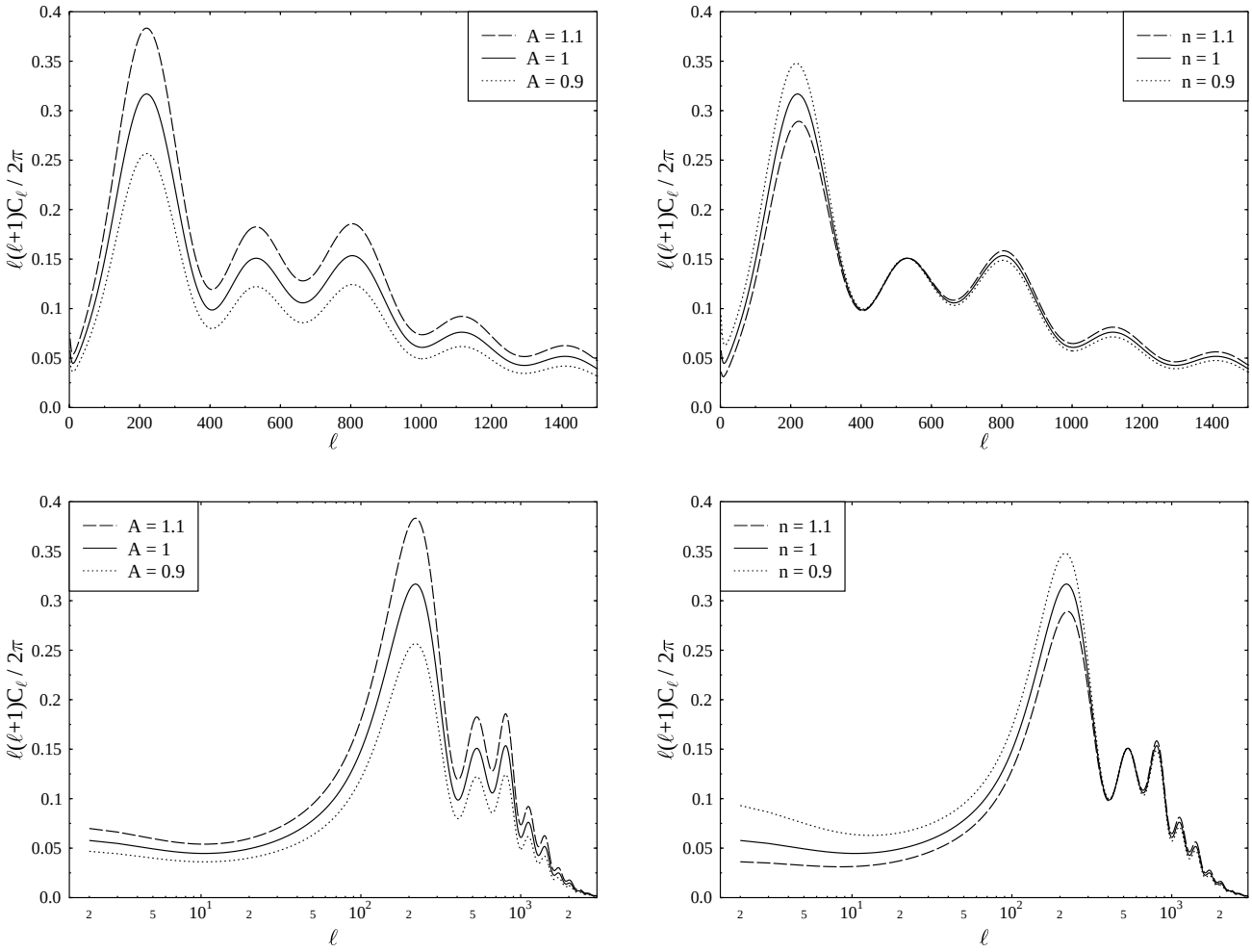

Figure 28: The effect of changing the primordial amplitude and spectral index from their reference values $A_s = 1$ and $n_s = 1$.

9.11.5 Effect of the primordial spectrum

The effect of the primordial spectrum is simple: raising the amplitude A_s raises the C_ℓ also, and tilting the primordial spectrum tilts the C_ℓ also. See Fig. 28.

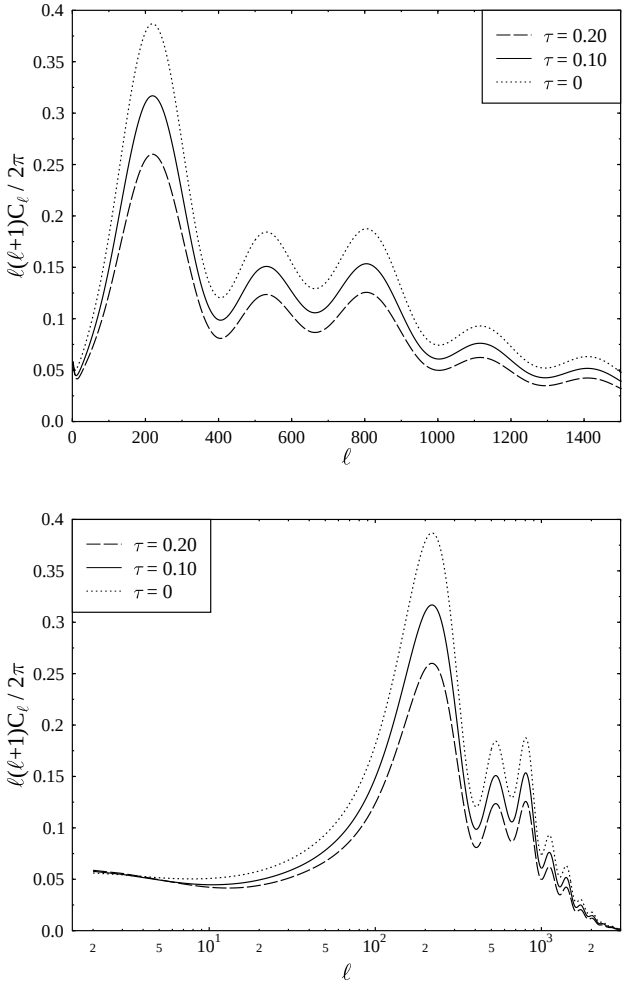

Figure 29: The effect of changing the optical depth from its reference value $\tau = 0.1$.

9.11.6 Optical depth due to reionization

The optical depth τ due to reionization was discussed in Sec. 9.10. See Fig. 29 for its effect on C_ℓ.

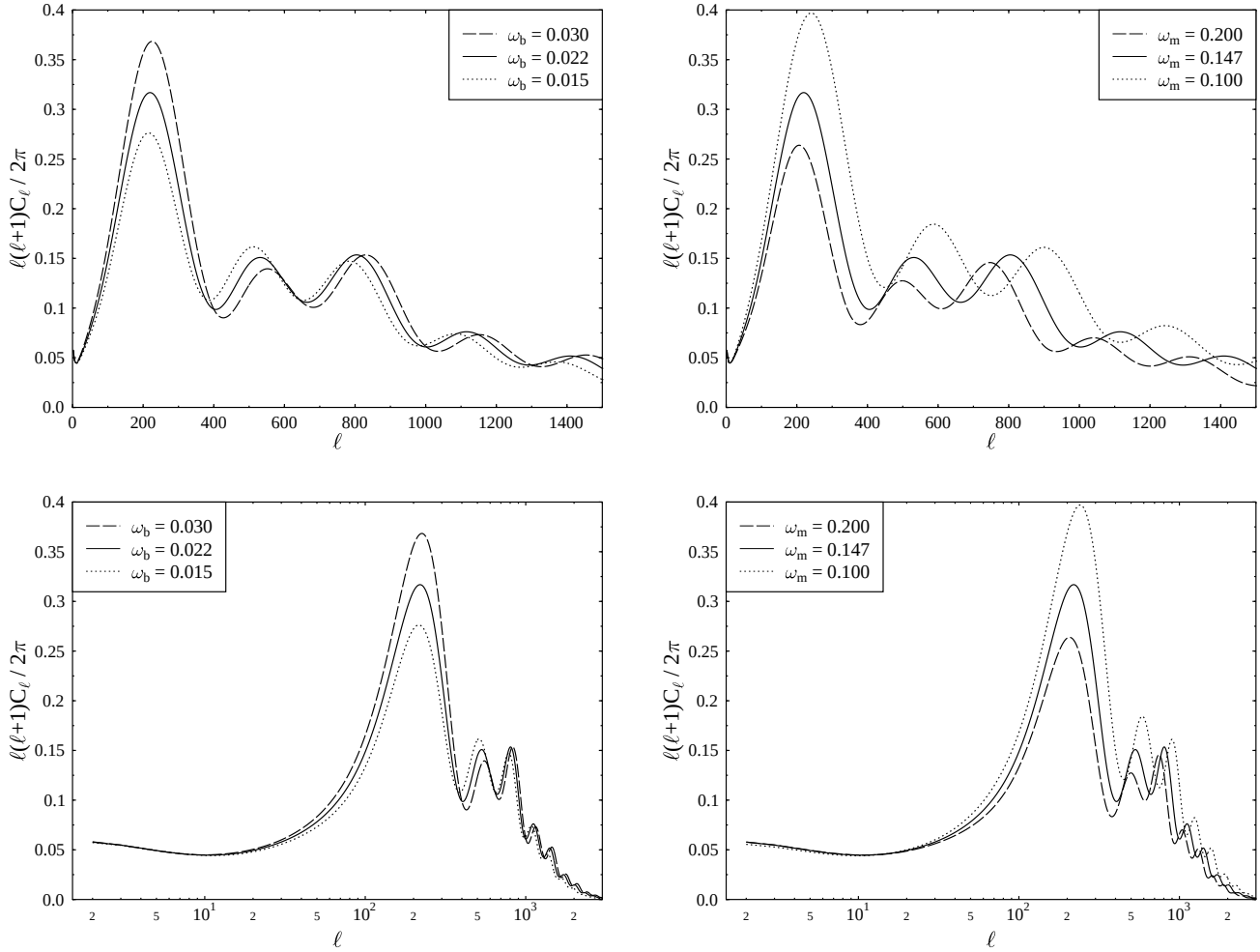

Figure 30: The effect of changing the physical baryon density and matter density parameters from their reference values $\omega_b = 0.022$ and $\omega_m = 0.147$.

9.11.7 Effect of ω_b and ω_m

These parameters affect both the positions of the acoustic peaks (through ϑ_s) and the heights of the different peaks. The latter effect is the more important, since both parameters have their own signature on the peak heights, allowing an accurate determination of these parameters, whereas the effect on ϑ_s is degenerate with Ω_0 and Ω_Λ.

Especially ω_b has a characteristic effect on peak heights: Increasing ω_b raises the odd peaks and reduces the even peaks, because it shifts the balance of the acoustic oscillations (the $-R\Phi$ effect). This shows the most clearly at the first and second peaks. Raising ω_b also shortens the damping scale k_D^{-1} due to photon diffusion, moving the corresponding damping scale ℓ_D of the C_ℓ spectrum towards larger ℓ. This has the effect of raising C_ℓ at large ℓ. See Fig. 30.

There is also an overall "baryon damping effect" on the acoustic oscillations which we have not calculated. It is due to the time dependence of $R \equiv 3\bar{\rho}_b/4\bar{\rho}_m$, which reduces the amplitude of the oscillation by about $(1+R)^{-1/4}$. This explains why the third peak in Fig. 30 is no higher for $\omega_b = 0.030$ than it is for $\omega_b = 0.022$.

Increasing ω_m makes the universe more matter dominated at $t_{\rm dec}$ and therefore it reduces the early ISW effect, making the first peak lower. This also affects the shape of the first peak.

The "radiation driving" effect is most clear at the second to fourth peaks. Reducing ω_m makes these peaks higher by making the universe more radiation-dominated at the time the corresponding scales enter, strengthening this radiation driving. The fifth and further peaks

Parameters for the ΛCDM model

	Planck 2018	best fit
ω_b	0.02237 ± 0.00015	0.022383
ω_m	0.1424 ± 0.0012	0.14249
Ω_Λ	0.685 ± 0.007	0.6841
τ	0.054 ± 0.007	0.0543
A_s	$4.58 \pm 0.04 \times 10^{-5}$	4.5832×10^{-5}
n_s	0.965 ± 0.004	0.96605
H_0	67.36 ± 0.54 km/s/Mpc	67.32 km/s/Mpc
ω_c	0.1200 ± 0.0012	0.12011
Ω_m	0.315 ± 0.007	0.3158
$z_{\rm eq}$	3402 ± 26	
$k_{\rm eq}^{-1}$	96.3 ± 0.8 Mpc	
$z_{\rm dec}$	1089.92 ± 0.25	
k_D^{-1}	7.10 ± 0.02 Mpc	
$z_{\rm reion}$	7.7 ± 0.7	7.68
ϑ_s	$0.5965^\circ \pm 0.0002^\circ$	0.59651°
t_0	$13.797 \pm 0.023 \times 10^9$ a	13.7971×10^9 a

Table 2: These parameter values are based on the CMB temperature power spectrum C_ℓ, CMB polarization, and gravitational lensing of the CMB, as observed by the Planck satellite [5]. The first six parameters, above the line, are independent parameters, and the parameters below the line are quantities that can be derived from them in the ΛCDM model. The error estimates are 68% confidence limits. The bets-fit column gives a representative model that is an excellent fit to the data; nearby models in the 6-parameter space may be practically equally good fits. Note that here Ω_m includes the contribution from neutrinos with $\sum m_\nu = 0.06$ meV ($\Omega_\nu = 0.0014$) whereas ω_m does not.

correspond to scales that have anyway essentially the full effect, and for the first peak this effect is anyway weak. (We see instead the ISW effect in the first peak.) See Fig. 30.

9.12 Current best estimates for the cosmological parameters

9.12.1 Planck values for ΛCDM parameters

The most important data set for determining cosmological parameters is the Planck data [5] on the CMB anisotropy. We give the parameter values determined by Planck for the ΛCDM model in Table 2. Note that all independent parameters of the model are fit simultaneously to the same data. The determination is based on the assumption that the model, here ΛCDM, is correct. One can judge this assumption based on how well the model fits the data. In the case of Planck and ΛCDM the fit is good; adding more parameters to the model does not improve the fit significantly.

This model agrees reasonable well with most of the other available cosmological data, with the exception of the distance-ladder determination of the Hubble constant, based on Cepheids and Type Ia supernovae, which gives $H_0 = 73.5 \pm 1.6$ km/s/Mpc [11, 12]. This is called the *local* measurement of H_0, since these measurements are from nearby parts of the Universe, in contrast to the *global* determination from the CMB, where the CMB has traversed the entire observable Universe. This discrepancy has been evident in the data for some time, but it has gradually become more serious as the error bars on H_0 from both CMB and local measurements have become tighter without the central values changing much. One may suspect systematic errors in the distance ladder data or that the ΛCDM model is a too simple model for the universe.

Constraints for extended models

	ΛCDM	Planck 2018	Planck+ext
Ω_0	1.0	1.011 ± 0.013	0.9993 ± 0.0037
r	0	< 0.101	< 0.065
$dn_s/d\ln k$	0	-0.005 ± 0.013	-0.004 ± 0.013
w	-1	-1.6 ± 0.5	-1.04 ± 0.10
$\sum m_\nu$	0.06 eV	< 0.241 eV	< 0.120 eV
$N_{\rm eff}$	3.046	2.89 ± 0.38	2.99 ± 0.34

Table 3: Each row is a different model and we show limits only to the "additional" parameter. As is customary with limits, the ranges are given as 95% confidence limits. $N_{\rm eff}$, the "effective number of neutrino species", refers to relativistic energy density (in addition to photons) near the time of photon decoupling.

9.12.2 Extended models and external data

In the ΛCDM model the universe is flat, $\Omega_0 = 1$. We can also fit *extended models*, with additional independent parameters. Such 7-parameter models, with one extra parameter in addition to the ΛCDM parameters, are fit to Planck data in Table 3. Since the ΛCDM model is a good fit, the estimates for these extra parameters are consistent with their values in the ΛCDM model. Instead of the central value, we therefore concentrate on the estimated probable range, i.e., *limits* to the deviation from the ΛCDM model. Note that in these extended models the ranges for the 6 ΛCDM parameters will be different from Table 2; they will be wider and the central values will be slightly different. One could of course consider models with more independent parameters, e.g., the 12-parameter model, where all the 6 parameters of Table 3 were added to ΛCDM. In such a model the allowed ranges for all these parameters would be wider than in Tables 2 and 3. The argument against such a model is *Occam's razor*: if there are many models that fit the data, one should prefer the simplest one; a corollary to this is that the models one should consider next are those that are almost as simple. Of course, there is no guarantee against all these parameters having a significant effect on the CMB. These one-parameter extensions to ΛCDM do not relieve the tension with the local determination of H_0 much, but by adding sufficiently many additional parameters one can get rid of the tension.

Dark radiation. The parameter $N_{\rm eff}$ corresponds to making ω_r a free parameter. From the discussion in Sec. 9.11.2 we see that we are constraining relativistic energy density at or before $t_{\rm dec}$. Additional relativistic particle species, in addition to photons and neutrinos, would raise $N_{\rm eff}$ above the Particle Physics Standard Model value 3.046. The 95% confidence upper limit for the contribution from such extra species is $\Delta N_{\rm eff} \equiv N_{\rm eff} - 3.046 < 0.3$. This rules out any new (currently unknown) particles that would decouple after QCD transition and stay relativistic until photon decoupling, see Fig. 31.

External data. Because of degeneracies of cosmological parameters in the CMB data, most importantly the *geometrical degeneracy* between parameters, like Ω_0, Ω_Λ, and the dark energy equation-of-state parameter w, whose main effect on CMB is via their effect on the angular diameter distance to the last scattering sphere, some parameters of these extended models are only weakly constrained by Planck data. To break these degeneracies, additional cosmological data (BAO and BICEP2/Keck, see below) has been used in the fourth column of Table 3 (ext = external to Planck). The impressive accuracy in this column is, however, mainly due to the accuracy of Planck. The parameter values allowed by Planck form a narrow but long region in the 7-parameter space, and the external data allows a region that is wider, but oriented differently; the intersection of these regions is then a shorter segment of the region allowed by Planck alone, see Fig. **??**.

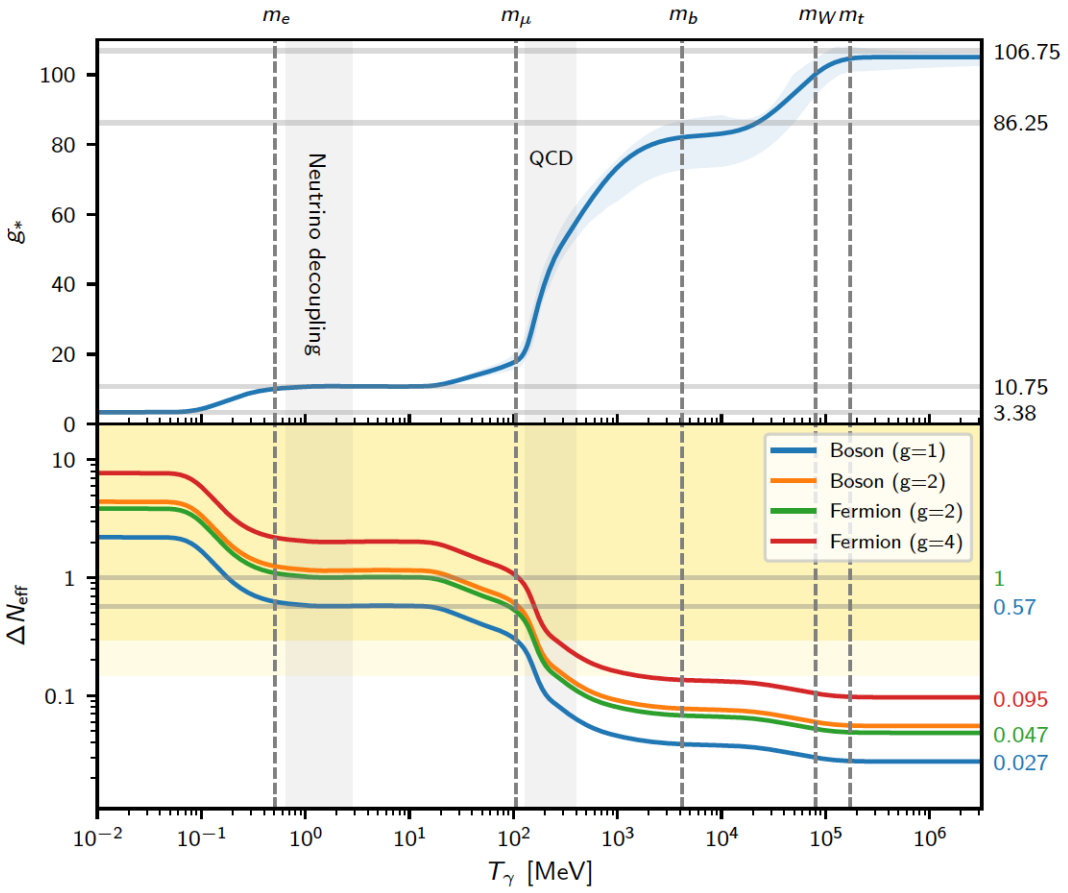

Figure 31: Upper panel: The effective number $g_*(T)$ of degrees of freedom in the Standard Model of particle physics. Note that the drop in $g_*(T)$ due to the QCD transition is not sharp, since this is not a phase transition (taking place at a fixed critical temperature T_c), but is a cross-over transition (happening gradually over a temperature range). Bottom panel: The colored curves show contributions to $\Delta N_{\rm eff}$ from different types of light (relativistic at photon decoupling) thermal relics as a function of their decoupling temperature. The darker yellow region is ruled out by the Planck upper limit $\Delta N_{\rm eff} < 0.3$. (The lighter yellow region corresponds to the 68% confidence upper limit $\Delta N_{\rm eff} < 0.13$.) From [5].

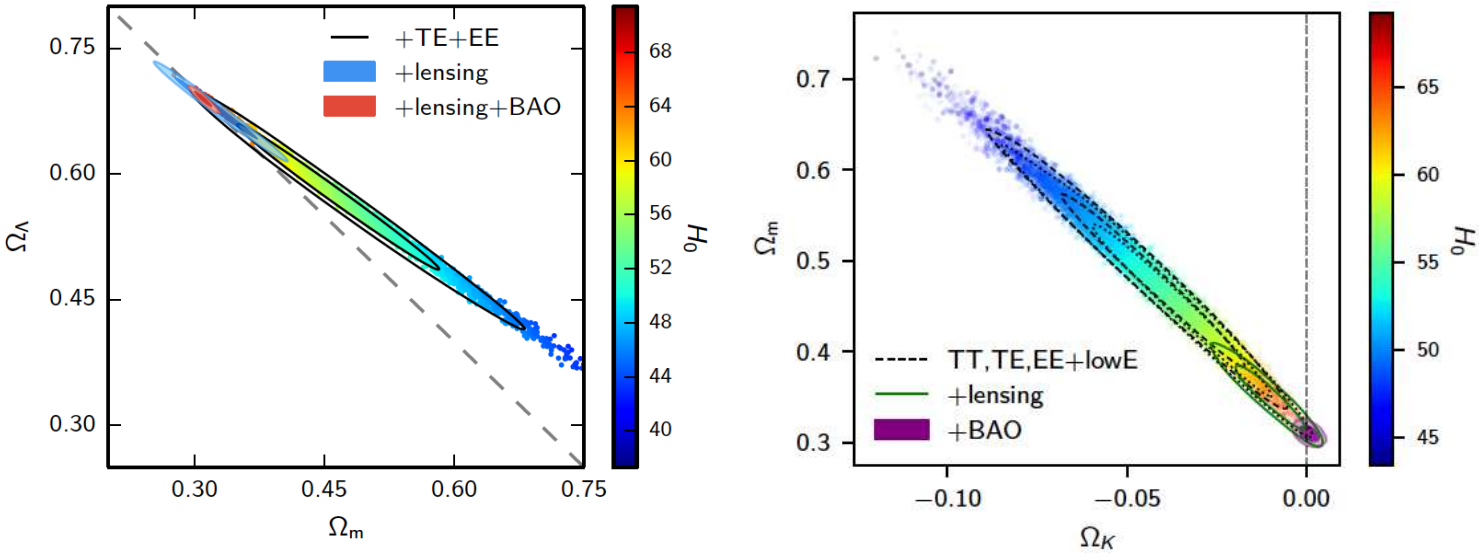

Figure 32: Left: Constraints on Ω_Λ and Ω_m (or $\Omega_0 = \Omega_\Lambda + \Omega_m$) in the ΛCDM+Ω_0 model from Planck 2015 and BAO data. The colored dots represent parameter values that fit Planck temperature C_ℓ and large scale polarization data, the color giving the value of H_0 required for the fit. The black contours (inner 68% and outer 95% confidence limits) give the models that remain allowed when Planck small-scale polarization data is also used; and blue contours when Planck CMB lensing data is used instead. The red contours show the effect of adding BAO data to break the Ω_0-Ω_Λ degeneracy. From the colors one can see that also independent H_0 data could be used to break the degeneracy. The dashed line corresponds to a flat universe. From [3]. Right: The same from Planck 2018 data, except shown for (Ω_k,Ω_m) instead of (Ω_m,Ω_Λ). From [5].

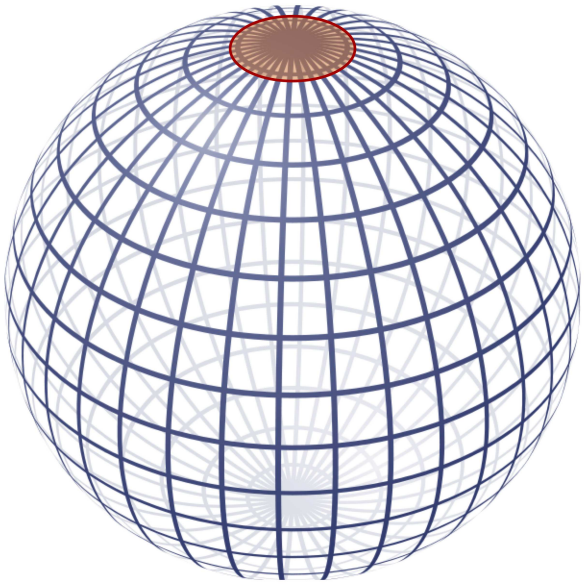

Figure 33: The upper limit $\Omega_0 < 1.003$ means that if we live in a closed universe, its curvature radius $R_{\rm curv} = H^{-1}/\sqrt{|\Omega_k|} > H^{-1}/\sqrt{0.003} = 18.3H^{-1} = 5.9d^c(z = 1090)$ is more than 5 times larger than the distance we can see (to the last scattering sphere, corresponding to the red circle, which is actually drawn too large here, since this figure was drawn when the limit was weaker).

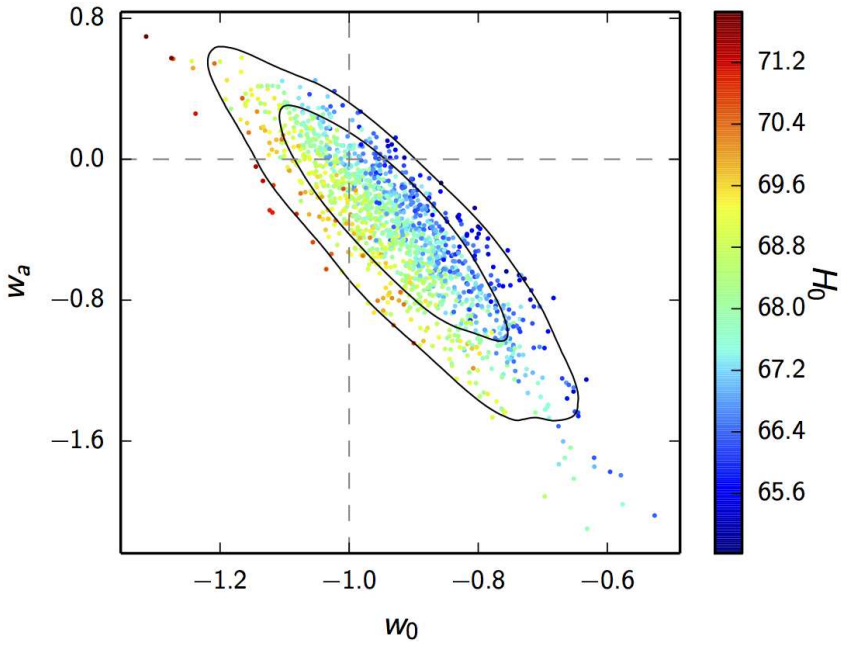

Figure 34: Constraints on the dark energy equation-of-state parameters w_0 and w_a (see text) in the 8-parameter $(w_0 + w_a)$CDM model from Planck, BAO, and SNIa data. From [3].

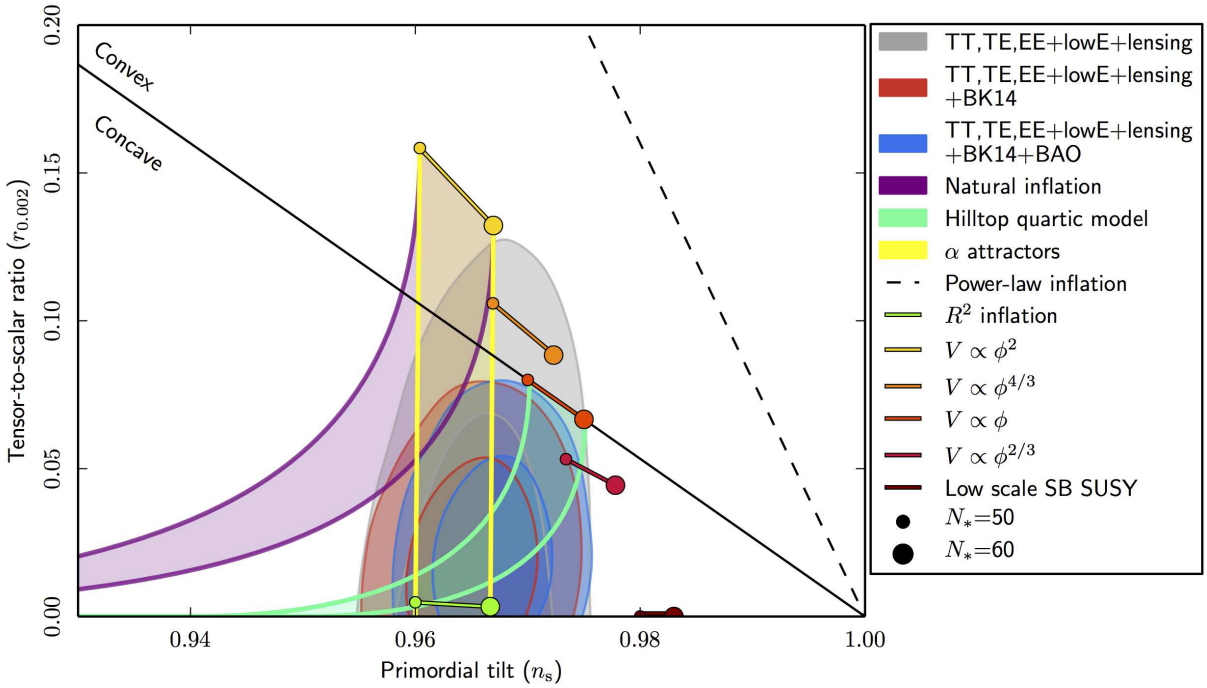

Figure 35: Constraints on the parameters n_s and r, which constrain inflation models, in the 7-parameter ΛCDM+r model from Planck data. Gray contours are based on Planck data only; red and blue contours include external data. Predictions from a selection of inflation models are marked on the plot. From [7].

Large scale structure surveys, i.e., the measurement of the 3-dimensional matter power spectrum $P_\delta(k)$ from the distribution of galaxies, mainly measure the combination $\Omega_m h$, since this determines where $P_\delta(k)$ turns down. Actually it turns down at $k_{\rm eq}$ which is proportional to $\omega_m \equiv \Omega_m h^2$, but since in these surveys the distances to galaxies are deduced from their redshifts (these surveys are also called galaxy redshift surveys), which give the distances only up to the Hubble constant H_0, these surveys determine $h^{-1}k_{\rm eq}$ instead of $k_{\rm eq}$. This cancels one power of h. Having $\Omega_m h^2$ from CMB and $\Omega_m h$ from the galaxy surveys, gives us both h and $\Omega_m = \Omega_0 - \Omega_\Lambda$, which breaks the Ω_0-Ω_Λ degeneracy.

BAO. Measurements of $P_\delta(k)$ are now so accurate that the small residual effect from the acoustic oscillations before photon decoupling can be seen as a weak wavy pattern [13]. This is the same structure which we see in the C_ℓ but now much fainter, since now the baryons have fallen into the CDM potential wells, and the CDM was only mildly affected by these oscillations in the baryon-photon fluid. In this context these are called *baryon acoustic oscillations* (BAO). The half-wavelength of this pattern, however, corresponds to the same sound horizon distance $r_s(t_{\rm dec})$ in both cases.[19] But now the angular scale on the sky is related to it by the angular diameter distance $d_A^c(z)$ to the much smaller redshifts z of the galaxy survey. This $d_A^c(z)$ has then a different relation to Ω_0, Ω_Λ, and ω_m. Comparing CMB data to galaxy surveys gives us the ratio $d_A^c(z)/d_A^c(t_{\rm dec})$, which gives us independent information on these parameters. The large scale structure surveys used for the BAO measurements to supplement Planck 2018 data were the 6dF Galaxy Survey (6dFGS) [14] and the Sloan Digital Sky Survey (SDSS) [15, 16].

Curvature. Because of the geometrical degeneracy, the CMB angular power spectra alone are not good for constraining Ω_k. The peak structure gives a precise measurement of the angular diameter distance to last scattering $d_A^c(t_{\rm dec})$. In the ΛCDM+Ω_k model his translates into a curve on the (Ω_m, Ω_Λ) plane (see Fig. 27). The late ISW effect due to Ω_Λ would break this degeneracy, but since this affects only the lowest multipoles it is lost in the cosmic variance. More significant is a higher-order (beyond linear perturbation theory) effect on the C_ℓ; that of gravitational lensing of the CMB due to large-scale structure. This smooths the acoustic peaks and the effect is proportional to Ω_m. Although the effect is small, it occurs at high ℓ where cosmic variance is small and provides some degeneracy breaking power between Ω_m and Ω_Λ, or equivalently, between Ω_m and Ω_k. The resulting constraint, from Planck C_ℓ only, on Ω_k is $\Omega_k = -0.044^{+0.018}_{-0.015}$ (68% CL), which favors a closed universe at well over 2 σ. The best-fit such models have $\Omega_m > 0.45$ and $H_0 < 55\,$km/s/Mpc, which are ruled out by other cosmological data. The problematic feature in the data is that the acoustic peaks are slightly lower than predicted by the ΛCDM model fit to the data, as if there was too much lensing (requiring higher Ω_m, which then leads to lower Ω_Λ and negative Ω_k as we move along the degeneracy line).

From the Planck data one can also measure the gravitational lensing of the CMB more directly from the effect it has on higher-order correlations (higher than the 2-point correlation measured by C_ℓ) of the CMB. This measurement of CMB lensing agrees with the ΛCDM prediction and thus with a flat universe, giving the constraint $\Omega_k = -0.0106 \pm 0.00065$ (when combined with the Planck C_ℓ). When one adds also BAO data to break the geometric degeneracy, one arrives at the final result given in the Planck+ext column of Table 3,

$$\Omega_k = 0.0007 \pm 0.0019 \qquad (68\%\text{CL})\,. \tag{128}$$

(Table 3 gives 95% confidence limits, which are twice as wide.) The 95% upper limit $\Omega_0 < 1.003$, or $\Omega_k > -0.003$ gives a minimum size to the Universe, see Fig. 33.

Supernovae. Another way to break the geometric degeneracy, is to use the redshift-distance relationship from Supernova Type Ia (SNIa) surveys [17], or simply the distance-ladder determination of H_0, where Cepheids and Supernovae are the last two steps of the ladder. These were

[19] To be accurate, the $t_{\rm dec}$ value to represent the effect in $P_\delta(k)$, is not exactly the same as for C_ℓ, since photon decoupling was not instantaneous, and in one we are looking at the effect on matter and in the other on photons.

not used in the Planck 2018 analysis of 6- and 7-parameter models, because of the discrepancy with the local H_0 determination[20], and since the SNIa data adds little statistical power to the CMB+BAO combination, but the SNIa data was used for the following 8-parameter model.

Dark energy. To constrain properties of dark energy, the 7-parameter wCDM model is probably too simplistic, since it assumes that the equation-of-state parameter w stays constant during the epoch when dark energy has a significant effect on the expansion. To stay at a phenomenological level, i.e., not assuming a particular dark-energy model, but just attempting to constrain its equation of state, the next step is a two-parameter equation of state $w(a) = w_0 + w_a(1-a)$, i.e., a first-order Taylor expansion with w_0 the current value of w, and w_a related to its first derivative with respect to the scale factor, leading to an 8-parameter model. From Fig. 34 you can see that the best fits are near the ΛCDM values $w_0 = -1$, $w_a = 0$, but that the equation of state is poorly constrained.

Neutrino masses. Neutrino masses, i.e., the amount of hot dark matter, have a larger effect on large-scale structure than CMB; the CMB data is mainly needed to determine the other parameters after which the large-scale structure power spectrum $P_\delta(k)$ can be used to determine the sum of the neutrino masses. The value 0.06 eV used for the ΛCDM model is the minimum allowed by neutrino oscillation data.

Tensor perturbations. The polarization pattern of the CMB on the sky can be divided into what are called E and B modes. This is analogous to the division of a vector field into irrotational (curl-free) and rotational (divergence-free) parts. To first (i.e. linear) order in perturbation theory, only tensor perturbations produce B-mode polarization in the CMB. Only E-mode polarization has so far been detected in the CMB. Upper limits to CMB B-mode polarization provide upper limits to the tensor-scalar ratio r. Planck was not optimized for polarization measurements, so its B-mode measurement is noisy and suffers from instrument systematics. Thus the Planck upper limit to r from B modes is weak, $r < 0.41$, and the Planck constraint $r < 0.101$ comes from the effect of tensor perturbations on the CMB temperature C_ℓ. The ground-based BICEP2/Keck Array [18] at the South Pole can measure polarization more accurately, but it has limited sky coverage and needs to be combined with Planck data to separate the CMB from the foreground. This combination leads to the B-mode upper limit $r < 0.065$.

Inflation models. Since inflation produces tensor perturbations, and many inflation models predict that they should be strong enough to have an observable effect on the CMB, the simplest way to constrain inflation is to fit the ΛCDM+r model to CMB data. From Fig. 35 you can see that the $V(\varphi) = \frac{1}{2}m^2\varphi^2$ inflation model, is ruled out by Planck data alone at a 95% confidence level (assuming that ΛCDM+r is the correct model for the universe).

[20] One should not combine discrepant data in parameter fitting. This would lead to artificially tight parameter values with poor fits to both data sets.

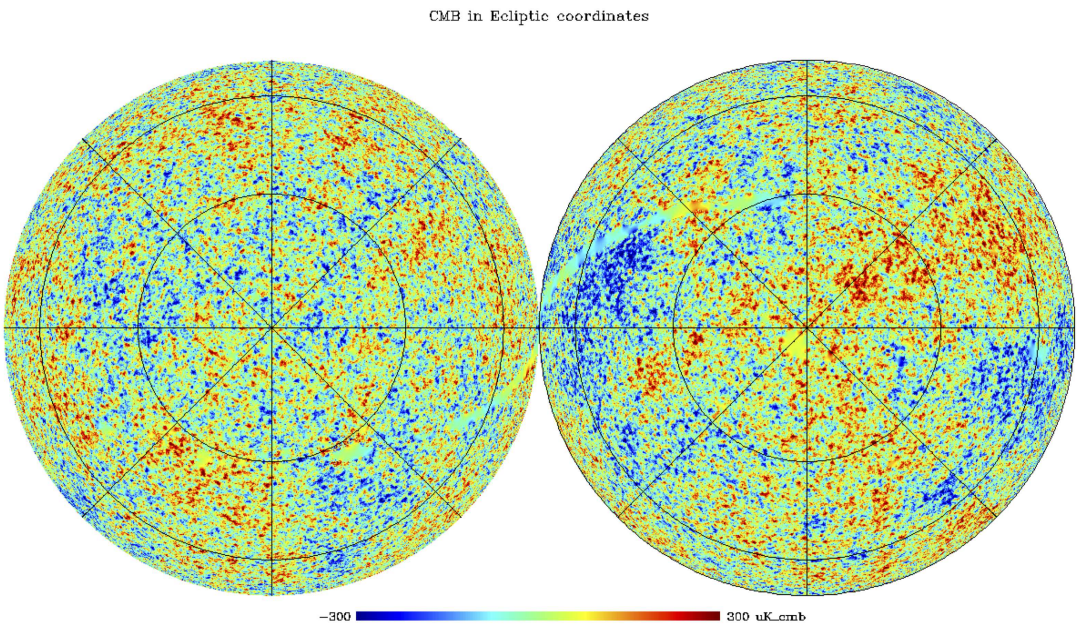

Figure 36: CMB temperature anisotropy in ecliptic coordinates.

9.13 Issues with CMB data

While the agreement of the CMB observations with the predictions of the ΛCDM model is impressive (see Fig. 11), it is not perfect. Also, while combining other cosmological data with CMB data adds more support for the ΛCDM model, there are some discrepancies. There are at least three issues:

Large scale anomalies. Comparing the northern (Fig. 6) and southern (Fig. 7) galactic hemispheres, one may notice that the southern hemisphere has stronger large-scale CMB anisotropies. The difference is more clear between the ecliptic hemispheres, see Fig. 36. This is not what we would expect from statistical isotropy. Also the quadrupole and octupole have planar shape ($m = \ell$ dominates, see the Y_{22} and Y_{33} in Fig. 10) and are aligned with each other (and the quadrupole is rather weak). These large-scale anomalies are seen in both WMAP and Planck data, so they are real. They may be just a statistical fluke, or a sign that the Universe deviates from standard ΛCDM at the very largest observable scales. Because of cosmic variance it is difficult to tell.

"Lensing smoothing". While the scatter of data points around the theoretical prediction (see Fig. 37) is mainly as expected (the error bars are 68% CL, so we expect 32% of the data points deviate from the prediction by more than the error bar), there are some features. Data for the low multipoles $\ell < 30$ are mostly below prediction. This is due to the lack of large-scale power in the northern ecliptic hemisphere, and thus related to the large-scale anomalies. In the range $\ell = 1100$–2000 the data residuals seem to oscillate in opposite phase to the acoustic peak pattern, i.e., the acoustic peaks in the data are slightly smoothed compared to theoretical prediction. Gravitational lensing of the CMB by the large-scale structure causes such smoothing, and it is as if this smoothing effect is some 10–20% larger than predicted by ΛCDM. These features can be fit better with the ΛCDM+Ω_k model with negative Ω_k (closed universe), but the Planck direct measurement of CMB lensing (from higher-order correlations) and other cosmological data disagrees with such a model.

Local vs global Hubble constant. The Planck ΛCDM value for the Hubble constant, $H_0 = 67.36 \pm 0.54\,\mathrm{km/s/Mpc}$ disagrees with distance-ladder measurements, which give, e.g., $H_0 = 74.0 \pm 1.4\,\mathrm{km/s/Mpc}$ [19]. One may think of many possible causes for this discrepancy. 1)

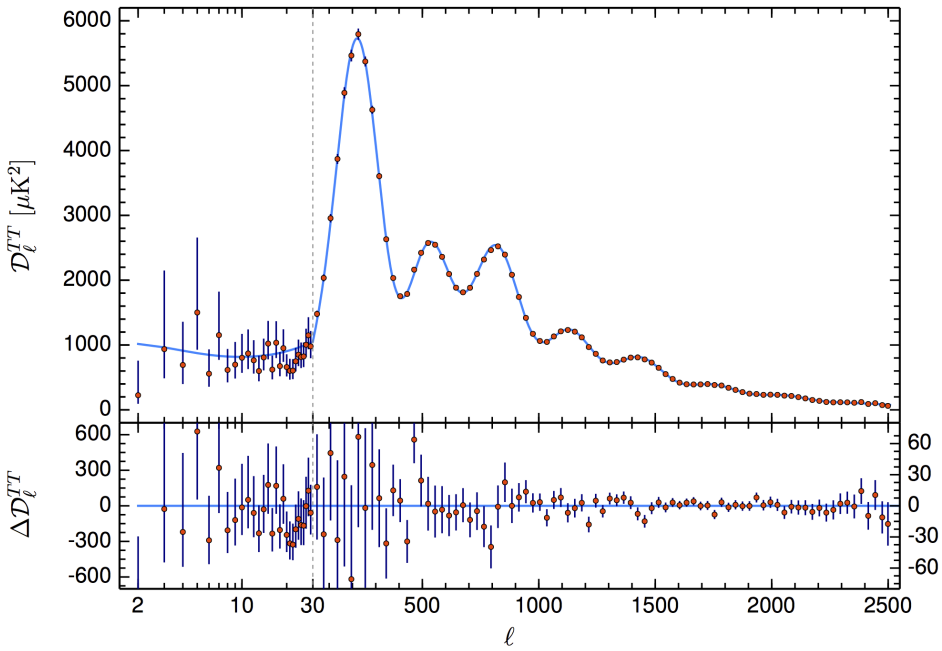

Figure 37: The temperature C_ℓ from Planck 2018 data. Unlike in Fig. 11, here the cosmic variance is included in the error bars, so the data can be more directly compared with theory. The blue curve is the ΛCDM prediction, and the bottom panel shows the difference (data residuals) between data and prediction. Note the different scale (on the right) for residuals at $\ell > 30$, where also the horizontal axis changes from logarithmic to linear. From [5].

There may be underestimated systematic errors in the distance-ladder measurements. 2) Note that the Planck value is not a "measurement" of H_0. It is a result of a six-parameter fit to the data, assuming the ΛCDM model, where H_0 is one of the six parameters. So the discrepancy could point to ΛCDM not being the correct model. One could alleviate the discrepancy by adding extra parameters to the model. (However, e.g., in the ΛCDM+Ω_k model the discrepancy becomes worse.) 3) The distance-ladder measurements are from a "local" part of the universe, $z < 1$, so it represents a local measurement of H_0; whereas the result from the CMB is related to the distance from here to the last scattering surface, so it corresponds to a value of H_0 which is representative of the entire observable Universe. The explanation of the discrepancy could thus be an unexpectedly large inhomogeneity: we live in a large underdense region, which thus expands faster than the Universe on average.

What should one make of such discrepancies? Similar issues are common in the progress of science. More often than not, they go away with improved data; but sometimes they point to something new, which improved data later confirms. For the large scale anomalies, "improved data" will be difficult to get, since here we are limited by cosmic variance. More accurate data on CMB polarization would help: are there similar large-scale anomalies in the polarization or not? The Planck data on polarization was inconclusive on this question [6], since the Planck design was not optimized for polarization measurements, and therefore there are residual systematic effects in the polarization data at large scales, which limits the accuracy.

References

[1] Planck Collaboration, *Planck 2013 results. I. Overview of products and scientific results*, arXiv:1303.5062, Astronomy & Astrophysics **571**, A1 (2014)

[2] Planck Collaboration, *Planck 2015 results. I. Overview of products and results*, arXiv:1502.01582, Astronomy & Astrophysics **594**, A1 (2016)

[3] Planck Collaboration, *Planck 2015 results. XIII. Cosmological parameters*, arXiv:1502.01589, Astronomy & Astrophysics **594**, A13 (2016)

[4] Planck Collaboration, *Planck 2018 results. I. Overview, and the cosmological legacy of Planck*, arXiv:1807.06205v1 (2018)

[5] Planck Collaboration, *Planck 2018 results. VI. Cosmological parameters*, arXiv:1807.06209v1 (2018)

[6] Planck Collaboration, *Planck 2018 results. VII. Isotropy and Statistics of the CMB*, arXiv:1906.02552v1 (2019)

[7] Planck Collaboration, *Planck 2018 results. X. Constraints on inflation*, arXiv:1807.06211v1 (2018)

[8] A.R. Liddle and D.H. Lyth: Cosmological Inflation and Large-Scale Structure (Cambridge University Press 2000)

[9] S. Dodelson: Modern Cosmology (Academic Press 2003)

[10] J. Väliviita, *PhD thesis*, University of Helsinki 2005

[11] A.G. Riess et al., *New Parallaxes of Galactic Cepheids from Spatially Scanning the Hubble Space Telescope: Implications for the Hubble Constant*, arXiv:1801.01120

[12] A.G. Riess et al., *Milky Way Cepheid Standards for Measuring Cosmic Distances and Application to Gaia DR2: Implications for the Hubble Constant*, arXiv:1804.10655

[13] W.J. Percival et al., *Measuring the Baryon Acoustic Oscillation scale using the Sloan Digital Sky Survey and Galaxy Redshift Survey*

[14] F. Beutler et al., *The 6dF Galaxy Survey: baryon acoustic oscillations and the local Hubble constant*, MNRAS **416**, 3017–3032 (2011)

[15] A.J. Ross et al., *The clustering of galaxies in the completed SDSS-III Baryon Oscillation Spectroscopic Survey: cosmological analysis of the DR12 galaxy sample.*, arXiv:1607.03155, MNRAS **470**, 2617 (2017)

[16] S. Alam et al., *The clustering of galaxies in the SDSS-III Baryon Oscillation Spectroscopic Survey: baryon acoustic oscillations in the Data Releases 10 and 11 Galaxy samples*, MNRAS **441**, 24–62 (2014)

[17] M. Betoule et al., *Improved cosmological constraints from a joint analysis of the SDSS-II and SNLS supernova samples*, Astronomy & Astrophysics **568**, A22 (2014)

[18] Keck Array and BICEP2 Collaborations, *Improved Constraints on Cosmology and Foregrounds from BICEP2 and Keck Array Cosmic Microwave Background Data with Inclusion of 95 GHz Band*, Phys. Rev. Lett. **116**, 031302 (2016)

[19] A.G. Riess et al., *Large Magellanic Cloud Cepheid Standards Provide a 1% Foundation for the Determination of the Hubble Constant and Stronger Evidence for Physics beyond* ΛCDM, Astrophys. J. **876**, 85 (2019)